

**SYNTHESIS AND CHARACTERISATION OF
CELLULOSE/NITROGEN DOPED TITANIUM DIOXIDE (N-TIO₂)
COMPOSITE USING HYDROTHERMAL METHOD FOR
SONOCATALYTIC DEGRADATION OF ORGANIC DYE**

LIM CHIN WOEI


**A project report submitted in partial fulfilment of the
requirements for the award of Bachelor of Engineering
(Honours) Chemical Engineering**

**Lee Kong Chian Faculty of Engineering and Science
Universiti Tunku Abdul Rahman**

April 2020

DECLARATION

I hereby declare that this project report is based on my original work except for citations and quotations which have been duly acknowledged. I also declare that it has not been previously and concurrently submitted for any other degree or award at UTAR or other institutions.

Signature : 

Name : LIM CHIN WOEI

ID No. : 1501328

Date : 26th April 2020

APPROVAL FOR SUBMISSION

I certify that this project report entitled **“SYNTHESIS AND CHARACTERISATION OF CELLULOSE/NITROGEN DOPED TITANIUM DIOXIDE (N-TIO₂) COMPOSITE USING HYDROTHERMAL METHOD FOR SONOCATALYTIC DEGRADATION OF ORGANIC DYE”** was prepared by **LIM CHIN WOEI** has met the required standard for submission in partial fulfilment of the requirements for the award of Bachelor of Engineering (Honours) Chemical Engineering at Universiti Tunku Abdul Rahman.

Approved by,

Signature

:



Supervisor

:

DR. PANG YEAN LING

Date

:

26th April 2020

The copyright of this report belongs to the author under the terms of the copyright Act 1987 as qualified by Intellectual Property Policy of Universiti Tunku Abdul Rahman. Due acknowledgement shall always be made of the use of any material contained in, or derived from, this report.

© 2020, Lim Chin Woei. All right reserved.

ACKNOWLEDGEMENTS

I would like to express my greatest gratitude towards my research supervisor, Dr. Pang Yean Ling for her unrelenting guidance and dedication provided to me during the course of this project. Additionally, I would also like to give my appreciation to my parents, younger brother and laboratory colleagues for providing all forms of assistance physically and psychologically necessary for the completion of my thesis and my degree. Lastly, special thanks to University Tunku Abdul Rahman for adequately and generously providing essential facilities, funding and expertise for me during the process of me completing this research project.

ABSTRACT

Cellulose /N-TiO₂ composite was successfully synthesized via the hydrothermal synthesis route and characterised using X-ray diffraction (XRD), scanning electron microscopy with energy dispersive X-ray (SEM-EDX) and Fourier Transform infrared spectroscopy (FTIR). Anatase N-TiO₂ was successfully deposited onto the extracted EFB cellulose fibre. An uneven layer of N-TiO₂ was formed on the surface of the cellulose fibres with occasional cracks. Additionally, N-TiO₂ aggregates and agglomerates were also present on the surface of the N-TiO₂ layered cellulose fibres. Comparatively, N-TiO₂/Cellulose composite showed an unprecedented improvement in terms of the sonocatalytic degradation of Congo Red in comparison with pristine TiO₂ and extracted EFB cellulose. In this work, parameter studies were also performed to determine the optimum amount cellulose on N-TiO₂, hydrothermal synthesis temperature, catalyst loading, oxidant type, oxidant dosage and solution pH. The highest sonocatalytic degradation efficiency and COD removal of Congo Red were 91.74 % and 73.7%, respectively after 30 min under optimum conditions. The prescribed conditions were 20 ppm Congo Red, 1.0 g/L of N-TiO₂/Cellulose with cellulose loading of 5 wt% that synthesized hydrothermally at 120 °C and the addition of 1.0 mM of potassium peroxymonosulfate under acidic condition.

TABLE OF CONTENTS

DECLARATION	i
APPROVAL FOR SUBMISSION	ii
ACKNOWLEDGEMENTS	iv
ABSTRACT	v
TABLE OF CONTENTS	vii
LIST OF TABLES	x
LIST OF FIGURES	xi
LIST OF SYMBOLS / ABBREVIATIONS	xv

CHAPTER

1	INTRODUCTION	
	1.1 General Introduction	1
	1.2 Importance of the Study	3
	1.3 Problem Statement	5
	1.4 Aims and Objectives	7
	1.5 Scope and Limitation of the Study	7
2	LITERATURE REVIEW	
	2.1 Biomass	8
	2.1.1 Cellulose	8
	2.1.2 Hemicellulose	11
	2.1.3 Lignin	12
	2.2 Titanium Dioxide	13
	2.2.1 Structure and Properties	15
	2.2.2 Synthesis Methods	19
	2.2.3 Titanium Dioxide Modifications	22
	2.3 Characterisation of Titanium Dioxide	24
	2.4 Organic Dyes	26
	2.4.1 Production of Organic Dyes	30

	2.4.2	Organic Dyes Removal Methods	32
2.5		Ultrasonic Irradiation and Sonoluminescence	34
	2.5.1	Sonolysis	35
	2.5.2	Sonocatalysis	37
3		METHODOLOGY AND WORK PLAN	
	3.1	Materials and Chemicals	38
	3.2	Overall Experimental Flowchart	39
	3.3	Preparation of Cellulose, Titanium Dioxide and Composite Materials	40
	3.3.1	Cellulose Extraction from Empty Fruit Bunch	40
	3.3.2	Preparation of Titanium Dioxide	41
	3.3.3	Preparation of Nitrogen Doped TiO ₂	41
	3.3.4	Hydrothermal Synthesis of Composite Material	41
	3.4	Experimental Setup for Sonocatalytic Degradation	42
	3.5	Liquid Sample Analysis	43
	3.6	Characterisation of Cellulose, Titanium Dioxide and Composite Materials	44
	3.6.1	X-Ray Diffraction (XRD)	44
	3.6.2	Scanning Electron Microscopy with Energy Dispersive X-ray (SEM-EDX)	45
	3.6.3	Fourier Transform Infrared Spectroscopy (FTIR)	45
4		RESULTS AND DISCUSSION	
	4.1	Characterisation of Sonocatalysts	46
	4.1.1	XRD	46
	4.1.2	SEM-EDX	51
	4.1.3	FTIR	58
	4.2	Parameter Studies	60
	4.2.1	Effect of Different Cellulose Loading	60
	4.2.2	Effect of Different Hydrothermal Synthesis Temperature	62

4.2.3	Effect of Different Catalyst Loading	64
4.2.4	Effect of Different Oxidant	65
4.2.5	Effect of Different Oxidant Dosage	67
4.2.6	Effect of Different Solution pH	68
4.3	COD Test Results	
5	CONCLUSIONS AND RECOMMENDATIONS	
5.1	Conclusions	71
5.2	Recommendations for Future Work	72
	REFERENCES	73

LIST OF TABLES

Table 1.1:	Fresh Oil Palm Fruit Constituent by Dry Weight Basis (Abdullah and Sulaiman, 2013).	5
Table 2.1:	Types of Synthetic Organic Dyes (Ziarani, et al., 2018)	28
Table 3.1:	Materials Involved in the EFB Cellulose Extraction Process and the Synthesis of TiO ₂ /Cellulose Composite Material.	38
Table 4.1:	Average Crystallite Size of TiO ₂ , N-TiO ₂ , and N-TiO ₂ Composites with Varying Cellulose Loading and Synthesis Temperature.	51
Table 4.2:	EDX Results for Various Catalysts.	57

LIST OF FIGURES

Figure 1.1:	World Water Consumption by Sector (Rijsberman and Cosgrove, 2000).	1
Figure 1.2:	World Water Consumption (Shahzad, et al., 2014).	2
Figure 1.3:	Water Pollution Caused by the Textile Industry within the G20 Community (Paraschiv, Tudor and Petrariu, 2015).	3
Figure 2.1:	Structure of Cellulose (Shrotri, Kobayashi and Fukuoka, 2017).	9
Figure 2.2:	Transformations of Cellulose Polymorphs (O’Sullivan, 1996).	10
Figure 2.3:	Xylan Hemicellulose (Shrotri, Kobayashi and Fukuoka, 2017).	12
Figure 2.4:	Hypothetical Structure of Lignin (Speight, 2008).	13
Figure 2.5:	TiO ₂ Photocatalysis Process (Nakata and Fujishima, 2012).	14
Figure 2.6:	TiO ₂ Superhydrophilicity (Fujishima, Rao and Tryk, 2000).	15
Figure 2.7:	Exotic Polymorphs of TiO ₂ which Consists of (a) Brookite, (b) B, (c) Baddeleyte, (d) Fluorite, (e) Spinel, (f) Hollandite, (g) Columbite, (h) OI, (i) Pyrite, (j) Ramsdellite and (k) Lepidocrocite-like (Angelis, et al., 2014).	16
Figure 2.8:	Anatase TiO ₂ Structure (Diebold, 2002).	17
Figure 2.9:	Rutile TiO ₂ Structure (Diebold, 2002).	18
Figure 2.10:	Brookite TiO ₂ Structure (Paola, Bellardita and Palmisanom 2013; Angelis, et al., 2014).	19
Figure 2.11:	XRD patterns of TiO ₂ Calcined at Various Temperatures (Viana, Soares and Mohallem, 2010).	24
Figure 2.12:	TGA and Differential Thermal Analysis (DTA) of TiO ₂ Synthesized via the Hydrolysis Route (Zoccal, Arouca and Goncalves, 2010).	25

Figure 2.13:	Langmuir Isotherm of TiO ₂ Calcined at 500 °C (Viana, Soares and Mohallem, 2010).	26
Figure 2.14:	Anaerobic Reductive Cleavage of Azo Dye (Ahlstrom, et al., 2005).	27
Figure 2.15:	Diazotization of Aromatic Amine (a) followed by the Azo Coupling Reaction (b) to form Azo Dye (Vaiano, Mari and Busardo, 2014).	31
Figure 2.16:	Overall Flow of Synthetic Dye Production (Rosa, et al., 2014).	31
Figure 2.17:	Sonolytic Degradation of Organic Compounds (Torres-Palma and Serna-Galvis, 2018).	36
Figure 2.18:	(a) Homogenous Acoustic Cavitation versus (b) Heterogeneous Acoustic Cavitation (Qiu, et al., 2018).	37
Figure 3.1:	Overall Experimental Flowchart.	39
Figure 3.2:	Experimental Setup for Sonocatalytic Degradation of Organic Dye.	42
Figure 4.1:	XRD Spectra of (a) TiO ₂ , (b) Cellulose, (c) N-TiO ₂ and N-TiO ₂ /Cellulose Composite with the Cellulose Portion of (d) 1 wt%, (e) 5 wt%, (f) 10 wt%, (g) 20 wt% and (h) 30 wt%.	47
Figure 4.2:	XRD Spectra of (a) TiO ₂ , (b) Cellulose, (c) N-TiO ₂ and N-TiO ₂ / 5 wt% Cellulose Composite at (d) 100 °C, (e) 120 °C, (f) 140 °C, (g) 160 °C and (h) 180 °C.	49
Figure 4.3:	SEM Images of Extracted EFB Cellulose at Magnifications of (a) 500×, (b) 1000×, (c) 5000× and (d) 5000×.	53
Figure 4.4:	SEM Images of (a) TiO ₂ and (b) N-TiO ₂ at 5000× Magnification.	53
Figure 4.5:	SEM Images of N-TiO ₂ /Cellulose Composites with Cellulose Loading of (a) 1 wt%, (b) 5 wt%, (c) 10 wt%, (d) 20 wt% and (e) 30 wt% at 5000× Magnification.	55
Figure 4.6:	SEM Images of N-TiO ₂ / 5 wt% Cellulose Composites Synthesized at (a) 100 °C, (b) 120 °C, (c) 140 °C, (d) 160 °C and (e) 180 °C at 5000× Magnification.	56

- Figure 4.7: FTIR Spectra of (a) TiO₂, (b) Cellulose, (c) N-TiO₂ and N-TiO₂/Cellulose Composite with the Cellulose Portion of (d) 1 wt%, (e) 5 wt%, (f) 10 wt%, (g) 20 wt% and (h) 30 wt%. 59
- Figure 4.8: FTIR Spectra of (a) TiO₂, (b) Cellulose, (c) N-TiO₂ and N-TiO₂/Cellulose Composite with 5 wt% Cellulose Synthesized at (d) 100 °C, (e) 120 °C, (f) 140 °C, (g) 160 °C and (h) 180 °C. 60
- Figure 4.9: Sonocatalytic Degradation of 20 ppm Congo Red with 0.5 g/L of (a) TiO₂, (b) cellulose, (c) N-TiO₂, and (d) N-TiO₂/Cellulose composite with Cellulose Loading of 5 wt%. 61
- Figure 4.10: Sonocatalytic Degradation of 20 ppm Congo Red with 0.5 g/L of N-TiO₂/Cellulose composite with Cellulose Loading of (a) 1 wt%, (b) 5 wt%, (c) 10 wt%, (d) 20 wt% and (e) 30 wt%. 62
- Figure 4.11: Sonocatalytic Degradation of 20 ppm Congo Red with 0.5 g/L of N-TiO₂/ 5 wt% Cellulose Composite Synthesized Hydrothermally at (a) 100 °C, (b) 120 °C, (c) 140 °C, (d) 160 °C and (e) 180 °C. 63
- Figure 4.12: Sonocatalytic Degradation of 20 ppm Congo Red with different catalyst loading of (a) 0 g/L, (b) 0.25 g/L, (c) 0.5 g/L, (d) 0.75 g/L, (e) 1 g/L and (f) 1.25 g/L of N-TiO₂/ 5 wt% Cellulose Composite Synthesized Hydrothermally at 120 °C. 65
- Figure 4.13: Sonocatalytic Degradation of 20 ppm Congo Red with N-TiO₂/Cellulose Composite Synthesized with Cellulose Loading of 5 wt% Synthesized Hydrothermally at 120 °C with the Addition of 1 mM (a) H₂O₂, (b) Potassium Persulfate and (c) Potassium Peroxymonosulfate 66
- Figure 4.14: Sonocatalytic Degradation of 20 ppm Congo Red with N-TiO₂/ 5 wt% Cellulose Composite Synthesized Hydrothermally at 120 °C with the addition of (a) 0 mM, (b) 0.2 mM, (c) 0.4 mM, (d) 0.6 mM, (e) 0.8 mM, (f) 1.0 mM, (g) 1.2 mM and (h) 1.4 mM Potassium Peroxymonosulfate. 68
- Figure 4.15: Sonocatalytic Degradation of 20 ppm Congo Red with N-TiO₂/ 5 wt% Cellulose Composite Synthesized Hydrothermally at 120 °C with 1.0 mM Potassium Peroxymonosulfate at Solution pH of (a) 2, (b) 4, (c) 6, (d) 8 and (e) 10. 69

Figure 4.16: COD Results for (a) Sonolysis, Sonocatalytic Degradation of Congo Red in the Presence of (b) N-TiO₂ and (c) N-TiO₂/ 5 wt% Cellulose Composite under Optimum Conditions.

LIST OF SYMBOLS / ABBREVIATIONS

C	final concentration of dye, mg/L
C_0	initial concentration of dye, mg/L
D	average crystallite size, nm
K	Scherrer constant
λ	X-ray wavelength, μm
β	peak width at half maximum, rad
θ	Bragg diffraction angle, degree
AOP	advance oxidation processes
COD	chemical oxygen demand
DTA	Differential Thermal Analysis
EFB	empty fruit bunches
FTIR	Fourier transform infrared spectroscopy
H_2O_2	hydrogen peroxide
KOH	potassium hydroxide
MBSL	multi-bubble sonoluminescence
NaOH	sodium hydroxide
N-TiO ₂	nitrogen doped titanium dioxide
SBSL	single-bubble sonoluminescence
SEM-EDX	scanning electron microscopy with energy dispersive x-ray
TGA	thermogravimetric analysis
TiO ₂	titanium dioxide
TPD-R-O	temperature programmed desorption, reduction and oxidation
UV	ultraviolet
UV-Vis	UV-visible spectrometry
XRD	x-ray diffraction
ZnO	zinc oxide

CHAPTER 1

INTRODUCTION

1.1 General Introduction

Water has been and will always be a significant necessity and commodity to not only the preservation and development of the human civilization, but also the preservation of the environment and the biosphere as a whole. Although 75 % of the surface of the earth is composed of water, roughly 95 % of these waters are saltwater and majority of the remaining reserves are stored in northern and southern ice caps, and glaciers which are distributed across the world (Odlare, 2014). As a result, only approximately 0.01 % of the earth's water exists in the form of readily usable fresh water. Such figures translate to the scarcity of accessible and usable freshwater especially in times of modern and rapid development accompanied the exponentiation of the human population. The world's water consumption can be differentiated into three major categories by consumption percentage as shown in Figure 1.1, which are the consumption by irrigation, industrial, and municipality (Rijsberman and Cosgrove, 2000). In total, roughly 3800 km³ of water were consumed by the stated human activities, where irrigation alone represented a staggering 70 % share of the total consumption. The industrial sector represented only about 20 % of the world's water consumption while the remainder is made out of municipal consumption.

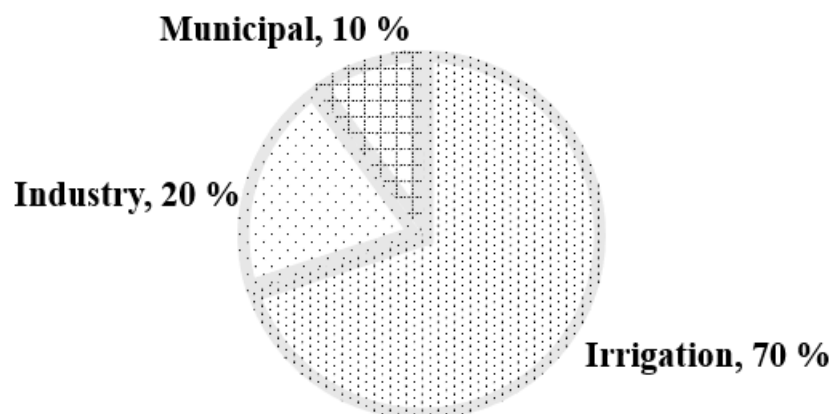


Figure 1.1: World Water Consumption by Sector (Rijsberman and Cosgrove, 2000).

Due to the reliance of human activities on freshwater supply, the consumption of water is often highly intangible from the boosting of the gross domestic product of any nation. Whereas in terms of gross domestic product, it is closely related to the balance between the growing population and national development. As the world strives for economic success, tremendous stress has been exerted on our water supplies due to the skyrocketing of water consumption as shown in Figure 1.2. Such phenomena is especially true in the developing Asia fuelled by the rapid growth in agriculture and other industries. Sequentially, the rise in water consumption is correlated to the rise in wastewater production which can lead to serious human and environmental problems. As reported by the International Water Association (2018), approximately 80 % of the world's wastewater production is currently discharged to the natural bodies of water without any prior treatment to minimize the dangerous anthropogenic constituents that are contained by these effluents. Statistically, the industrial wastewater production of 2212 km³/year was identified along with 330 km³/year of municipal wastewater being produced simultaneously (Food and Agricultural Organization of the United Nations, n.d.; Mateo-Sagasta, Raschid-Sally and Thebo, 2015). As a result, an irreversible climactic disaster and the deterioration of the ecosystem will be upon us if the current wastewater discharge rates are persisted without change.

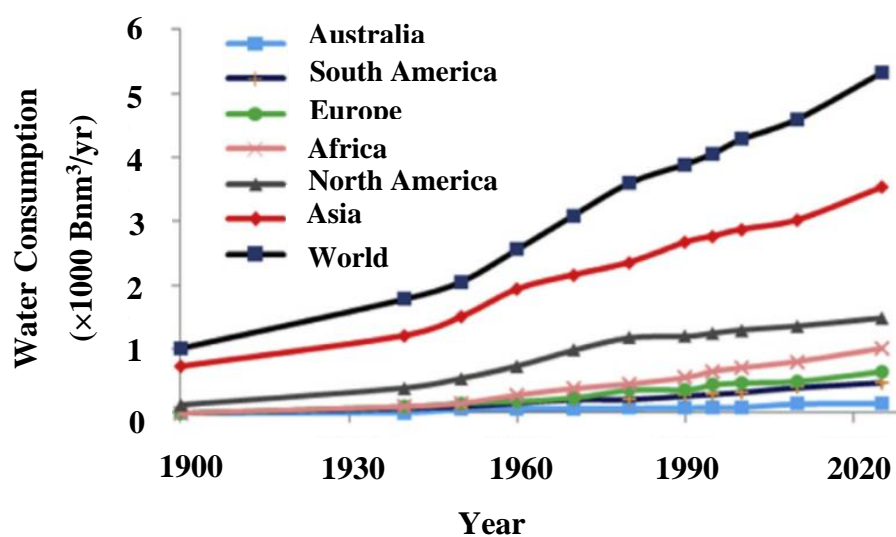


Figure 1.2: World Water Consumption (Shahzad, et al., 2014).

The textile industry is one of the producers of wastewater with high human and environmental toxicity due to the presence of dye constituents. Especially when textiles are produced by the wet process pathway, the involved dyeing process consumes a significant amount of water as compared to its dry counterpart and releases effluents with horrendous colours (Yaseen and Scholz, 2019). Mostafa (2015) found out that the average untreated textile industry effluent had a maximum chemical oxygen demand of 12 000 mg/L accompanied by oil, grease, traces of heavy metal, sulphates, and a maximum colour rating on the platinum-cobalt scale of 2500. Paraschiv, Tudor and Petrariu (2015) further reported that even the G20 community which is composed of the world's largest and leading economies has textile wastewater contamination problems as shown in Figure 1.3. In China alone, it was reported that 20.29 % of China's water pollution was attributed to the textile industry. Turkey's water contamination problem was reported to be even worse at 32.21 %. On the bright side, the United States have a relatively low percentage of contamination at only 4.29 %, with the lowest being in Germany with the figure of 2.44 %. As a result, no matter the contamination level, a feasible and economical solution has to be devised swiftly to deal with the contaminations caused by the textile industry.

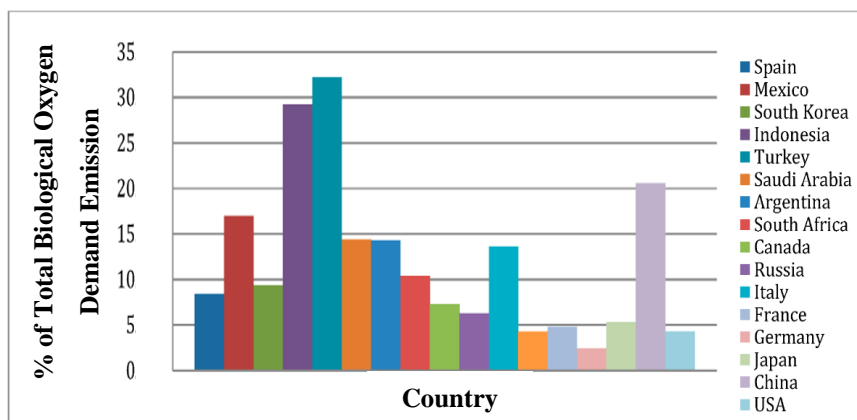


Figure 1.3: Water Pollution Caused by the Textile Industry within the G20 Community (Paraschiv, Tudor and Petrariu, 2015).

1.2 Importance of the Study

Malaysia is one of the leading producers and exporters of palm oil in the world since the beginning of the rapid expansion of the oil palm plantation in 1960

with the plantation yield of about 100 000 tonnes in 2016. As a result, 17.32 million tonnes of crop yield have been produced which translates to RM 64.42 billion per annum of earning and was responsible for 5 % to 7 % of the Malaysian gross development product (Choo, 2012; Nambiappan, et al., 2018). Oil palm biomass wastes consisting of empty fruit bunches (EFB), mesocarp fruit fibres, and palm kernel shells are produced in a significant amount as a result of the oil extraction process where each palm tree gives a biomass waste to oil is around nine to one (Abdullah and Sulaiman, 2013). Owing to the rapid expansion of the oil palm industry which can be directly correlated to the blooming waste problem as a consequent of the industry itself, a proficient waste integration and valorisation initiative has to be outlined, executed, and regulated to ensure the attainment of sustainable mutual economical benefits while safeguarding the environment in coherence to the participation of Malaysia in the sustainable development goals of the United Nations. As a result, the transformation of oil palm biomass wastes into value-added products via the valorisation these wastes can provide a sustainable, steady, abundant and feasible catalyst source to various waste treatment industries.

Secondly, the development of advance oxidation processes (AOP) is extremely crucial to replace the relatively ineffective conventional treatment methods due to the chemical nature of AOP which degrades organic pollutants into carbon dioxide and water (Bethi, et al., 2016). The degradation mechanisms of AOP technologies involve intermediates that are superior in the reactivity perspective, and those waste molecules that are extremely persistent that strongly resist archetypal degradation methods can be vanquished with ease. These aspects reinforce the notion of AOP having the upper-hand in managing wastes. The current wastewater treatments were designed to cope with conventional existing wastes that were identified retrospectively, and can find it challenging when degrading modern chemicals ranging from pharmaceutical products to personal use products, or even newly developed complex organic molecules (Ghauch, 2017). As a result, AOP promises a better prospect in the evolution of the waste treatment industry.

1.3 Problem Statement

Oil palm wastes valorisation has been the centre of attention in recent years especially in the context of Malaysia. Malaysia has been and still is a major player in the oil palm industry where it is reported that in year 2008, Malaysia have utilized 4.5 million hectares of land to produce a staggering 17.7 million tonnes of palm oil which is the second largest producer in that time (Abdullah and Sulaiman, 2013). Based on the Malaysian Palm Oil Board (2019), the crude palm oil output has been raised to about 19.6 million tonnes per year. Since 2008, Malaysia has been holding firmly to the world's second largest palm oil producer just below Indonesia with a percentage of 28 % (Ling, 2019). Although the palm oil trade offers a lucrative return to the Malaysian economy, the valued crude palm oil was found to be only 21 % by dry weight basis of a fresh oil palm fruit which translates to 79 % of biomass wastes as shown in Table 1.1 (Abdullah and Sulaiman, 2013). Based on the statistics mentioned, a significant and undeniable amount of biomass wastes are produced during the palm oil extraction process. Additionally, 75 % of the solid residues resulted from an oil palm mill is typically left to decompose in plantation grounds for nutrient recycling purposes, while the remaining 25 % are used for internal electricity generation of the mill itself (Awalludin, et al., 2015). Specifically, EFB is often burned as a source of fuel for the operation of a palm oil refinery, the produced fruit bunch after oil extraction has a great deal of moisture which lowers the efficiency of boilers. As a result, oil palm based lignocellulosic biomass is especially lucrative as Malaysia pushes towards complete waste valorisation.

Table 1.1: Fresh Oil Palm Fruit Constituent by Dry Weight Basis (Abdullah and Sulaiman, 2013).

Fresh Oil Palm Fruit Constituent	Percentage by Dry Weight Basis (%)
Palm oil	21
Palm kernel	7
Fibre	15
Shell	6
Empty fruit bunches	23
Palm oil mill effluent	28

In conjunction with the synthesis of titanium dioxide (TiO₂) hybrid materials, the existing conventional techniques utilized during the synthesis process includes simpler methods like sol-gel impregnation and hydrothermal synthesis, and sophisticated methods like magnetron sputtering, plasma treatments, polymerization of suspension and cross-linking approaches (Dong, et al., 2018). In terms of sol-gel impregnation, the overall process takes a significant amount of time which can be a problem considering the operative costs during the synthesis process (Dong, et al., 2018). Complex methods like magnetron sputtering and plasma treatments are generally plasma based method involving the generation of noble gas ion plasma alongside with fed-oxygen and the subsequent bombardment of these gaseous ions onto a pure titanium target in a chamber to induce TiO₂ deposition onto the pre-treated cellulosic material (Geng, 2018; Nunez, et al., 2017). Despite that plasma-based techniques have the upper-hand of intricate morphology manipulation, they often involve extravagant equipment to perform (Dong, et al., 2018). In contrary, the polymerization technique can enhance TiO₂ attachment to cellulosic materials without the use of plasma in exchange of a high solvent requirement and a complex synthesis procedure due to the use of droplet polymerization for the coating of TiO₂ onto cellulosic materials (Dong, et al., 2018; Jiang, et al., 2011). The cross-linking technique also requires highly expensive solvents in exchange for a better thermal and mechanical stability of the catalyst (Yousefi, et al., 2019; Dong, et al., 2018). As a result, the method of hydrothermal synthesis will be explored in this work.

Ultimately, the photocatalytic pollutant degradation efficiency of organic pollutants in the presence of TiO₂ is hugely dependant on its ability to produce adequate amounts of radicals by the generation of photogenerated electron-hole pairs via its photocatalytic capabilities. Consequently, the two major parameters that pose significant challenge in ensuring an excellent catalytic efficiency are the reduction of the electronic band gap energy, and the prevention of the recombination of photoelectrons and holes either on the surface of the catalyst, or within the volume of the catalyst itself (Bora and Mewada, 2017). These two problems are prominent in pristine TiO₂ due to the fact that TiO₂ has a large band gap around 3.2 eV. This limits its initiation source to only UV radiation which only represents about less than 5 % of the solar

radiation after passing through the atmosphere to reach the surface of Earth (Lin, et al., 2010). At the same time, UV radiation does not penetrate well into bodies of water contaminated by deeply gloomy dyes hence limiting its usability in a large scale industrial process. As a result, the chemical alteration towards the band gap energy of TiO_2 and the improvement of the efficiency of the initiation source reaching TiO_2 itself are to be considered by employing pre-treated lignocellulosic carbonaceous materials and the concept of sonocatalysis.

1.4 Aims and Objectives

This project will encompass three major objectives:-

1. To extract cellulose from oil palm biomass.
2. To synthesize N- TiO_2 /Cellulose hybrid composite material via the hydrothermal route and characterize its properties using various techniques.
3. To determine the optimum conditions for sonocatalytic degradation of synthetic organic dye in the presence of N- TiO_2 /Cellulose composite.

1.5 Scope and Limitation of the Study

The research is limited to the utilisation of TiO_2 as the sole metal oxide photocatalyst throughout the experiment, followed by the use of cellulose extracted only from the EFB of an oil palm fruit. Additionally, the composite will only be synthesized via hydrothermal means with varying hydrothermal temperatures, reaction time, and hydrothermal solution concentration. The characterisation study of the crystallinity, surface morphologies, functional groups, thermostability and acidity of the composite catalyst are conducted by X-ray diffraction (XRD), scanning electron microscopy with energy dispersive X-ray analyses (SEM-EDX) and Fourier transform infrared spectroscopy (FTIR), respectively. In addition to catalyst characterization, the sonocatalytic activities of the synthesized catalyst will be studied based only on its efficiency in degrading organic dye.

CHAPTER 2

LITERATURE REVIEW

2.1 Biomass

Biomass represents a family of organic materials itself where these materials are primarily derived from a plant based source. Some of the examples of the most common biomass can range from simple monomers like glucose, to macromolecules like oils and complex polymeric structures like cellulose. Additionally, a portion of the current industrial and domestic wastes are also rich in organic constituents due to the way of production and consumption of substances derived from nature, can be considered as biomass too. Food wastes and agricultural wastes are two of the industrially and domestically produced biomass waste. Ultimately, lignocellulosic materials like wood, generic organic wastes like food wastes, and algae are the three main feedstocks for the global biomass consumption.

Lignocellulosic biomass has long been the central of attention in the frontier of biomass due to its abundance resulted from the mass selective extraction of certain components from plants such as sugar extraction from sugar cane (Vanek, Albright and Angenet, 2012). Mass production of sugar cane sugar has led to the accumulation of the residual stalks of the sugar cane itself, which represents a majority of the carbon by weight of the crop. As a result, the produced biomass wastes such as sugar cane which consist of the majority amount of energy produced by a crop are now utilized in various fields, particularly in the production of biodiesel (Ma and Hanna, 1999), waste treatment catalyst enhancement (Mohamed, et al., 2017), energy (Deboni, et al., 2016), and chemicals like methanol (Trop, Anicic and Goricanec, 2014).

2.1.1 Cellulose

Cellulose is one of the major constituent in lignocellulosic biomass other than hemicellulose and lignin. It is generally derived from plants especially in cell walls, and also found in various bacteria, algae, and some other major classes of microorganisms like the prokaryote. As shown in Figure 2.1, cellulose is made from the polymerization of six carbon sugar monomers (glucose), where

each monomer is linked its adjacent monomers with the β -1,4-glycosidic bond forming a long glucan homogenous polymeric chain. More specifically, the form of glucose units in cellulose are known as d-glucopyranose where the first and fifth carbon of the molecule are linked by an oxygen atom, and each subsequent monomer is 180° flipped from its neighbouring monomers (Shrotri, Kobayashi and Fukuoka, 2017). It can further be classified into 7 crystalline forms of cellulose. The most common two forms of cellulose are cellulose I (native cellulose), and cellulose II (a rare derivative form of cellulose I) (Brown, 2003).

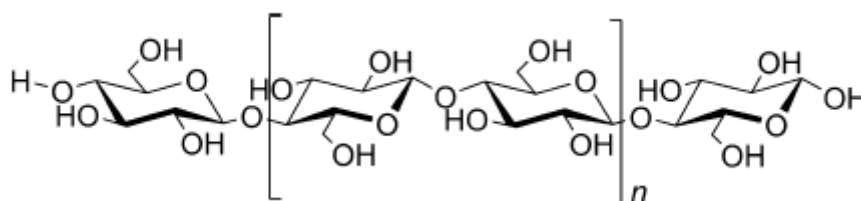


Figure 2.1: Structure of Cellulose (Shrotri, Kobayashi and Fukuoka, 2017).

Cellulose I, has a crystal structure where its glycosidic bonds are arranged in a parallel manner and can be further classified into two sub-crystalline forms depending on the hydrogen bonding patterns of its monomers. The two sub-crystalline forms are known as cellulose 1α and cellulose 1β where the metastable triclinic cellulose 1α is rarely found in organisms. Meanwhile the monoclinic cellulose 1β is more thermodynamically stable and is found in abundance in plant based cellulose (O'Sullivan, 1996). In plant-based organisms, their genetic materials will provide metabolic instructions for the arrangement of cellulose I into different forms of nanostructures which are known as microfibrils, and are used to control and manipulate structural growth of the plant itself (Brown, 2003). Furthermore, the content of cellulose I in plant-based organisms plays a significant role in determining not only the structural stability of the plant itself, but the thermal properties of its fibres. Poletto, Junior and Zattera (2014) discovered that fibres containing cellulose I with high crystallinity could lead to the enhancement in both tensile strength and resistance to thermal degradation, but has minimal influence in regulating the accumulation of moisture in fibres. This was due to the increment in

hydrogen bonding between the phenolic groups of lignin and cellulose I which enhanced the mechanical strength of the fibres, and also promoted the close packing of cellulose I which deteriorated heat transfer and increased thermal stability of the overall structure.

Cellulose II is rarely obtained from organisms except for a small number of algae and bacteria although it is thermodynamically more stable as compared to cellulose I due to the presence of an additional hydrogen bond per glucose residue (Brown, 2003; Kolpak and Blackwell, 1975). Comparatively, instead of having parallel glycosidic bonds, cellulose II has anti-parallel glycosidic bonds, and is artificially synthesized via the irreversible regeneration and mercerization of cellulose I (O'Sullivan, 1996). The process of mercerization involved the alteration of cellulose I chain polarities and its hydroxymethyl groups leading to chain swelling and twisting which results in better reactivity, tensile strength, and thermal stability of cellulose (Yue, 2011). As a result, the synthesis of cellulose II from cellulose I allows a wider usage of biomass cellulose in the chemical industry and also the infrastructural industry.

The remaining types of cellulose are physiochemically derived from cellulose I and II, which are cellulose III and cellulose IV as shown in Figure 2.2. Both cellulose III and cellulose IV can be further classified into type I (cellulose III_I and cellulose IV_I) and type II (cellulose III_{II} and cellulose IV_{II}) depending on the original cellulose where they are derived from. In general, cellulose III_I is derived from the ammonia treatment of cellulose I which is reversible, and can be subsequently irreversibly transformed into cellulose IV_I via heat and glycerol.

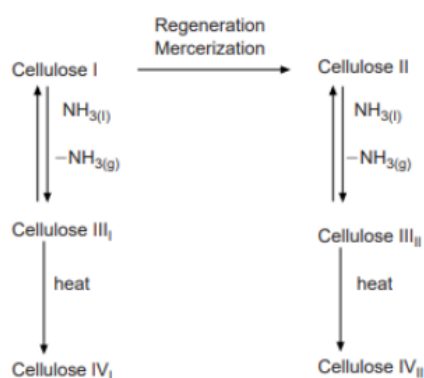


Figure 2.2: Transformations of Cellulose Polymorphs (O'Sullivan, 1996).

Cellulose III_{II} and cellulose IV_{II} are also obtained using a similar fashion. Cellulose III has a hexagonal unit crystal cell and its primary usage is to improve cellulose I by reversibly retransforming cellulose III back to cellulose I which has properties that slightly differ from the pristine cellulose I (O'Sullivan, 1996). As a result, the re-obtained cellulose I inherits unique crystalline properties such as crystallographic distortion and fragmentation caused by the process of cellulose III transformation, hence having better surface area and activity. For cellulose IV, it is typically obtained from the heated glycerol treatment of cellulose III hence crystallographically transforming it from a hexagonal unit cell into an orthogonal unit cell (O'Sullivan, 1996). However, its usages are not common where one of the rare examples is shown by Okiyama, Motoki and Yamanaka (1993). They utilized bacterial derived cellulose IV as structural reinforcements and bulking agents for food due to its excellent thermal stability, smooth texture, and high water retention capacity.

2.1.2 Hemicellulose

Unlike cellulose, hemicellulose is not considered as a homopolymer as it is composed of different monomers mainly consisting of 5 carbon sugars (pentose) with a small number of 6 carbon sugars (hexose) and saccharide derived acids. Nonetheless, hemicellulose is bonded to cellulose via hydrogen bonding and is also covalently bonded to lignin within a lignocellulosic structure. It is amorphous in nature as compared to cellulose. Xylose is said to be the most abundant pentose within the hemicellulose polymeric structure, followed by other pentose like arabinose, and subsequently hexose which consists of glucose, mannose and galactose (Nag, 2008). Trace amounts of other hexose like rhamnose can also be found along with other trace constituents of hemicellulose like glucuronic acid, methylglucuronic acid, and galacturonic acid. Owing to its chemical diversity found within its structure as compared to its homogenous counterpart and its biodegradability, the utilisation have been extensively researched by researchers in terms of paint stabilisation (Mikkonen, et al., 2019), coatings and adhesives that are associated with paper (Farhat, et al., 2017), and even the synthesis of bioethanol (Smugu-Kogut, et al., 2019).

Depending on the constituent of the hemicellulose itself, it can be generally classified into xylan as shown in Figure 2.3, which is the most

abundant hemicellulose in plants, xyloglucan, mannan, glucomannan, and mixed-linkage glucan (Scheller and Ulvskov, 2010). Specifically, xylan is a hemicellulose that is comprised of a heterogeneous backbone of 1,4-linked β -D-xylopyranose with arabinose residues attached on it that plays an important role in forming the hard and woody part of plants (Nag, 2008). In contrary to xylan, xyloglucan can be easily found in the soft and woody parts of a plant. Other plant-based hemicelluloses are xynoglucan which can be found in almost all plant species, while rarer forms of hemicellulose like mannan, glycomannan and mixed-linkage glucans are only dominant in a limited number of plant and algae species.

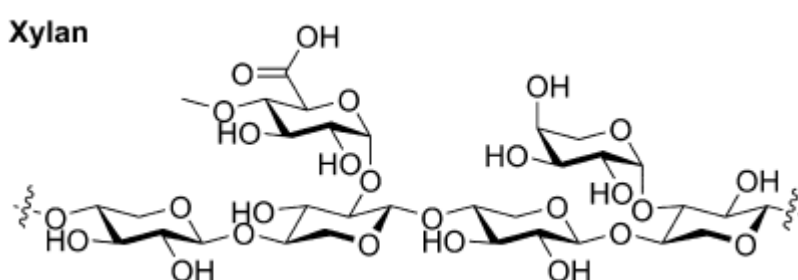


Figure 2.3: Xylan Hemicellulose (Shrotri, Kobayashi and Fukuoka, 2017).

2.1.3 Lignin

Lignin is the final major constituent of a lignocellulosic material, and has the highest degree of molecular complexity as compared to both cellulose and hemicellulose. The structure of lignin is shown in Figure 2.4. Additionally, unlike its counterparts, lignin is not a result of the polymerization of carbohydrates, but an extensively complex molecule that comprises of aromatic groups linked to aliphatic chains although its exact structure is not explicitly known. Fundamentally, p-hydroxyphenylpropane is one of the most significant monomer in the making of lignin and the overall structure of lignin is derived from three alcohols, which are p-coumaryl alcohol, sinapyl alcohol and coniferyl alcohol (Speight, 2008).

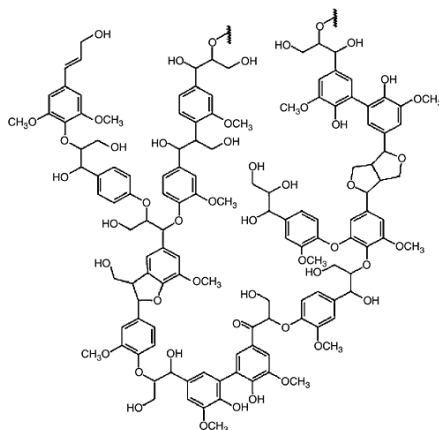


Figure 2.4: Hypothetical Structure of Lignin (Speight, 2008).

Due to the molecular nature of lignin, it is not readily biodegradable and resistance to hydrolysis which makes its transformation difficult. As a result, woody crops and wastes that contain a high weight fraction of lignin are hardly utilized in cellulose and hemicellulose consuming industries due to the inability of effective degradation of lignin. Nonetheless, researchers have been developing methods to separate lignin from the usable contents proficiently via steaming or aqueous bisulfite solution dissolution (Speight, 2008). Furthermore, lignin itself is useful after undergoing hydrolysis or pyrolysis processes that can degrade its massive cross-linking internal structures (Chio, Sain and Qin, 2019). Some examples of these operations are the catalytic pyrolysis of lignin to aromatic hydrocarbons (Ryu, et al., 2019), thermal radiolysis of lignin to phenolic compounds (Ponomarev, 2017), and biodegradation of lignin by fungi, bacteria and laccases (Asina, et al., 2016).

2.2 Titanium Dioxide

TiO₂ has gained popularity in recent times due to its many interesting properties, especially in the field of degradation of organic pollutants under solar radiation which was built upon the works of Fujishima and Honda (1972) on photolysis. The applications of TiO₂ usually involve several forms of electromagnetic radiation, like the development of photocatalyst to degrade dyes (Miao, Zhang and Zhang, 2018), photo fuel cell (He, et al., 2018), and photo-assisted chemical detections (Si, et al., 2019) due to its ability to generate conducting electrons using photons. However, its usage stretches far beyond the mentioned ranging

from electronics as gate dielectrics (Najafi-Ashtiani, 2018), thermal insulation (Bao, Kang and Ma, 2018), tumour markers and treatments (Zhang, et al., 2019; Jia, et al., 2019).

TiO₂ is one of the major photocatalytic material that has been widely researched due to several interesting properties when incident by electromagnetic radiation in the ultraviolet (UV) to the visible light spectrum. The electrons within the valence band of TiO₂ particles are able to be excited to the conduction band upon absorbing an incoming photon. As a consequent, a positive hole is left behind by each escaped electron, hence forming a photo-generated electron-hole pair within the material. These extremely reactive electron-hole pairs are able to diffuse to the surfaces of TiO₂ to perform oxidation and reduction reactions with other organic compounds that are being adsorbed. Specifically, the electrons generated can react with surrounding oxygen molecules to form superoxide radicals ($\bullet\text{O}_2^-$) which are highly oxidative (Fujishima, Zhang and Tryk, 2008) as shown in Figure 2.5. Additionally, hydroxyl ions on the surfaces of TiO₂ can be violently oxidize to form hydroxyl radicals (Nakata and Fujishima, 2012). These radicals and electron-hole pairs are able to mineralize adsorbed organic compounds into carbon dioxide and water molecules. As a result, TiO₂ has been conventionally employed in advance oxidation process (AOP) waste degradation due to its financial friendliness, stellar redox capabilities, and unparalleled resistance to both chemical and photocorrosion (Ram, Andreescu and Ding, 2011).

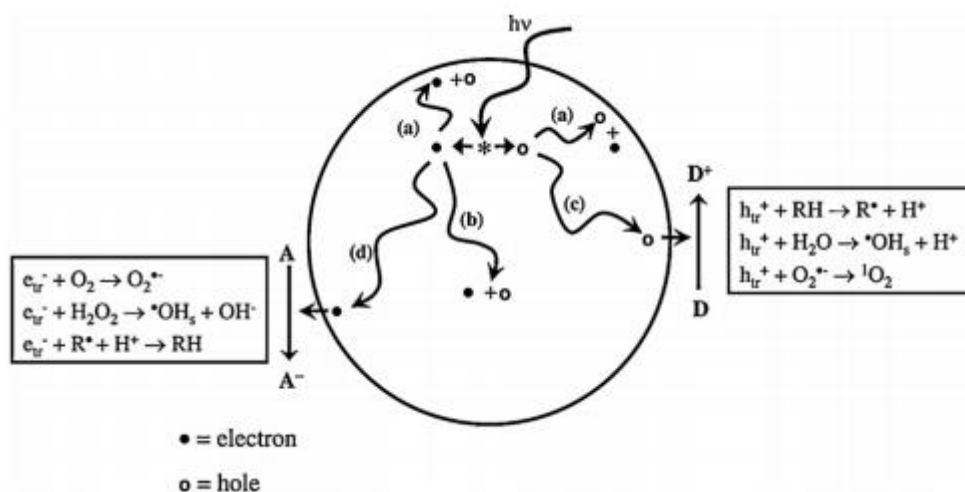


Figure 2.5: TiO₂ Photocatalysis Process (Nakata and Fujishima, 2012).

Another interesting photo-induced property surrounding TiO_2 is its ability to undergo hydrophobic to hydrophilic surface transition which is known as superhydrophilicity. Prior to any surface modification, TiO_2 surfaces itself is hydrophobic by nature. However, trapped hydroxyl radicals within the crystal of TiO_2 accompanied by oxygen vacancies that are generated by photocatalytic reactions may cause conformational chemical changes of TiO_2 surfaces as shown in Figure 2.6 (Fujishima, Rao and Tryk, 2000; Nakata and Fujishima, 2012). When these sites are in contacted with water, the formation of thermodynamically less stable hydroxyl groups will induce hydrophilicity on TiO_2 surfaces.

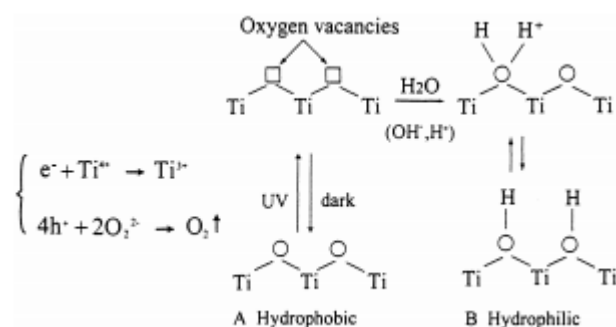


Figure 2.6: TiO_2 Superhydrophilicity (Fujishima, Rao and Tryk, 2000).

The general application of superhydrophilicity of TiO_2 is to prevent fogging on material surfaces as instead of water droplet dispersion. Superhydrophilic surfaces are able to ensure thin and uniform liquid film formation which is beneficial for evaporative operations. Zhou, et al. (2019) were able to utilize this property of TiO_2 to create switchable superhydrophobic-superhydrophilic TiO_2 films for surface moisture and fouling control. Other applications for superhydrophilicity of TiO_2 are oil-water emulsion separation (Jiang, et al., 2018) and pervaporation dehydration (Gong, et al., 2013).

2.2.1 Structure and Properties

In general, TiO_2 is a metal oxide semiconductor which can exist in three different crystal phases. This include the tetragonal rutile, anatase, and rhombohedral brookite phases. Comparatively, the rutile and anatase phase TiO_2 are being conventionally utilized for most of the TiO_2 applications due to

their reactive surfaces and better electronic properties as compared to their counterparts (Diebold, 2002). Additionally, TiO_2 has a variety of exotic and semi-stable polymorphs that are shown in Figure 2.7 which consists of high pressure derivatives of rutile and anatase, and polymorphs that are able to form 2 dimensional TiO_2 sheets (Angelis, et al., 2014).

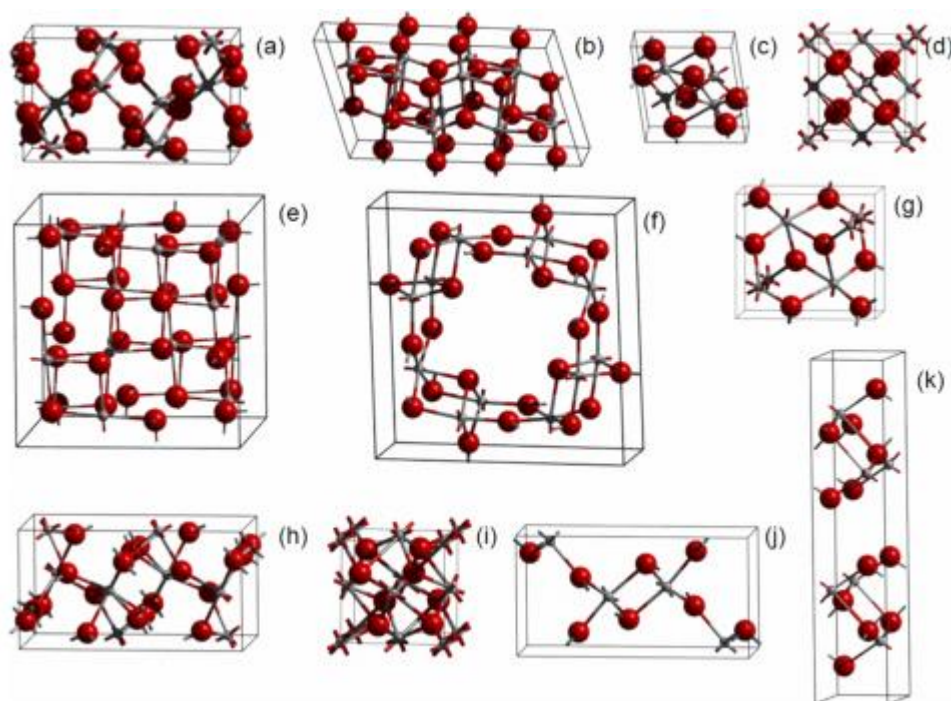


Figure 2.7: Exotic Polymorphs of TiO_2 which Consists of (a) Brookite, (b) B, (c) Baddeleyite, (d) Fluorite, (e) Spinel, (f) Hollandite, (g) Columbite, (h) OI, (i) Pyrite, (j) Ramsdellite and (k) Lepidocrocite-like (Angelis, et al., 2014).

Ultimately, the crystal structure of TiO_2 regulates three significant factors that are the position of valence and conduction bands, band gap energy, and also the surface energy of TiO_2 polymorphs. The generation of photoelectrons and holes are only possible if the conduction band lies within close proximity of the valence band, and small band gap energy. However, the generated photoelectrons and holes may not be useful if the surfaces of TiO_2 has low surface energy, which translates to low surface reactivity due to the increase of the difficulty of surface contaminant adsorption (Yang, et al., 2008). Comparatively, the anatase phase of TiO_2 has the most excellent structural, surface, and electronics property that is suitable for photocatalysis reactions as

compared to rutile and the other polymorphs (Conesa, 2010; Kavan, et al., 1996).

Figure 2.8 shows the anatase polymorph of TiO_2 . It has a tetragonal individual cell unit where the overall crystal structure is made out of slightly altered octahedral building blocks that are sharing four edges with each other, and has 5 different facets according to the Wulff construction (Diebold, 2002).

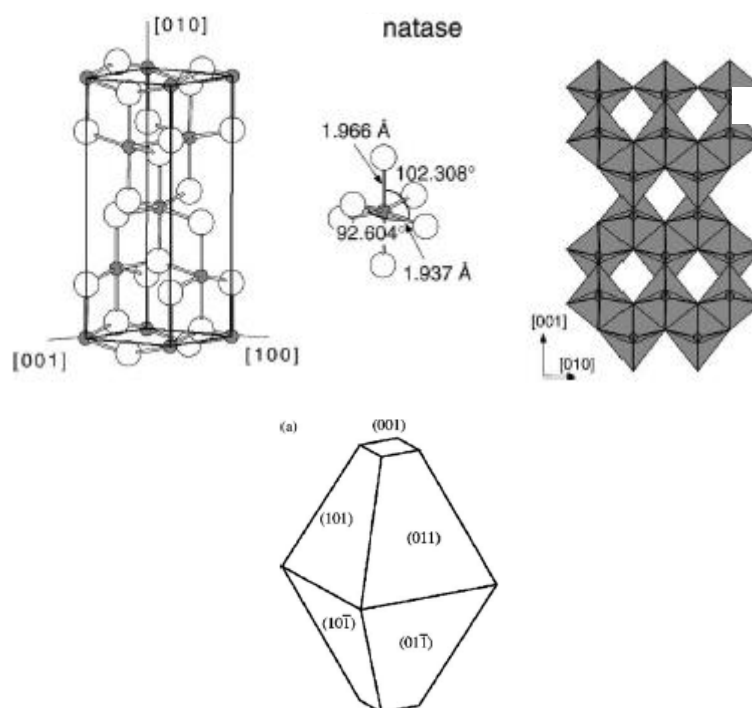


Figure 2.8: Anatase TiO_2 Structure (Diebold, 2002).

Anatase TiO_2 has a band gap of around 3.2 eV with facet (001) has the highest surface energy but is thermodynamically less stable as compared to the abundant facet (101) which also has the lowest surface energy (Yang, et al., 2008). As a result, anatase TiO_2 with a majority of facet (001) is always preferable in photocatalytic degradation. The difference in surface energies of different facets in anatase TiO_2 is primarily due to the conduction band edge. The higher the energy of the conduction band edge accompanied by the presence of a large number of less coordinated titanium atoms and huge Ti-O-Ti bond angles will typically give a higher surface energy (Mirkut, Kobielski and Macyk, 2019). Additionally, anatase TiO_2 is able to produce photoelectrons and holes that have greater oxidative and reductive abilities as compared to

rutile TiO_2 due to its larger band gap energy. Other superior properties of anatase TiO_2 over rutile TiO_2 involve lower conduction band, smaller indirect band gap which promotes surface reaction participation probability, and better charge transport (Luttrell, et al., 2014).

Rutile TiO_2 is also tetragonal by nature, and is formed by octahedral TiO_6 crystal cell units with each octahedron sharing two edges with its adjacent octahedrons as shown in Figure 2.9 (Hanaor and Sorrell, 2011). Facet (111) of rutile TiO_2 was reported to have the greatest photocatalytic efficiency, and can be further improved in terms of water splitting and charge separation by the synergistic effects when working simultaneously with other facets (Lai, et al., 2013).

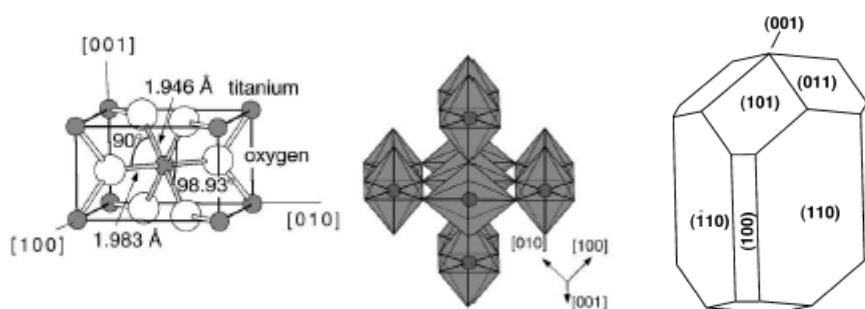


Figure 2.9: Rutile TiO_2 Structure (Diebold, 2002).

As reported by Kakuma, Nosaka and Nosaka (2015), although rutile TiO_2 was able to produce more hydrogen peroxide and superoxide radical as compared to anatase TiO_2 , the generation of these reactive species were ineffective in enhancing its photocatalytic activity. This is due to the short Ti-Ti distance on the surface of rutile TiO_2 which can lead to the formation of Ti-O-O-Ti groups by consuming two holes that were supposedly used for photocatalytic operations. However, the combination of both rutile and anatase TiO_2 was observed to be beneficial due to the transfer of photoelectrons from rutile TiO_2 to anatase TiO_2 which can improve charge separation (Wang, et al., 2016).

On the other hand, brookite TiO_2 has a similar octahedral construction in terms of its crystallography, where each octahedron shares three edges with its adjacent octahedrons as shown in Figure 2.10 (Paola, Bellardita and

Palmisanom 2013). Interestingly, the most reactive surface of brookite TiO_2 which is the facet (210) shares a staggering amount of similarity with the facet (101) of anatase TiO_2 with an exception that facet (210) of brookite TiO_2 is far more reactive (Angelis, et al., 2014).

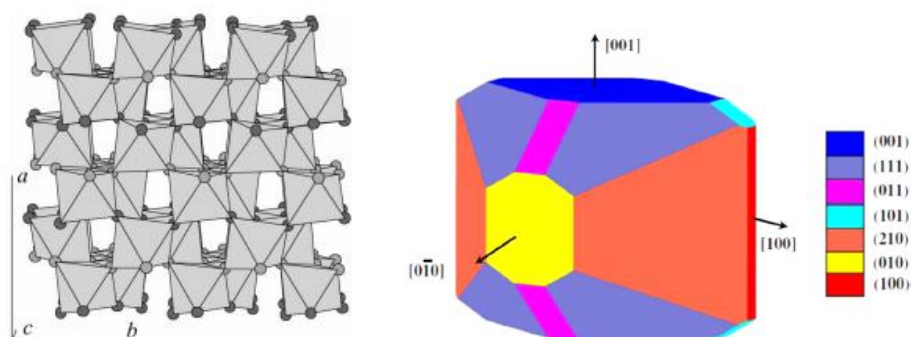


Figure 2.10: Brookite TiO_2 Structure (Paola, Bellardita and Palmisanom 2013; Angelis, et al., 2014).

However, the charge transfer from the surface of facet (210) to the adsorbed species was negligible, which makes it an unlikely candidate for photocatalysis reaction (Rodriguez, et al., 2012). Despite that, brookite TiO_2 has also been widely researched for the development of better photocatalyst, but its development has been continuously impeded its instability and the inability of synthesizing high purity brookite phase TiO_2 as compared to rutile and anatase TiO_2 (Park, et al., 2018).

2.2.2 Synthesis Methods

In recent times, the synthesis of TiO_2 nanostructures have gained much attention due to the presence of quantum confinement effects when TiO_2 particles has a radius of smaller than 10 nm (Gupta and Tripathi, 2011). Owing to these effects, the band gap of TiO_2 nanoparticles were found to increase and effectively enhanced the redox potential of its photo-generated electron and holes without affecting charge transfer. As a result, liquid phase synthesis methods like the hydrothermal synthesis route have been gradually developed by researchers to manipulate these nanostructures and to ensure particle homogeneity. Hydrothermal synthesis can be summarized as a heterogeneous reaction within a subcritical or supercritical aqueous media under conditions which exceed 100

°C and 1 bar in sealed containers for crystal growth, where it also occurs in the natural world during mineral formation and is used industrially in the processing of zeolite and quartz (O'Hare, 2001; Feng and Li, 2017). Hydrothermal solutions generally have better diffusivity which is beneficial for efficient crystal growth on stable crystal nucleus (Feng and Li, 2017). While the hydrothermal solvent concentration, temperature, pressure and residence time can drastically affect the nanostructures being produced, additives can also be added into the system to promote certain structural growth. These additives are inclusive of organic additives, template additives, and substrate additives.

One of the important hydrothermal method which is utilized in metal oxide nanostructure synthesis is the recrystallization of metastable precursors. This hydrothermal synthesis route involves the recrystallization of crystal nuclei sourced from amorphous colloids or nano-crystalline precursors by reacting these precursors with hydroxide ions under high hydrothermal temperatures and pressures (Shi, Song and Zhang, 2013). Another simpler route of metal oxide nanostructure synthesis involves the reshaping of industrial bulk metal oxide powders which by nature has minimal homogeneity to their structures. This can be done by aqueous solution dissolution of bulk metal oxides, and treating the solution with hydrothermal conditions with hydroxide ions to form uniform and homogenous nanostructures (Shi, Song and Zhang, 2013). The hydroxide ions used in both routes can be sourced from alkali mediums like sodium hydroxide (NaOH) and potassium hydroxide (KOH) solutions. These routes have been used extensively by researchers in synthesizing TiO₂ nanostructures due to their simplicity. Some of the examples are the synthesis of TiO₂ nanotubes and nanorods using NaOH and KOH as medium (Keerthana, et al., 2018), TiO₂ nanosheets synthesis of graphene-TiO₂ nanotube composites (Perera, et al., 2012), and the synthesis of TiO₂ nanoparticles which organizes into films with ammonium hydroxide (Burnside, et al., 1998). Alternative solvents inclusive of acidic solvents and TiO₂ precursors can also be used during hydrothermal synthesis as shown in the synthesis of anatase TiO₂ nanosheets with higher concentrations of facet (001) using hydrofluoric acid and tetrabutyl titanate (Han, et al., 2009), and synthesis of hollow anatase TiO₂ nanospheres using titanium fluoride and hydrofluoric acid (Yang and Zeng, 2004).

As mentioned earlier, hydrothermal synthesis processes can be further enhanced with the assistance of additives, where either organic compounds are added to form templates for the growth of certain crystalline structure, or the direct usage of templates itself to achieve similar effects. One of the examples is the addition of surfactants as templates was demonstrated by Zhou, et al. (2006) where the addition of polyethylene glycol with zinc species under hydrothermal conditions would induce polyethylene glycol aggregation, subsequently forming zinc oxide (ZnO) globules that have either rod-like or cone-line ZnO protrusion on the globule surface. Such properties were due to the presence of both hydrophobic and hydrophilic groups on surfactant molecules. Additionally, ethylene glycol itself may be beneficial in forming complex three-dimensional structures of TiO₂ due to the presence of hydroxyl groups. Such techniques are known to be alcohol-assisted hydrothermal synthesis. The complex structures are formed by the initial adsorption of alcohol groups onto specific surfaces of metal oxide crystals owing to the presence of hydrogen bonds, and a subsequent growing on the crystal at the adsorption site (Shi, Song and Zhang, 2013). Other materials like ionic liquids which similarly to surfactants, have both hydrophobic and hydrophilic groups can aid in complex structural formation too as shown in Jiang, et al. (2005) using 1-butyl-3-methylimidazolium tetrafluoroborate ionic liquid. Although the techniques discussed previously did not involve the removal of templates, such methods did in fact exist. Peng, Dong and Li (2003) demonstrated that semiconductor hollow microspheres could be formed hydrothermally using nitrogen microbubbles itself where the microbubbles act as attachment sites for zinc selenide and disappear when the microsphere synthesis was completed. Titirici, Antonietti and Thomas (2006) utilized another route in hollow sphere hydrothermal synthesis by growing metal oxides on carbon spheres before calcinating the material to remove the carbon sphere template and leaving behind only the hollow metal oxide spheres.

In addition to hydrothermal synthesis, sol-gel synthesis is also one of the popular techniques in making nanostructural TiO₂ particles. Sol-gel technique involves the transformation of TiO₂ into a colloidal solution using organic solvents to form nanoparticles also known as sol, and specific conditions are applied to allow the evaporation of the excess solvents. This leaves behind a

network of linked nanoparticles known as the gel with the final product being a porous material with nano-sized pores and nano-sized TiO₂ particles (Sharma, 2010). This technique generally involves lower temperature as compared to hydrothermal synthesis, but requires the usage of large amounts of expensive organic solvents with long processing time, and produces highly amorphous TiO₂ that requires recrystallization to have better photocatalytic properties. The hydrolysis of titanium isopropoxide to produce TiO₂ particles as demonstrated by Mahshid, Askari and Ghamsari (2017) is also an alternative synthesis method that has more control on particle size and shape as compared to sol-gel synthesis. Other remaining methods of TiO₂ synthesis involves the utilisation of plasma as shown in the works of Liu, et al. (2013) in synthesizing TiO₂ nanoparticles with gliding arc warm plasmas, and Kim, et al. (2018) where plasma-assisted electrolysis is used to produce TiO₂ nanoparticles from bulk materials that are industrially suitable.

2.2.3 Titanium Dioxide Modifications

The primary aims of TiO₂ modification involves the reduction in photo-generated electron-hole recombination, visible light sensitizing of TiO₂, and the improvement of overall photocatalytic efficiency. While many researchers have been developing ways of TiO₂ modifications, the doping of TiO₂ with other materials remain one of the most fundamental ways of improvement. Doping can be done with either cationic or anionic materials depending on the nature of the desired application. Cationic doping involves the doping of TiO₂ with metals such as rare earths, transition metals, post-transition metals and noble metals. Metallic doping was found to be sometimes beneficial if the right amount of dopant is used due to the enhancement of electron-hole separation and the extension of photocatalytic activity towards the visible light region (Daghrir, Drogui and Robert, 2013). On the other hand, anionic doping involves the doping of non-metals within TiO₂ matrices to achieve similar effects, with an exception that non-metal dopants are least prone to become electron-hole recombination centers as compared to cationic dopants. Fundamentally, the incorporation of ions into the TiO₂ matrix introduces the new energy levels from the ions to the existing energy levels of TiO₂, in which electrons are able to jump to these new energy levels from the valence band, or can be donated from

these new energy levels to the conduction band. This reduces the energy required by a photon to excite electrons in the valence band of the doped material to the conduction band due to the reduction in energy level separation, hence allowing visible light induced photocatalysis. Metals from the lanthanide group were reported to be able to create electron and hole traps in addition to impurity state introduction (Bingham, and Daoud, 2011). Similar effects can also be achieved in transition metal doped TiO₂ (Zaleska, 2008). Noble metal doping shares similar positive effects of lanthanide doping, with other advantages like the increment in localized electromagnetic field that can polarize adsorbed molecules and decrement in the diffusion length of electron-hole pairs (Prakash, et al., 2018). However, inappropriate amounts and type of dopant used may result in negative alteration of TiO₂ surfaces and electronic properties which can deteriorate photocatalytic activity and thermal stability (Daghrir, Drogui and Robert, 2013).

Other alternatives in modifying TiO₂ involves the manipulation of TiO₂ morphology in attaining desired structural and surface properties which are more effective for photocatalytic degradation. One of the simplest ways of doing this is to allow the formation of both rutile and anatase phase TiO₂ in optimized ratios to facilitate the charge separation with reduced band gap energies on specific surfaces in order to promote photocatalytic activity (Djurisic, Leung and Ng, 2014). Methods like the synthesis of TiO₂ micro and nanostructures which improves both surface area and charge separation are also seen in works of Singh, et al. (2019) in developing sub-micron rutile-anatase TiO₂ balls, Asl, Saed and Sadrnezhaad. (2019) in synthesizing TiO₂ nanorod and nanoflowers, and Singh, et al. (2017) in making nanostructured TiO₂ films. Additionally, researchers have also been developing ways to selectively synthesize TiO₂ selectively with high ratios of desired facets in order to improve TiO₂ surface reactivity for specific applications like the synthesis of facet (001) dominant TiO₂ nanosheets for photocatalytic hydrogen evolution (Sui, et al., 2019), and the manipulation of TiO₂ film crystal texture and orientation for better photocatalytic properties (Tuckute, et al., 2019). Wang, et al. (2017) reported that the presence of bulk defects should also be taken into account as defects can act as charge traps which can promote electron-hole recombination.

As a result, proper annealing process should be used to modify TiO₂ to prevent the accumulation of these defects in order to promote photocatalytic efficiency.

2.3 Characterisation of Titanium Dioxide

Synthesized TiO₂ can be subsequently characterized with instruments to determine its surface morphology, particle size, surface areas, functional groups, crystal structure and phase that are unique to TiO₂. The surface morphology of TiO₂ particles can be preliminarily examined by SEM. However, to determine the amount of crystal structure and phases that are present in any TiO₂ samples, the XRD analysis will be used as shown by Figure 2.11 TiO₂ calcined at different temperatures. It could be observed that the transformation of anatase (a) to rutile (r) phase occurred at high calcination temperature due to the stability of rutile at high temperatures owing to energy being absorbed to undergo reconstructive phase transfer from anatase to rutile which involves the breaking reforming of TiO₂ bonds (Hanaor and Sorrell, 2011).

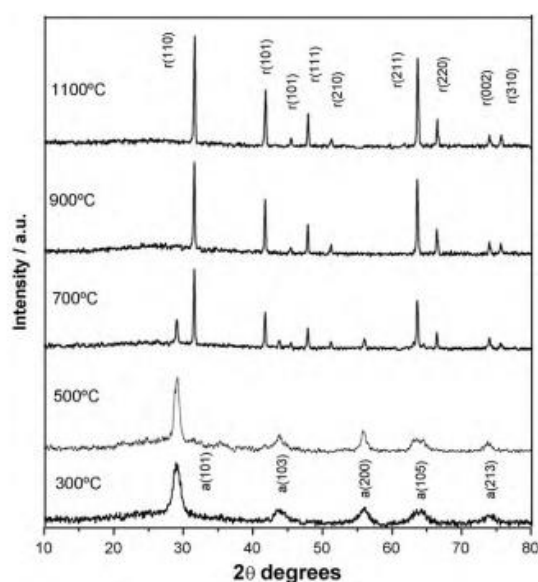


Figure 2.11: XRD patterns of TiO₂ Calcined at Various Temperatures (Viana, Soares and Mohallem, 2010).

In addition to crystal phases, XRD analysis are able to determine the amounts of different reflective planes which are present on the TiO₂ samples. Each reflective plane is a particular facet of TiO₂ that is represented by a peak where the associated peak intensity is directly correlated to its amount.

Furthermore, the peak intensities obtained from the XRD can also be used to estimate particle size of TiO_2 using the Debye-Scherrer equation.

In order to reconfirm the presence of TiO_2 , the UV-visible spectrometry (UV-Vis) and the FTIR can be conducted. TiO_2 will have a UV-Vis absorption between 300 nm to 800 nm (Sharfudeen, Latheef and Ambrose, 2017). The FTIR further confirms the presence of TiO_2 if a significant peak around 511.9 cm^{-1} which represents the vibration of Ti-O-Ti groups of TiO_2 (Viana, Soares and Mohallem, 2010). The large absorption band within this region can also be correlated to a large particle size distribution. FTIR spectrum for TiO_2 also involved the hydroxyl group stretching at around 3414.66 cm^{-1} , and peak at around 751.42 cm^{-1} again due to the Ti-O-Ti bond (Sharfudeen, Latheef and Ambrose, 2017). Additionally, the thermogravimetric analysis (TGA) can be used to determine the presence and the amount of residual solvents and moisture that are remained in the TiO_2 sample. Zoccal, Arouca and Goncalves (2010) TiO_2 synthesized using the hydrolysis route would retain moisture within the material, where an abrupt loss of mass could be spotted between $250 \text{ }^\circ\text{C}$ and $480 \text{ }^\circ\text{C}$ as shown in Figure 2.12 due to vaporization of water molecules (Zoccal, Arouca and Goncalves, 2010). DTA results also showed an exothermic profile between $250 \text{ }^\circ\text{C}$ and $480 \text{ }^\circ\text{C}$, where Zoccal, Arouca and Goncalves (2010) postulated that it is due to the breaking of bonds upon the release of water molecules during the process of vaporization.

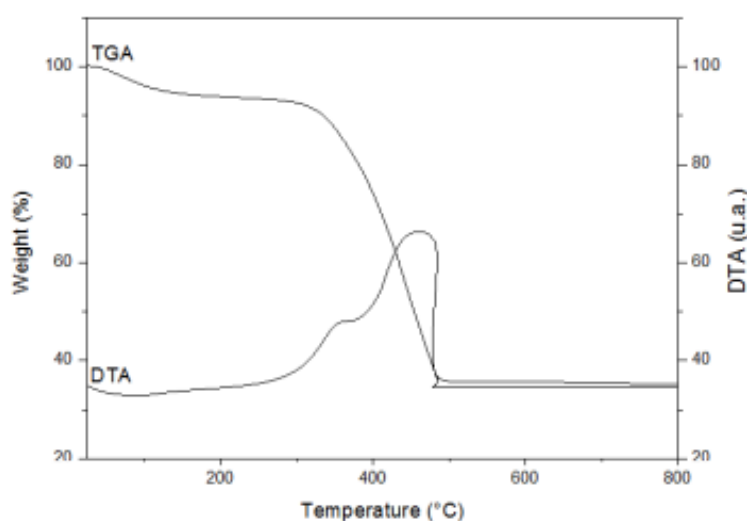


Figure 2.12: TGA and Differential Thermal Analysis (DTA) of TiO_2 Synthesized via the Hydrolysis Route (Zoccal, Arouca and Goncalves, 2010).

In terms of the surface area and pore size studies of TiO₂, the TPD can be used. The TPD functions by allowing adsorption of an inert gas onto the surfaces of TiO₂ where the adsorption pattern will be initially recorded, followed by the desorption of these gasses from the surface of TiO₂ where the desorption pattern will be similarly measured under isothermal conditions. The sample results of this analysis is shown at Figure 2.13 where the Langmuir isotherms for TiO₂ showed difference in adsorption and desorption profile caused by hysteresis. The hysteresis phenomena is classified as a type IV(a) Langmuir isotherm where mesopores are present in the TiO₂ nanostructure which is caused by delayed desorption process caused by multi-layer adsorption and the insufficient pore size for the desorbed species to escape (Sotomayor, Cychosz and Thommes, 2018).

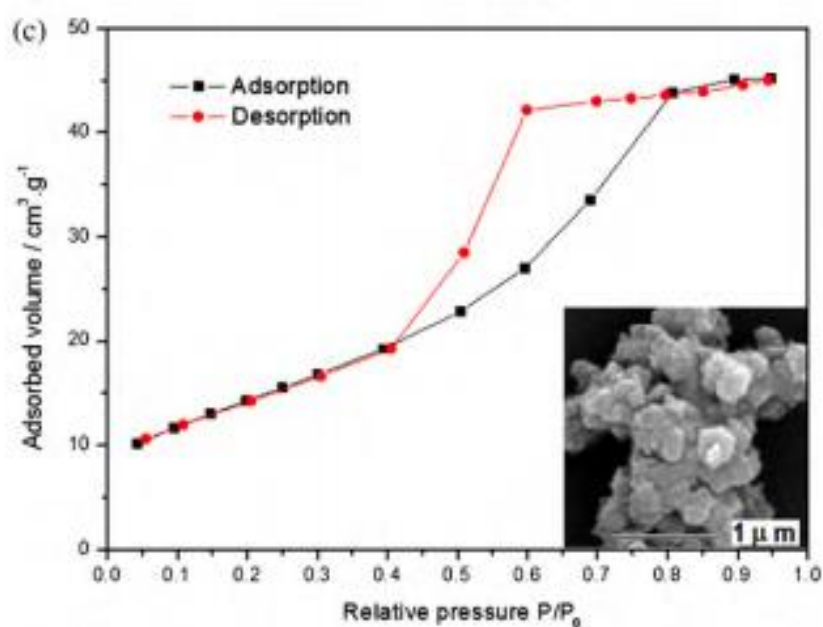


Figure 2.13: Langmuir Isotherm of TiO₂ Calcined at 500 °C (Viana, Soares and Mohallem, 2010).

2.4 Organic Dyes

Organic dyes are organic molecules which fall in the classification of having the ability to absorb visible light from 400 nm to 700 nm. Organic dyes possess at least one colour causing chromophore group, have conjugated bonding systems like alternating double and single bonds, and shows electron resonance (Ambrogi, et al., 2017). Additionally, most organic dyes have colour helpers

which are known as auxochromes. Auxochromes are used to shift the colour of the dye and control dye solubility (International Agency for Research on Cancer, 2010). While synthetic organic dyes provide colourant superiority as compared to inorganic dyes, they are found to be oxidation and biodegradation resistant, and some even pose serious health risks to humans especially for aromatic amine group containing dyes (Butun, et al., 2017). As compared to other organic dyes, azo dye was reported to account for 65 % of the commercial organic dye production due to its many colours that can be incorporated in a variety of goods. However, it poses a significant problem when it comes to its degradation especially from the perspective of aromatic amine group production as shown in Figure 2.14 (Ahlstrom, et al., 2005). Azo dye is extremely resistant to aerobic degradation and can only be degraded anaerobically via reductive cleavage by specific enzymes. The conventional degradation route involves the formation of highly carcinogenic aromatic amine groups. Such degradation routes are also found in the metabolic pathway of humans upon azo dye ingestion, hence posing a serious health threat.

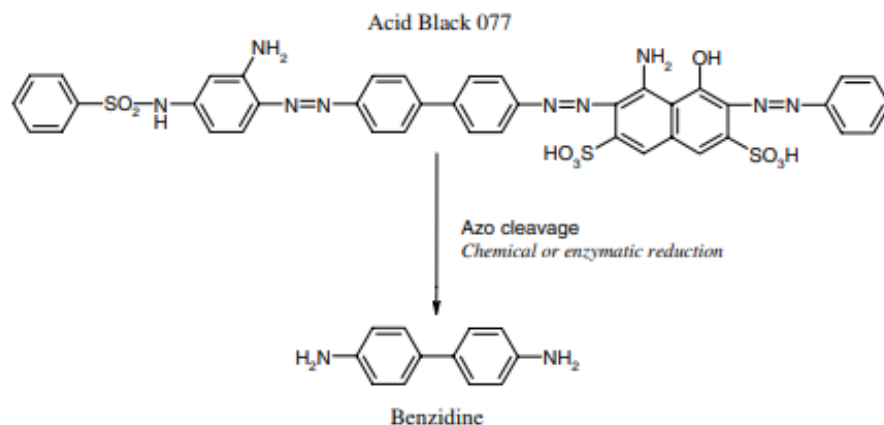


Figure 2.14: Anaerobic Reductive Cleavage of Azo Dye (Ahlstrom, et al., 2005).

Organic dye can be classified into 17 different groups as shown in Table 2.1. Table 2.1 displays the identification of specific dyes and their respective examples structurally.

Table 2.1: Types of Synthetic Organic Dyes (Ziarani, et al., 2018).

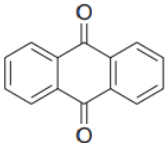
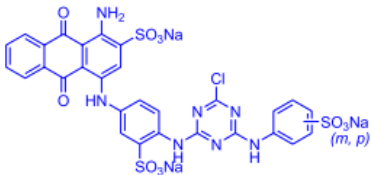
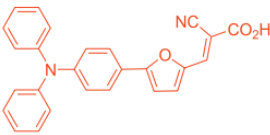
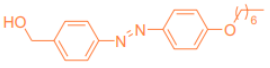
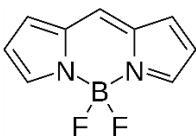
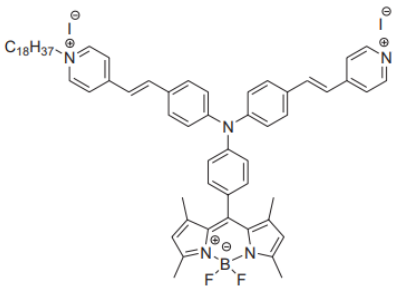
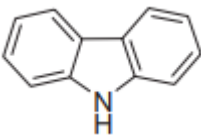
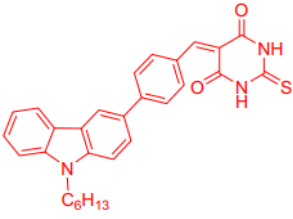
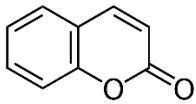
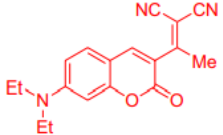
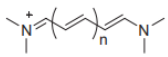
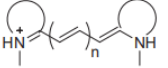
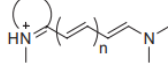
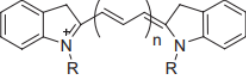
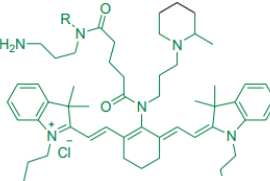
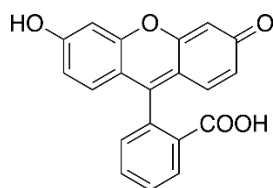
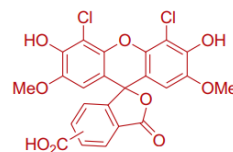
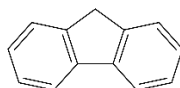
Dye Group	Identifier	Examples
Anthraquinone	 Anthraquinone	
Amine	$R-N\begin{matrix} R'' \\ R' \end{matrix}$ Amine group	
Azo	$-N=N-$ Azo Group	
Boron-Dipyrromethane	 Boron dipyrromethane	
Carbazole	 Carbazole	
Coumarin	 Coumarin	
Cyanine	    Polymethine groups	 CyR 4

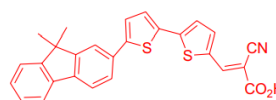
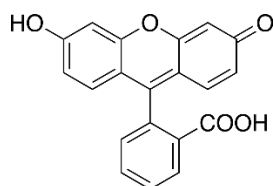
Table 2.1 (Continued)

Fluorescein

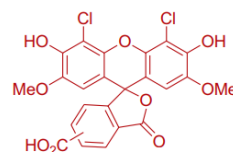
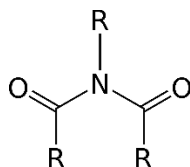
Fluorescein

**Fluorene**

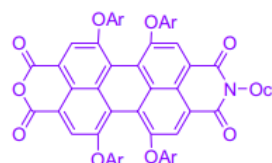
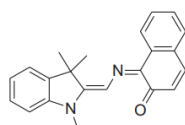
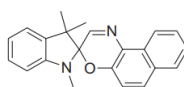
Fluorene

**Fluorescein**

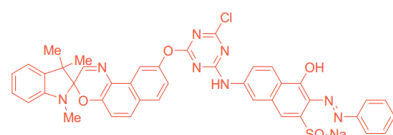
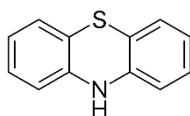
Fluorescein

**Imide**

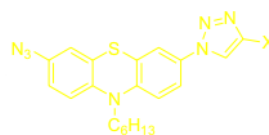
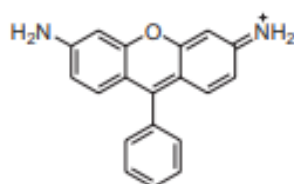
Imide group

**Oxazine**

Spirooxazine

**Phenothiazine**

Phenothiazine

**Rhodamine**

Rhodamine

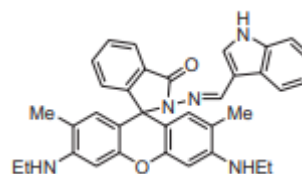
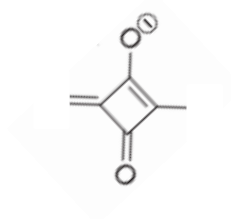
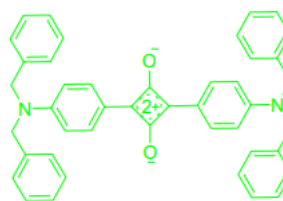
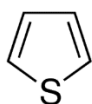


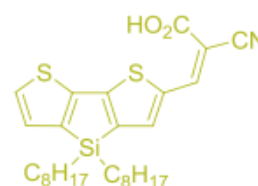
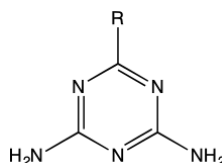
Table 2.1 (Continued)

Squaraine

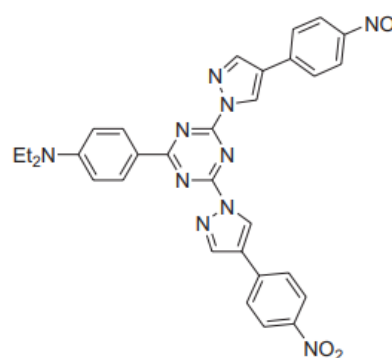
Four carbon ring derived
from squaric acid

**Thiophene**

Thiophene

**Triazine**

Triazine

**2.4.1 Production of Organic Dyes**

Azo dyes are widely utilized in the industry especially in the fabric and textile dyeing process. The synthesis route of azo dyes are relatively straightforward as shown in Figure 2.1. Initially, an aromatic amine or diazonium compound undergoes diazotization using hydrochloric acid, followed by the azo coupling of other aromatic groups to form the chromophore (Waring, 1984).

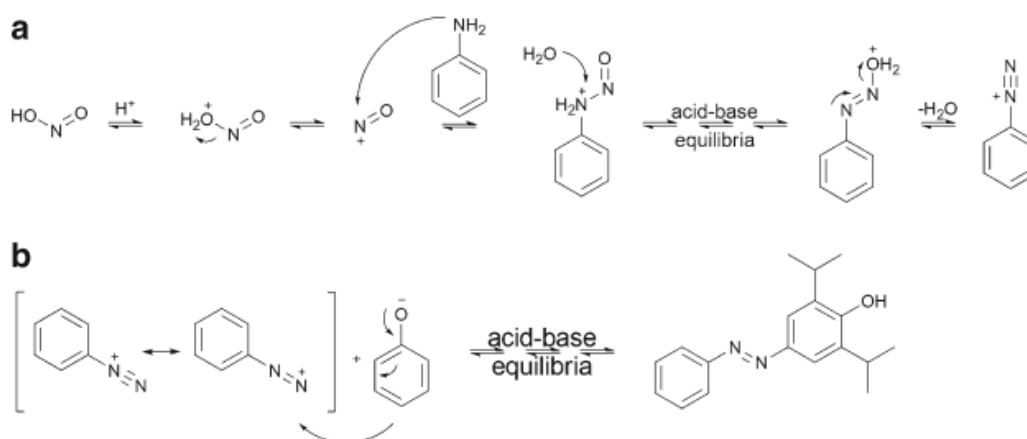


Figure 2.15: Diazotization of Aromatic Amine (a) followed by the Azo Coupling Reaction (b) to form Azo Dye (Vaiano, Mari and Busardo, 2014).

Industrially, synthetic dye production processes involve three major components, which are the initial chemical synthesis of dye, following by drying of product to produce powder or paste like substance, and lastly, the treatment of effluents resulted from the process itself. The overall process flow is shown in Figure 2.16. Despite the installation of effluent treatment process in dye producing facilities, the discolouration of waste effluent is still posing a significant challenge especially in the production of reactive dyes (Rosa, et al., 2014).

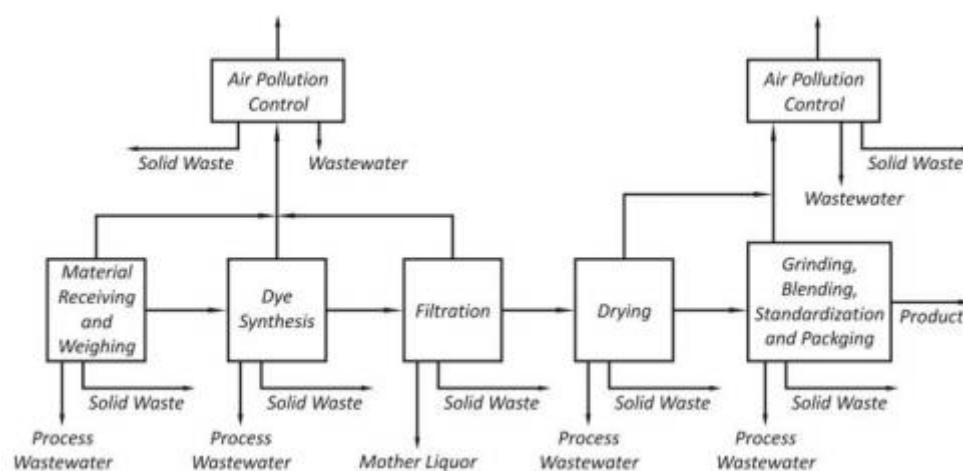


Figure 2.16: Overall Flow of Synthetic Dye Production (Rosa, et al., 2014).

Other challenges that are faced by the synthetic dye producing industry are the huge consumption of water and persisting environmental problems

caused by industrial waste water output. As a result, AOP processes are being developed to promote selective degradation of recalcitrant organic pollutants that are produced by the industry.

2.4.2 Organic Dyes Removal Methods

Synthetic organic dyes cannot be removed by aerobic means and are often toxic to most biodegradation microbes and other living biomass although specific dyes can be biodegraded with a specific set of microbes which reduces treatment flexibility. In terms of microbial degradation, Forgacs, Cserhati and Oros (2004) compiled a list of microbes that are suitable for the degradation of specific dyes. Due to the lacking of flexibility and unforeseen parameters which are hard to be controlled, microbial degradation of synthetic organic dye has yet to be fully industrialized, but remains a promising treatment alternative.

The current dye degradation methods that are available industrially can be classified into two major categories, which are chemical removal techniques and physical removal techniques. In terms of the chemical removal techniques, these methods primarily involve destructive oxidation of dyes, while physical techniques adopt separation processes like filtration and adsorption. The utilisation of Fenton's reagents, ozonation, and photochemical degradation of dyes are several major examples for chemical removal techniques. Physical techniques include membrane filtration, activated carbon adsorption, and ion exchange separation. However, chemical methods pose a greater advantage as compared to the conventional physical methods as physical methods are generally non-destructive, hence requiring regeneration procedures during excessive fouling of filter materials and adsorbents (Konstantinou and Albanis, 2004). Moreover, physical treatment methods require additional treatment processes for the produced sludge thus making them less attractive economically.

As mentioned previously, chemical methods fall under the classification of AOP. Fenton's reagents are concoctions of hydrogen peroxide and iron(II) salts. The mixture of these two components will lead to the decomposition of hydrogen peroxide to form highly oxidative hydroxyl radicals which are effective hydroxylation agents (Goldstein, Meyerstein and Czapski, 1993). The radicals produced will then be used to mineralize the suspended dye particles to

produce water and carbon dioxide, followed by a subsequent coagulation and flocculation of the residual reagents and dye fragments. However, the method was reported to have inferior results on vat and disperse dyes in terms of degradation, and does not produce effective settling flocs for vat dyes (Robinson, et al., 2001; Xu, et al., 2004). Additionally, reactive, direct, mordant and acid dyes were also reported to form flocs which are unlikely to settle despite having superior degradation efficiency over vat dyes. The ozonation technique follows a similar pathway in terms of dye degradation mechanism via the generation of radicals. Generally, ozonation involves the reaction of ozone molecules with hydroxide ions, producing highly oxidative superoxide and hydroperoxyl radicals (Shriram and Kanmani, 2014). Moreover, this technique can be assisted via UV irradiation to produce additional hydroxyl radicals to facilitate the degradation process. Ozonation has a comparative advantage relative to the Fenton process due to both dye decolourization effectiveness and no sludge formation. However, ozone has a residence time of only about 20 minutes and may be lesser under acidic conditions with the presence of inorganic salts and high dye concentrations (Shriram and Kanmani, 2014; Robinson, et al., 2001). By-product formation owing to the radicalism of ozonation is also another major disadvantage. Comparatively, the photochemical technique is a simplified version of the Fenton technique where hydrogen peroxide decomposition is performed to produce radicals catalysed by UV radiation instead of ferrous cations. As a result, similar to ozonation, no sludge is produced but formation of by-products remains a problem (Robinson, et al., 2001). Furthermore, UV-hydrogen peroxide systems without catalytic assistance are only effective in treating low dye concentrations (Silva and Faria, 2003).

In addition to the mentioned chemical techniques, the utilisation of photocatalytic materials have also been popularized due to their effectiveness in dye degradation. Based on Konstantinou and Albanis (2004), the photocatalytic degradation of azo dyes using TiO_2 was found have relatively better destructive power as compared to ozonation, Fenton process and photochemical degradation. Additionally, photocatalysis reaction do not require reagents with high oxidative power, and is only dependant on materials that are abundantly available, which are solar irradiation, water, and oxygen. TiO_2 is also relatively cheap as compared to other oxidative reagents due to its abundance in nature,

chemically stable, and has low environmental toxicity (Ram, Andreescu and Ding, 2011). Another apparent advantage of using photocatalysis in dye degradation is the sensitization of dyes. Konstantinou and Albanis (2004) provided the mechanism for dye sensitization which involves the initial absorption of visible light by a dye to reach its excited state. The excited dye then forms a cationic dye radical by the donating an electron to the conduction band of TiO_2 which behaves similarly like photoelectron generation. Subsequently, TiO_2 that bears the extra electron will react with oxygen to form superoxide radicals which then degrades the dye. Simultaneously, the cationic dye radical reacts with hydroxide ion to form hydroxyl radicals, hence returning the dye radical to its ground state while producing more radical species for dye degradation. As a result, the synergistic effect between dye and TiO_2 could accelerate the separation of electron-hole pairs to produce oxidative radicals, and offers two distinct routes of radical production with different redox potentials (Hilal, et al., 2007).

2.5 Ultrasonic Irradiation and Sonoluminescence

The spur of the field of ultrasonic chemistry originates from the ability of high intensity ultrasonic waves to cause acoustic cavitation in liquids. During the cavitation of liquids, meta-stable microscopic gas bubbles are formed which will then be compressed adiabatically by the surrounding liquid and collapse violently, causing the exponentiation of temperature at the epicentre of the phenomena (Flint and Suslick, 1991). The release of a single pulse of light can then be observed from the geometrical centre of the cavitation bubbles. Such effects are known as sonoluminescence. Gaitan, et al. (1992) stated that during acoustic cavitation, the expansion of bubbles is promoted by rectified diffusion, while its rapid subsequent collapse can be attributed to the impact of surface waves and hence causing a sudden bubble fragmentation. Additionally, they also found out that optimal and detectable sonoluminescence emission can be found when the bubble size ranges from 15 microns to 20 microns which can be induced by ultrasonic waves of 20 kHz, and has to reach a collapse temperature of at least 2000 K to 3000 K. The produced luminescence ranges from the visible region towards the UV region whilst having an incremental continual spectral energy density pattern (Yasui, et al. 2004). Mechanistically,

acoustic cavitation occurs within the liquid bulk at the antinodes of the ultrasonic waves that have amplitudes of greater than 1 atm, which causes local pressures to become negative. At positions of negative pressure, the liquid element stretches outwards causing a sudden drop in gas solubility within its bulk leading to sudden local vaporization of these gasses.

Popularly, two distinct models have been outlined by researchers to explain sonoluminescence, which are the single-bubble sonoluminescence (SBSL) and multi-bubble sonoluminescence (MBSL). In SBSL, a stable single bubble is said to be located at the antinode of an ultrasonic wave, and collapses at each ultrasonic wave period to emit sonoluminescence which can persist for days under steady state conditions (Yasui, et al., 2004). Within the bubble itself, higher pressures and temperatures can cause weak ionization of vapour within to form plasma. Electrons resulted from the ionization process then move within the plasma rapidly and randomly, causing collisions with other neutral atoms and cations while some recombine with the orbits of cations. These phenomena cause a sudden electron deceleration and lead to the release of bremsstrahlung radiation that will be detected as sonoluminescence. However, at cases of MBSL, in addition to the phenomena of SBSL, the chemiluminescence of formed hydroxyl radicals are also seen at relatively high ultrasonic amplitude, and is said to be the dominant mechanism of luminescence (Yasui, et al., 2004). An excellent review of the current physical models that are used to predict bubble dynamics and the release of sonoluminescence can be obtained from Brenner, Hilgenfeldt and Lohse (2002).

2.5.1 Sonolysis

Sonolysis is an AOP which employs the technique of ultrasonic irradiation for water splitting and the radicalization of dissolved gases to produce highly reactive radicals that can be used chemically. During acoustic cavitation, the pinpoint locations within the water bulk with extreme temperatures and pressures are formed as the microscopic bubbles collapse. This causes several interesting bond cleavage reactions of water and diatomic gases and form hydroxyl, monoatomic oxygen and monoatomic nitrogen radicals (Torres-Palma and Serna-Galvis, 2018). These radicals can then further react with species that are present in water to undergo recombination to form neutral

elements, and the formation of other oxidative species like nitric acid and hydrogen peroxide. However, the type of radical formation can be altered by changing the type and amount of dissolved gases within the liquid bulk as shown by Kohno, et al. (2010). Sonoluminescence and the pyrolysis of organic compounds are also seen throughout the process. In terms of degradation of organic pollutants, the utilisation of sonolytic pathways is able to convert long hydrocarbon chains into short ones, and also possible mineralization of these organic compounds to form carbon dioxide and water. The sonolytic degradation pathway consists of two routes as shown in Figure 2.17, which are the thermal route and the radical route. Extremely hydrophobic and non-volatile organic compounds which are resistant to hydroxyl radicals are typically decomposed via thermal pyrolysis caused by the extreme pinpoint temperatures, while the remaining compounds can be degraded either thermally or via hydroxyl radicals (Torres-Palma and Serna-Galvis, 2018). As a result, sonolysis can be used in a variety of waste treatment processes, which includes the degradation of azo dyes (Okitsu, et al., 2005), ibuprofen degradation in waste water (Adityosulindro, et al., 2017) and pre-treatment for solid organic waste anaerobic digestion (Cesaro and Belgiorno, 2013).

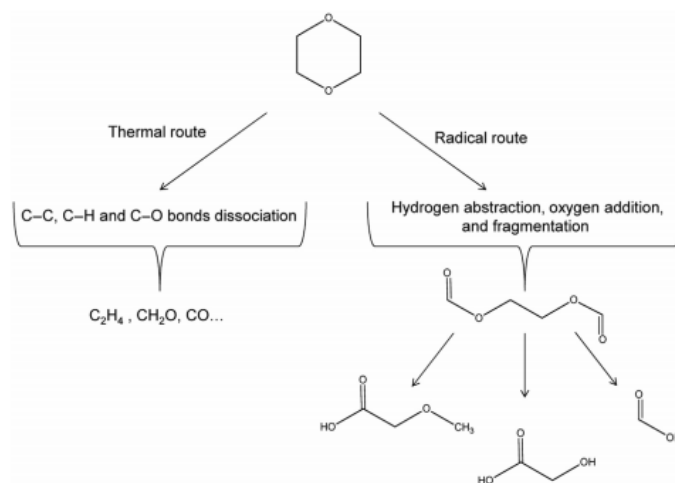


Figure 2.17: Sonolytic Degradation of Organic Compounds (Torres-Palma and Serna-Galvis, 2018).

2.5.2 Sonocatalysis

Sonocatalysis involves the amalgamation of sonolysis and photocatalysis into a single synergistic method in order to increase the overall number of hydroxyl radicals produced for degradation of organic pollutants (Kuna, et al., 2017). Such incorporation allows a dual-pathway degradation system which can be induced by both ultrasonic waves and solar UV radiation. This is found to be superior in terms of degradation efficiency as compared to isolated systems (Vinu and Madras, 2009). Additionally, Ogi, Hirao and Shimoyama (2002) demonstrated that due to the spectral resemblance of bremsstrahlung UV radiation emitted via the SBSL route to the UV absorption spectra of TiO₂, the sonoluminescence produced by SBSL acoustic cavitation is able to activate the photocatalytic properties of TiO₂. Qiu, et al. (2018) provided an alternative mechanism which involves the nucleation of bubbles at the surface of solids resulted by acoustic cavitation as depicted in Figure 2.18. The mentioned mechanism can be achieved by increasing surface roughness, porosity and hydrophobicity to reduce energy barrier for the formation of bubble cavitation.

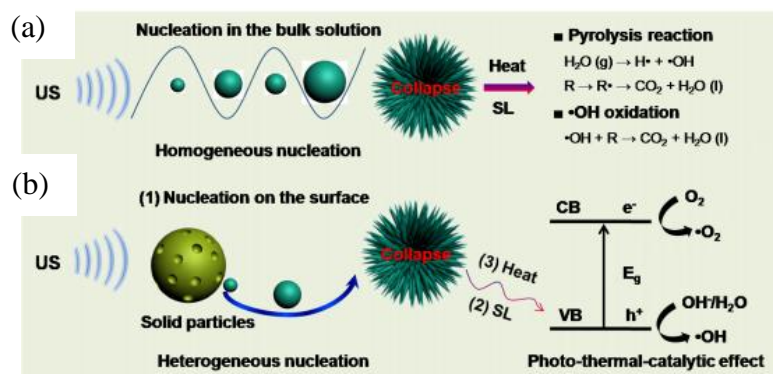


Figure 2.18: (a) Homogenous Acoustic Cavitation versus (b) Heterogeneous Acoustic Cavitation (Qiu, et al., 2018).

In terms of the ultrasonic intensity, Eren and Ince (2010) observed that ultrasonic of low frequency is much more efficient in terms of dye degradation as compared to high ultrasonic frequency regardless of the dye structure in the presence of nanostructured TiO₂. The benefits of low ultrasonic frequency are attributed to the formation of bubble with long half-life, hence inducing high bubble implosion temperatures and stronger sonoluminescence intensity.

CHAPTER 3

METHODOLOGY AND WORK PLAN

This section contains all the materials involve in the synthesis of the TiO₂/cellulose composite catalyst. Additionally, the methodology for the extraction of cellulose from EFB was outlined followed by the hydrothermal synthesis process of the composite itself. Lastly, the characterization methods were further discussed to examine both the physical and chemical properties of the synthesized product.

3.1 Materials and Chemicals

Initially, the chemicals that were used in the EFB extraction process, hydrothermal synthesis reagents and target pollutant are be outlined in Table 3.1.

Table 3.1: Materials Involved in the EFB Cellulose Extraction Process, Synthesis of TiO₂/Cellulose Composite Material and Catalytic Activity Study.

Material	Grade	Supplier	Usage
Alconox® detergent	-	Merck	Cellulose extraction,
Deionized water	-	-	hydrothermal synthesis and catalytic activity study
Ethanol ≥99.8 %	ACS Reagent	Merck	Cellulose extraction and hydrothermal synthesis
Sodium hydroxide (NaOH) ≥97 %	ACS Reagent	Merck	Cellulose extraction
Hydrogen peroxide (H₂O₂) 30 wt. % in H₂O	ACS Reagent	Merck	Cellulose extraction
Formic acid ≥95 %	Reagent Grade	Merck	Cellulose extraction

Table 3.1 (Continued)

Titanium(IV) isopropoxide 99.999 %	-	Merck	Hydrothermal synthesis
Congo Red ≥ 35 %	-	Merck	Catalytic activity study
Triethylamine	-	Merck	Hydrothermal synthesis

3.2 Overall Experimental Flowchart

Figure 3.1 depicts the overall experimental flowchart for the preparation of the composite material samples, followed by the subsequent characterisation and catalytic activity examination procedures.

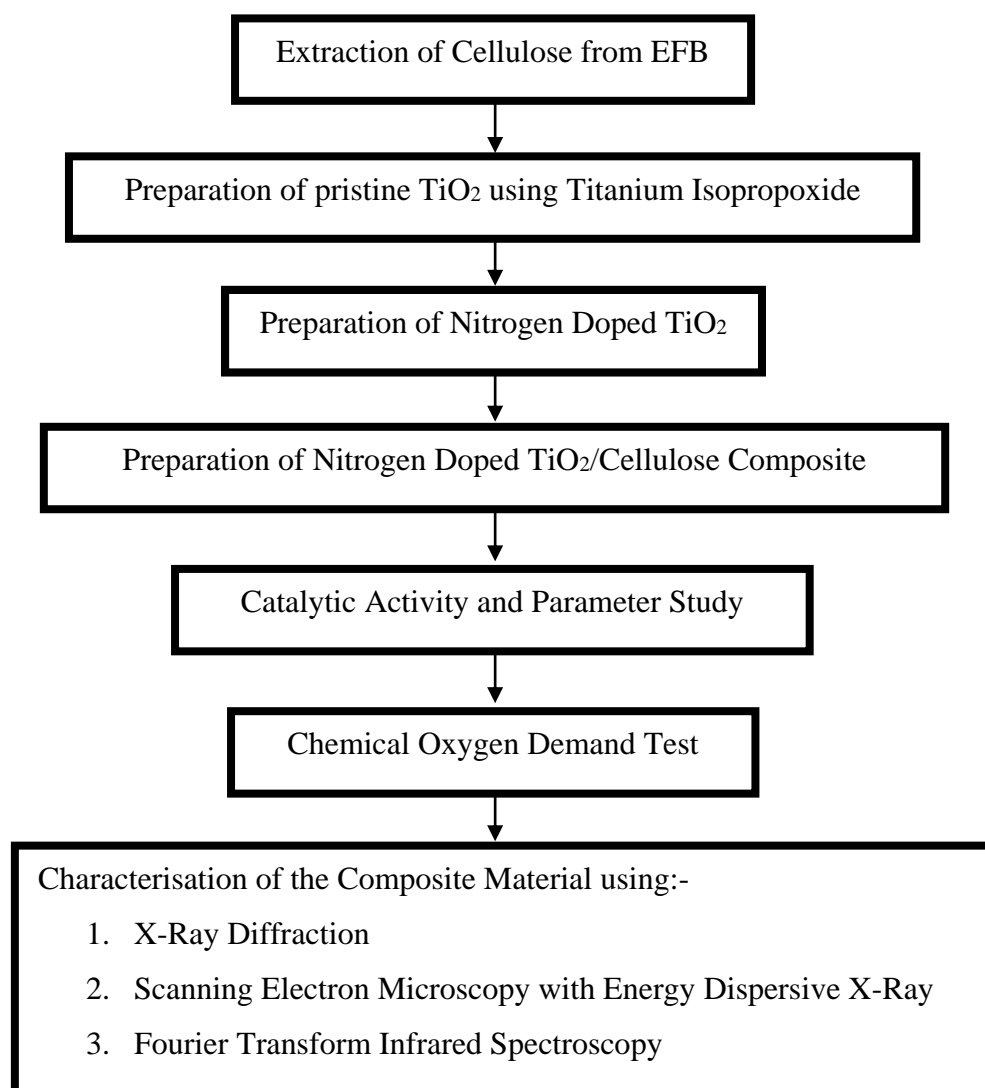


Figure 3.1: Overall Experimental Flowchart.

3.3 Preparation of Cellulose, Titanium Dioxide and Composite Materials

Cellulose was initially extracted from the EFB by firstly cleaning the obtained EFB to remove residual oils and hidden dirt particles, followed by drying and de-waxing of the cleaned fibres. The lignin that was present within the fibres were further removed from the fibres via the autoclaving of the suspension made by mixing the cleaned and de-waxed EFB with NaOH. Subsequently, pristine titanium dioxide samples were prepared by hydrothermally treating solutions made from dissolving titanium isopropoxide of various quantities into ethanol. Additionally, the composite material samples were prepared by dropping solutions made from dissolving titanium isopropoxide of various quantities into ethanol into cellulose suspensions. The obtained suspensions were then treated under similar hydrothermal conditions to yield the composite materials.

3.3.1 Cellulose Extraction from Empty Fruit Bunch

The extraction of cellulose from EFB were separated into two phases, beginning with the pre-treatment of the EFB and followed by the extraction process.

Initially, the fibre branches were separated from the mother EFB physically via mechanical means. The fibres were then continuously rinsed with a solution made with 1 % detergent in order to remove any residual oil based components and trapped dirt. Such rinsing was done until the used solution turned colourless from a brownish hue. Subsequently, the cleaned fibres were dried using an oven under the condition of 100 °C with a tolerance of 2 °C until the attainment of a constant weight, and were further milled mechanically into minute pieces with an average size of 0.2 mm. The dried fibres were then de-waxed with 200 mL of 70 vol% ethanol where the ratio for de-waxing was one part fibre to ten parts ethanol solution in a soxhlet apparatus for 6 hours. After the de-waxing procedure, the fibres were then rinsed again with deionized water to eliminate residual ethanol before drying in an oven and repeat the steps until a constant weight was been attained. 10 g of dried de-waxed fibres were then suspended in 100 mL of 10 % NaOH for 24 hours. Finally, the NaOH soaked fibres were transferred into 100 mL of 10 % H₂O₂ and was covered with a layer of aluminium foil before being autoclaved under the conditions of 121 °C (Nazir, et al., 2013). As a result of the autoclave, the dark brown liquid soaking the

treated fibres were disposed. The fibres were then washed with deionized water again continuously until the washing liquid produced was clear and colourless.

The extraction of cellulose from the treated fibres were done by initially soaking the autoclaved fibres in a solution made out of 50 mL of 20 % formic acid and similar quantities of 10 % H_2O_2 for two hours to remove the lignin constituent (Nazir, et al., 2013). The fibres were then filtered out and were rinsed again with 10 % formic acid, followed by deionized water. Subsequently, the fibres were again suspended in 10 % H_2O_2 at 60 °C for 1.5 hours. Note that the pH of the H_2O_2 were adjusted to pH 11 via 10 % NaOH prior to the suspension of the fibres. Finally, a white suspension was produced and was filtered out and washed with deionized water to produce an insoluble substance, which was α -cellulose.

3.3.2 Preparation of Titanium Dioxide

The preparation of TiO_2 without the addition of cellulose was done by taking titanium isopropoxide of 10 mL to be dissolved into 25 mL of 99.9 % ethanol (Chauhan and Mohanty, 2014) and 40 mL of distilled water under simultaneous stirring for 30 minutes. The suspension was then heated to 120 °C for 13 hours in an oven inside a Teflon stainless steel hydrothermal reactor vessel.

3.3.3 Preparation of Nitrogen Doped TiO_2

The preparation of nitrogen doped TiO_2 (N- TiO_2) was done by mixing 10 mL of titanium isopropoxide, 25 mL of 99.9 % ethanol and 40 mL of distilled water with 2.38 mL of triethylamine as the nitrogen dopant. The used amount of triethylamine constituted a titanium to nitrogen molar ratio of 2 (Cong, et al., 2007). As per Cong, et al. (2007), the use of the stated molar ratio and triethylamine promises maximum N- TiO_2 performance as compared to other nitrogen dopants.

3.3.4 Hydrothermal Synthesis of Composite Material

The hydrothermal synthesis of the composite material involved immobilization of N- TiO_2 particles onto the previously extracted α -cellulose from the EFB. 22.6 mg, 113 mg, 226 mg, 452 mg and 678 mg of α -cellulose which corresponded to 1 wt%, 5 wt%, 10 wt%, 20 wt% and 30 wt% of cellulose loading were firstly

suspended and dispersed in 40 mL of deionized water mixed with 25 mL of 99.9 % pure ethanol (Chauhan and Mohanty, 2014). 10 mL of Titanium isopropoxide and 2.38 mL of triethylamine were then respectively added to each sample. Note that titanium isopropoxide was added drop by drop into their respective cellulose suspension made previously and the final suspensions were continuously stirred for 30 minutes under ambient conditions. As a result, 5 hydrothermal solution sets were prepared, where each set was stored in a Teflon stainless steel hydrothermal reactor vessel and heated in an oven at 120 °C for 13 hours. Finally, the hydrothermally treated suspensions were cooled at ambient conditions, and the final suspensions were all washed with 99.9 % ethanol until clean.

The composite material with the best sonocatalytic organic dye degradation were then re-synthesized under the hydrothermal temperatures of 100 °C, 120 °C, 140 °C, 160 °C and 180 °C at similar hydrothermal residence time to produce 5 sets of the composite material for further catalytic activity study to determine optimal hydrothermal temperature.

3.4 Experimental Setup for Sonocatalytic Degradation

Figure 3.2 contains the experimental setup for the sonocatalytic degradation of organic dye using the synthesized composite materials.

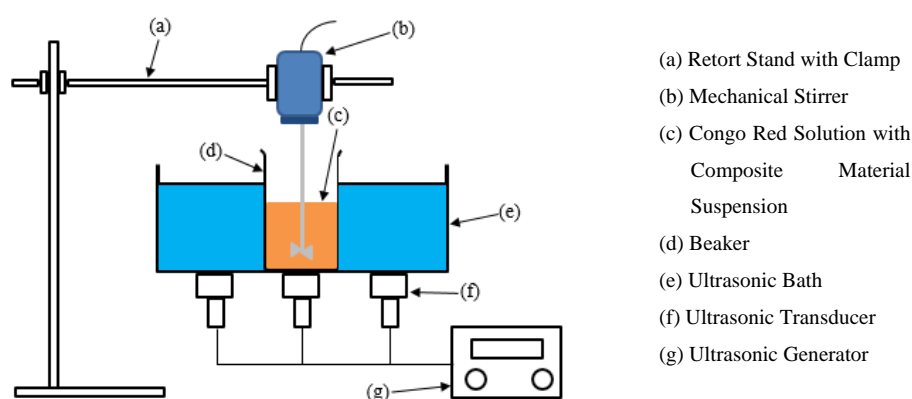


Figure 3.2: Experimental Setup for Sonocatalytic Degradation of Organic Dye.

Initially, 20 ppm of Congo Red was prepared to mimic a dye-infested wastewater. Subsequently, 0.5 g/L of the composite material suspension was added to the organic dye containing wastewater, and was continuously stirred

for 1 hour to achieve equilibrium adsorption-desorption condition. The suspension was then placed in an ultrasonic bath with the rating of 35 kHz and 50 W for 1 hour. The liquid sample was collected every separate 10 minutes and a syringe filter was used to separate the composite material from the wastewater instantaneously. The treated wastewater will then be tested with UV-Vis spectrophotometry to determine the remaining organic dye concentration based on the change in absorbance.

Additionally, a parameter study was also conducted to locate the optimum cellulose loading, synthesis temperature and operating condition for the composite material with the following arrangement: cellulose loading (1 wt%, 5 wt%, 10 wt%, 20 wt%, 30 wt%), hydrothermal synthesis temperature (100 °C, 120 °C, 140 °C, 160 °C, 180 °C), catalyst loading (0 g/L, 0.25 g/L, 0.50 g/L, 0.75 g/L, 1.00 g/L, 1.25 g/L), oxidant type (1 mM potassium peroxymonosulfate, 1 mM potassium persulfate, 1mM hydrogen peroxide), oxidant dosage (0 mM, 0.2 mM, 0.4 mM, 0.6 mM, 0.8 mM, 1.0 mM, 1.2 mM), and solution pH (pH 2, pH 4, pH 6, pH 8, pH 10).

3.5 Liquid Sample Analysis

The liquid samples were withdrawn and centrifuged to separate the composite material from the dye-infested water. Subsequently, a model 6320D UV-Vis spectrophotometer supplied by Jenway was used to determine the amount of organic dye that had been degraded based on the maximum absorption wavelength of methyl orange at 505 nm to determine the methyl orange concentration for each treated wastewater sample. The degradation efficiency of the organic dye was then determined using Equation 3.1. The chemical oxygen demand (COD) of the liquid samples were also analysed with the USEPA Reactor Digestion Method (Method 8000) where digestion vials containing the treated waste water were added with digestion reagents and put into a Hach DRB200 digestion reactor to be heated for 2 hours. The cooled liquid samples were then tested for their respective COD values via colorimetry.

$$\text{Degradation Efficiency} = \left| \frac{C - C_0}{C_0} \right| \times 100 \% \quad (3.1)$$

where

C = Final concentration of dye, mg/L

C_0 = Initial concentration of dye, mg/L

3.6 Characterisation of Cellulose, Titanium Dioxide and Composite Materials

The surface morphologies, accompanied by the presence of specific functional groups, thermal stability, particle sizes, surface area, and the optimum oxidation and reduction temperature of cellulose, titanium dioxide and the composite material will be examined with XRD, SEM-EDX and FTIR for an in-depth understanding of the properties of the stated materials.

3.6.1 X-Ray Diffraction (XRD)

The XRD analysis was used to determine the crystalline phases present within the composite material following by their relative amounts of both TiO₂ and α -cellulose. The analysis was one using the Shimadzu XRD-6000. Furthermore, the size of TiO₂ particles was estimated with the Debye-Scherrer equation. The XRD analysis of the composite material was based on the Cu-K α -X-ray with a wavelength of 1.5406 Å. The analysis range (2θ) of the XRD was from 10° to 70° with an increment angle of 0.1972°. The average crystallite sizes of the synthesized catalysts can be calculate using the Debye-Scherrer equation (equation 3.2).

$$D = \frac{K\lambda}{\beta \cos\theta} \quad (3.2)$$

where

K = Scherrer constant

D = Average crystallite size, μm

λ = X-ray wavelength, μm

β = Peak width at half maximum, rad

θ = Bragg diffraction angle, degree

3.6.2 Scanning Electron Microscopy with Energy Dispersive X-ray (SEM-EDX)

SEM-EDX was employed to examine the surface morphology of the composite material along with its chemical constituents via the Hitachi S-3400N model. The composite material was initially dried and attached onto a SEM holder attached via a double-sided carbon tape prior to the scanning. The scanning was done with magnifications of 5000 \times , 10 000 \times and 20 000 \times .

3.6.3 Fourier Transform Infrared Spectroscopy (FTIR)

The FTIR analysis was conducted using ThermoFisher Scientific Nicolet IS10 FTIR Spectrometer via the sampling procedure of the attenuated total reflectance (ATR). The FTIR scan was conducted with the resolution of 8 cm^{-1} with 254 scans with the range of 700 cm^{-1} to 4000 cm^{-1} .

CHAPTER 4

RESULTS AND DISCUSSION

4.1 Characterisation of Sonocatalysts

4.1.1 XRD

XRD was used to examine the crystal phases and average crystallite sizes of TiO₂, EFB cellulose, N-TiO₂, and also the N-TiO₂/Cellulose composite. Figure 4.1 shows the XRD spectra for TiO₂, N-TiO₂ and N-TiO₂/Cellulose composite.

Two major peaks at $2\theta = 21.90^\circ$ to 22.20° and at $2\theta = 15.70^\circ$ to 16.30° were observed, which corresponded to the (200) crystal plane and the (110) crystal plane of cellulose respectively (Poletto, Ornaghi Junior and Zattera, 2014). It could be observed that the synthesized EFB cellulose was amorphous due to the presence of broad peaks at the two mentioned positions within its XRD spectrum (Nazir, et al., 2013). The presence of a prominent peak at $2\theta = 21.90^\circ$ to 22.20° also indicated the successful elimination of lignin and the depolymerisation of hemicellulose yielding pure cellulose fibres. However, as compared to the standard XRD spectrum for commercial cellulose provided by Nazir, et al. (2013), the peaks of the extracted cellulose were comparatively broad with relatively less prominence. Such observations can be explained by the transformation of native cellulose into amorphous cellulose as shown in the work of Ciolacu, Ciolacu and Popa (2010), which may have been caused by the reduction in hydrogen bonding within the internal structure of cellulose. Such effects were also reported by them to be beneficial as majority of the surface chemical and physical reactions are prone to happen in the amorphous domain of cellulose. They stated that the transformation might have been due to the dissolution of cellulose in ethanol during the initial washing of residual oil.

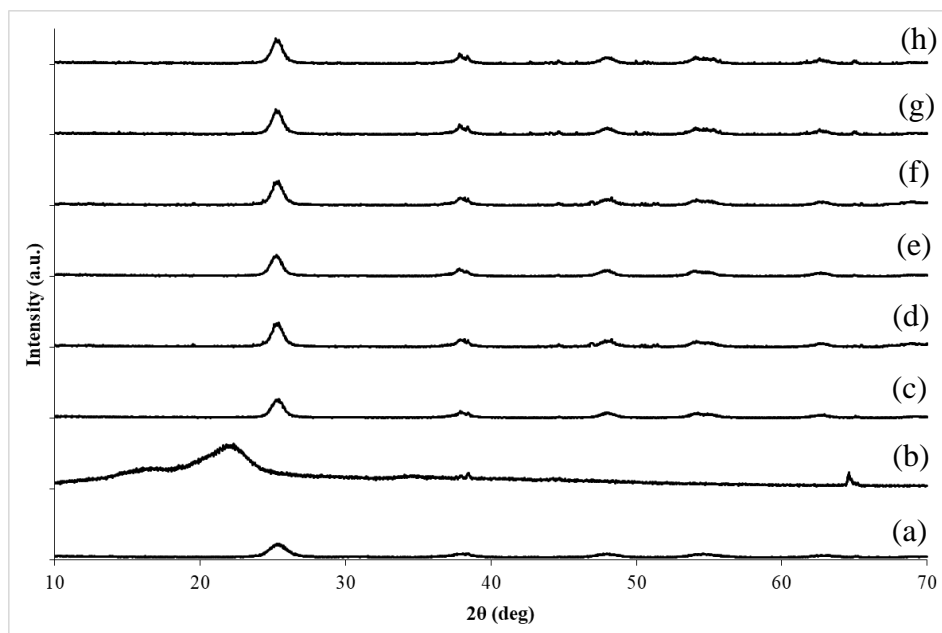


Figure 4.1: XRD Spectra of (a) TiO_2 , (b) Cellulose, (c) N- TiO_2 and N- TiO_2 /Cellulose Composite with the Cellulose Portion of (d) 1 wt%, (e) 5 wt%, (f) 10 wt%, (g) 20 wt% and (h) 30 wt%.

The synthesized TiO_2 was purely in the anatase phase due to the presence of diffraction peaks at $2\theta = 25.2^\circ$, 37.7° , 47.8° , 54.2° and 62.6° which corresponded to the (101), (004), (200), (105) and (204) crystallographic planes of anatase TiO_2 (Viana, Soares and Mohallem, 2010). Moreover, no diffraction peaks that were associated to the rutile phase of TiO_2 were observed at $2\theta = 27.3^\circ$, 35.9° , 41.1° and 56.4° . The absence of the rutile phase can be explained by the low hydrothermal synthesis temperature at 120°C as rutile is much more thermodynamically favourable at high temperatures due the requirement of bond breaking during the phase transfer from anatase to rutile (Hanaor and Sorrell, 2011). Typically, such phase transfer activities only occur at around 150°C to 600°C (Kalaivani and Anilkumar, 2017). Additionally, the broad peaks shown by the TiO_2 XRD spectrum suggested it has a low crystallinity. The loss of TiO_2 crystallinity is a common phenomenon especially when low synthesis temperatures are employed due to the collapse of meso-ordered structure and pore structure of TiO_2 as reported by Elgh, et al. (2014). Kalaivani and Anilkumar (2017) also reported that the decrease in synthesis temperature indeed leads to the decrement of TiO_2 crystallinity compensated by the reduction of crystallite size.

The doping of TiO₂ with triethylamine to produce N-TiO₂ produced a few miniscule but noticeable changes to its XRD spectrum. Firstly, there had been a slight shifting of the diffraction peak at $2\theta = 25.2^\circ$ which corresponded to the (101) crystal plane of anatase TiO₂ to the left. This shifting was also reported by Gomes, et al. (2019). As explained by Ata, et al. (2017), the shifting of the (101) diffraction peak was related to the slight change of binding energy due to the replacement of oxygen within the anatase TiO₂ lattice. Additionally, a slight transformation of the anatase phase to the rutile phase was observed by the addition of a small peak around $2\theta = 38^\circ$ to 39° which corresponds to the rutile TiO₂. However, no other diffraction peaks that are characteristic to the rutile phase was observed. The formation of the rutile phase at low temperatures could be explained by oxygen vacancies induced after doping with nitrogen (Nolan, et al., 2012). As a result, nitrogen doping extends the temperature range for anatase to rutile transformation hence causing the emergence of rutile TiO₂ at low temperatures. However, the effect of nitrogen doping to the formation of rutile TiO₂ is stated to be much more drastic at exceedingly high temperatures, thus explaining the miniscule amount of rutile TiO₂ being formed.

A slight improvement on the crystallinity of N-TiO₂ was observed as compared to TiO₂. However, there is no prominent nor distinct changes of XRD spectra after the doping with nitrogen in overall. Cong, et al. (2007) reported that the doping of nitrogen with triethylamine at molar ratio of titanium isopropoxide to triethylamine of 2 only had very minor effects structurally as the addition of nitrogen into the TiO₂ lattice did no change the crystal cell dimension by a huge degree. Lastly, no nitrogen diffraction peaks were observed in the XRD spectrum of N-TiO₂. This is also a common phenomenon as reported by Gomes, et al. (2019).

When the amount of cellulose constituted 1 wt%, there was a slight improvement of crystallinity as shown by the growth in diffraction peak intensity when compared to pure N-TiO₂. However, the improvements were not drastic. As the loading of cellulose increase, no prominent changes in peak intensity were observed in any way. As reported by Oliveira, et al. (2017), the impregnation of TiO₂ onto cellulose fibres in fact did not cause any alteration to the degree of crystallinity of TiO₂ and there are hardly any changes to crystallite sizes either. Additionally, they also reported that XRD itself cannot

detect any peaks that corresponded to cellulose due to the complete coverage of TiO_2 particles on the cellulose fibres.

Figure 4.2 shows the XRD spectra for N- TiO_2 / 5 wt% Cellulose composite synthesized under different hydrothermal temperatures. It can be observed that the increase in synthesis temperature consequent in the improvement of N- TiO_2 /Cellulose composite crystallinity. This was supported by the fact that the increase of synthesis temperature did led to a better crystallinity due to the increased stability of meso-sized structures and pores (Elgh, et al., 2014; Kalaivani and Anilkumar, 2017). However, the improvements were again hugely marginal with no actual prominent change. This was further confirmed by the work conducted by Suwannaruang, et al. (2015) which showed that hydrothermal temperature and time between 120 °C to 180 °C and 6 hours to 12 hours had no solid effect on anatase TiO_2 crystallinity and particle size. Additionally, cellulose would have underwent dissolution due to the hydrothermal solution itself containing ethanol and triethylamine (Mohamad, et al., 2015). As a result, composites with a high degree of crystallinity can hardly form under these circumstances.

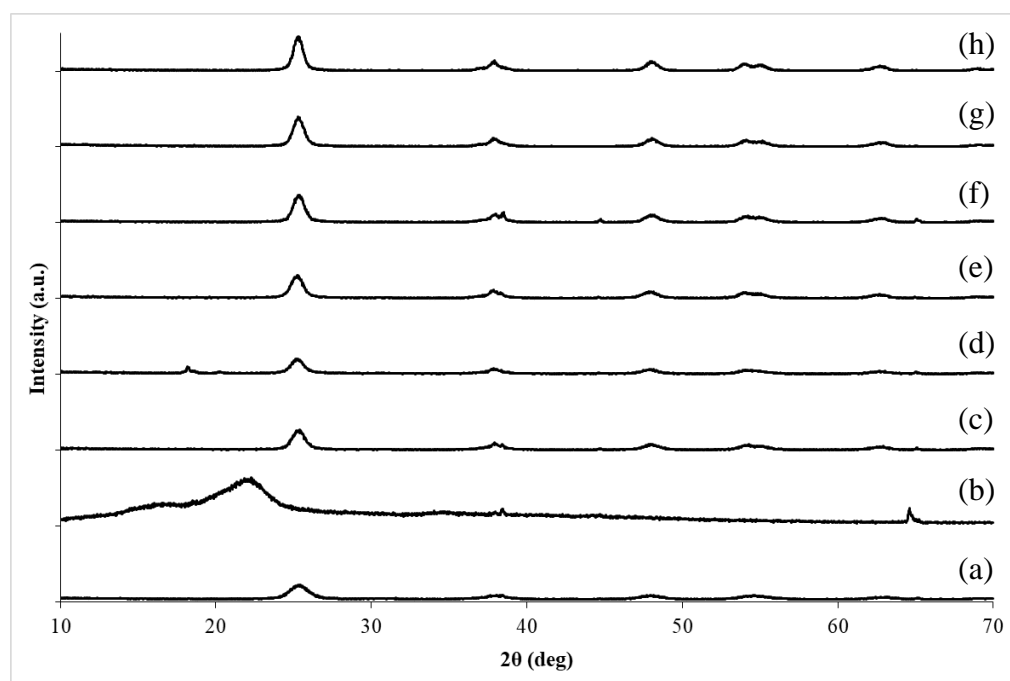


Figure 4.2: XRD Spectra of (a) TiO_2 , (b) Cellulose, (c) N- TiO_2 and N- TiO_2 / 5 wt% Cellulose Composite Synthesized at (d) 100 °C, (e) 120 °C, (f) 140 °C, (g) 160 °C and (h) 180 °C.

Out of the norm, N-TiO₂/Cellulose composite with 1 wt% cellulose loading exhibited a small peak at around $2\theta = 19.8^\circ$ to 21.3° while the stated peak was nonexistent in composites of any other cellulose loading. Mohamad, et al. (2015) stated that the peak could be possibly associated with cellulose II. However, the reason provided by them behind the transformation from native cellulose to cellulose II was due to the addition of NaOH and urea during the synthesis process, in which both were absent in the current case. A probable explanation for this phenomenon was that such transformations could be induced by hydroxypropyltriethylamine as shown in the work of Cao, et al. (2018). The source of hydroxypropyltriethylamine might have been originated from the hydrothermal solution itself which was constituted by triethylamine, titanium isopropoxide, water and ethanol. However, such transformation was negligible as it had hardly any effect at higher cellulose loading. Despite the increase of hydrothermal temperature, the formation of rutile TiO₂ was observed to be rather stagnant as excluding the sole rutile diffraction peak obtained from the synthesis of pure N-TiO₂, there were no other rutile associated peaks regardless of the variation in cellulose loading and synthesis temperature. Additionally, the decrement in crystallinity when the hydrothermal temperature used was 100 °C could be explained by the lack of hydrolysis of titanium isopropoxide, leading to amorphous N-TiO₂ formation at low temperatures (Yu, et al., 2007). They also mentioned that hydrolysis rates could be improved when hydrothermal synthesis temperatures used were higher than 100 °C.

The average crystallite size of TiO₂, N-TiO₂, and N-TiO₂/Cellulose composites at various cellulose loading and synthesis temperature were calculated using the Debye-Scherrer equation (equation 3.2) and presented in Table 4.1. It was found that both nitrogen doping and increased cellulose loading provided a marginal increment in crystallite size. The increase in synthesis temperature had much more effect on the increment of crystallite size TiO₂. These results are coherent with the facts stated previously that cellulose loading hardly gives any solid structural changes as opposed to the change in hydrothermal synthesis temperature.

Table 4.1: Average Crystallite Size of TiO₂, N-TiO₂, and N-TiO₂ Composites with Varying Cellulose Loading and Synthesis Temperature.

Sample	Average Crystallite Size (nm)
TiO ₂ (120 °C)	8.58
N-TiO ₂ (120 °C)	8.63
N-TiO ₂ /Cellulose (Cellulose 1 wt%, 120 °C)	8.58
N-TiO ₂ /Cellulose (Cellulose 5 wt%, 120 °C)	8.26
N-TiO ₂ /Cellulose (Cellulose 10 wt%, 120 °C)	8.58
N-TiO ₂ /Cellulose (Cellulose 20 wt%, 120 °C)	8.72
N-TiO ₂ /Cellulose (Cellulose 30 wt%, 120 °C)	8.83
N-TiO ₂ /Cellulose (Cellulose 5 wt%, 100 °C)	8.11
N-TiO ₂ /Cellulose (Cellulose 5 wt%, 140 °C)	9.02
N-TiO ₂ /Cellulose (Cellulose 5 wt%, 160 °C)	9.28
N-TiO ₂ /Cellulose (Cellulose 5 wt%, 180 °C)	10.60

4.1.2 SEM-EDX

SEM-EDX was employed to examine the surface morphology of TiO₂, N-TiO₂, cellulose, and N-TiO₂/Cellulose composites with varying cellulose loading and synthesised under different temperatures. Figure 4.3 shows the SEM images of extracted EFB cellulose. It could be observed that the extracted cellulose fibre had a rather smooth surface embedded with scar-like crevices and pores with irregular dimensions as shown in Figure 4.3 (a) and (b). Additionally, there were no signs of the deposition of any amorphous components on the surface of the extracted cellulose. As per Nazir, et al. (2013), the presence of these characteristics indicated the complete removal of high amorphous hemicellulose and lignin that were entangling the cellulose fibre, and also wax which were previously removed by submerging the EFB into ethanol. Additionally, they also mentioned that the emergence of scar like crevices and pores was due to the removal of embedded inorganic components on the surface of the fibre. Hence, the SEM images proved the complete elimination of unwanted substances, producing only cellulose fibres with the diameter of around 900 µm. The sizes of the produced crevices were largely uneven, but had a typical longitudinal size distribution of 100 µm to 1200 µm as shown in

Figure 4.3 (d), while pore like scars shown in Figure 4.3 (e) had an average diameter of 120 μm .

Figure 4.4 provides a side-by-side comparison of the surface morphology of pristine TiO_2 and N- TiO_2 . It can be seen from Figure 4.4 (a) that TiO_2 had an uneven distribution of roughly spherical congregates with majority of them being smaller than 10 μm , while for the large ones, around 20 μm . The formation of these TiO_2 congregates with rough surfaces instead of highly spherical particles with exceedingly smooth surfaces typically occur at low hydrothermal temperatures coupled with short synthesis time (Guo, et al., 2012). For the case of N- TiO_2 , it can be seen that chunkier particles with crystallite sizes around 8 μm to 70 μm were formed as compared to TiO_2 . Such effects were also reported by Barkul, et al. (2016) who further stated that nitrogen doping could have a significant effect on particle size especially when the nitrogen composition exceeds 7 mol%. Additionally, Barkul, et al. (2016) also stated that the doping of nitrogen enhances the crystallinity of TiO_2 which is also in consensus with the XRD spectrum of N- TiO_2 shown in Figure 4.1 and 4.2. However, a contradicting observation was obtained from Hu, et al. (2011) in which they found that the doping of nitrogen with triethylamine decreased both crystallite size and crystallinity, as opposed to Barkul, et al. (2016) and the current observations. In a N- TiO_2 review produced by Gomes, et al. (2019), they reported similar contradictions and stated that there were currently no agreement on how nitrogen doping affects the surface morphology and structure of TiO_2 .

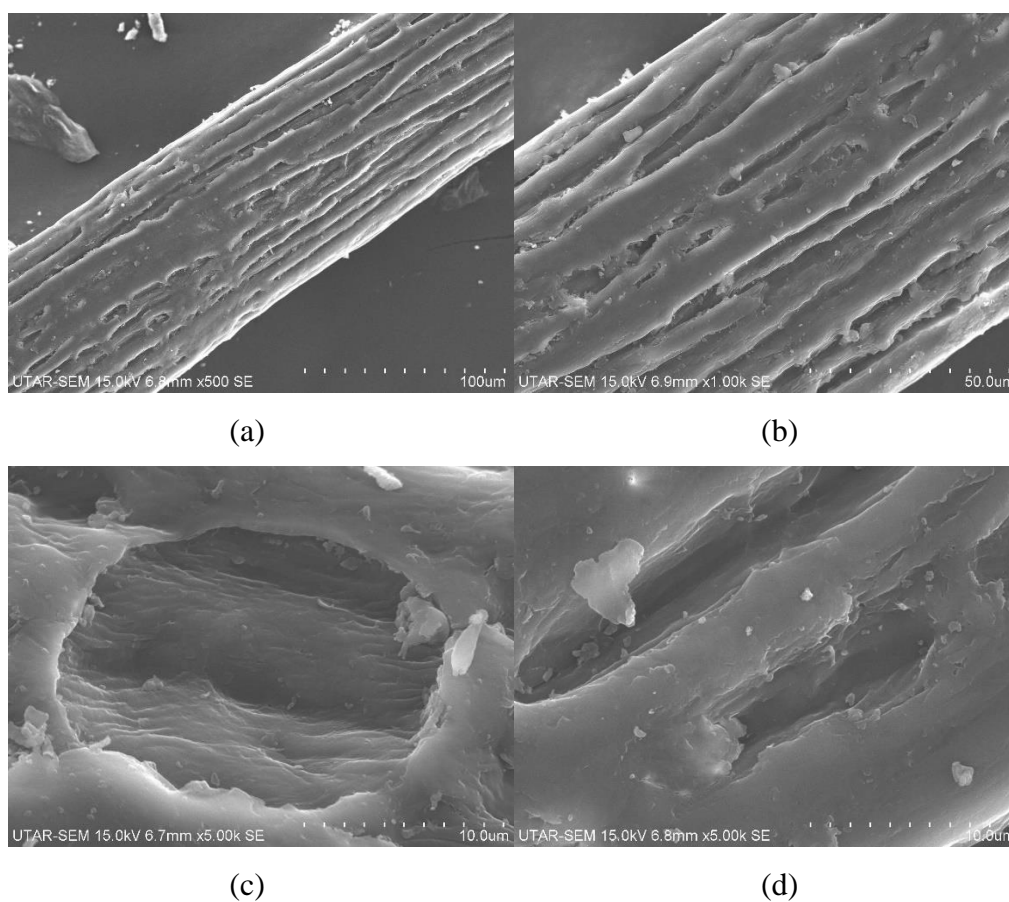


Figure 4.3: SEM Images of Extracted EFB Cellulose at Magnifications of (a) 500 \times , (b) 1000 \times , (c) 5000 \times and (d) 5000 \times .

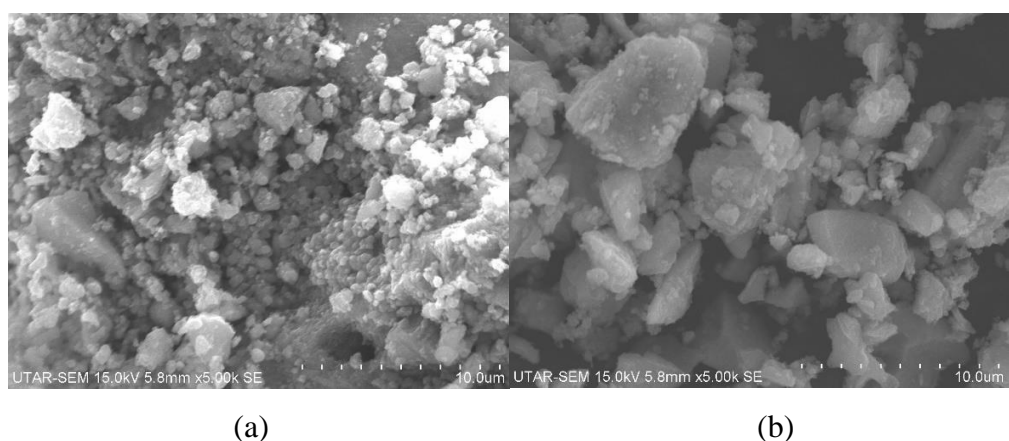


Figure 4.4: SEM Images of (a) TiO₂ and (b) N-TiO₂ at 5000 \times Magnification.

Figure 4.5 shows N-TiO₂ deposited on cellulose fibres at different cellulose loadings. Cellulose loadings had virtually no effect on N-TiO₂ particle size. These observations were in coherent with the results of XRD shown in Table 4.1. It could be observed that at extremely low cellulose loading, N-TiO₂

seemed to have fully covered the surface of cellulose by a thin N-TiO₂ layer, along with the deposition of aggregates and agglomerates causing the surface to be relatively rough. This observation was also found by Uddin, et al. (2007) with the exception that the N-TiO₂ layered surface was rather smooth with less signs of aggregates. The increase in aggregate formation might have been due to a far greater amount of titanium isopropoxide and a far lesser amount of cellulose used during the synthesis process. Subsequently, as cellulose loading was increased, it was found that the N-TiO₂ no longer fully covered the cellulose fibres with occasional cracks and holes present all throughout the fibre surface. The formation of aggregates were also found to be much more profound at higher cellulose loadings. The dispersal of these aggregates was also found to be increasingly loose at increasing cellulose loading. Such observations were also shown in the work of Oliveira, et al. (2017). The lack of crystallographic changes regardless of any cellulose loading were also reported by Oliveira, et al. (2017), which is in consensus with the current observations.

Figure 4.6 shows that the N-TiO₂ aggregates that were deposited on the surface of cellulose fibres increased in size at increasing hydrothermal temperatures. This overall effect was also reported by the XRD analysis as per Table 4.1. Such effects were due to the increase of N-TiO₂ crystallinity due to the increase of titanium isopropoxide hydrolysis as per Yu, et al. (2007). They also stated that low rates of titanium isopropoxide hydrolysis could cause residual un-hydrolysed titanium isopropoxide to inhibit the phase transfer from amorphous N-TiO₂ to its anatase phase and such problems conventionally happen at low hydrothermal temperatures.

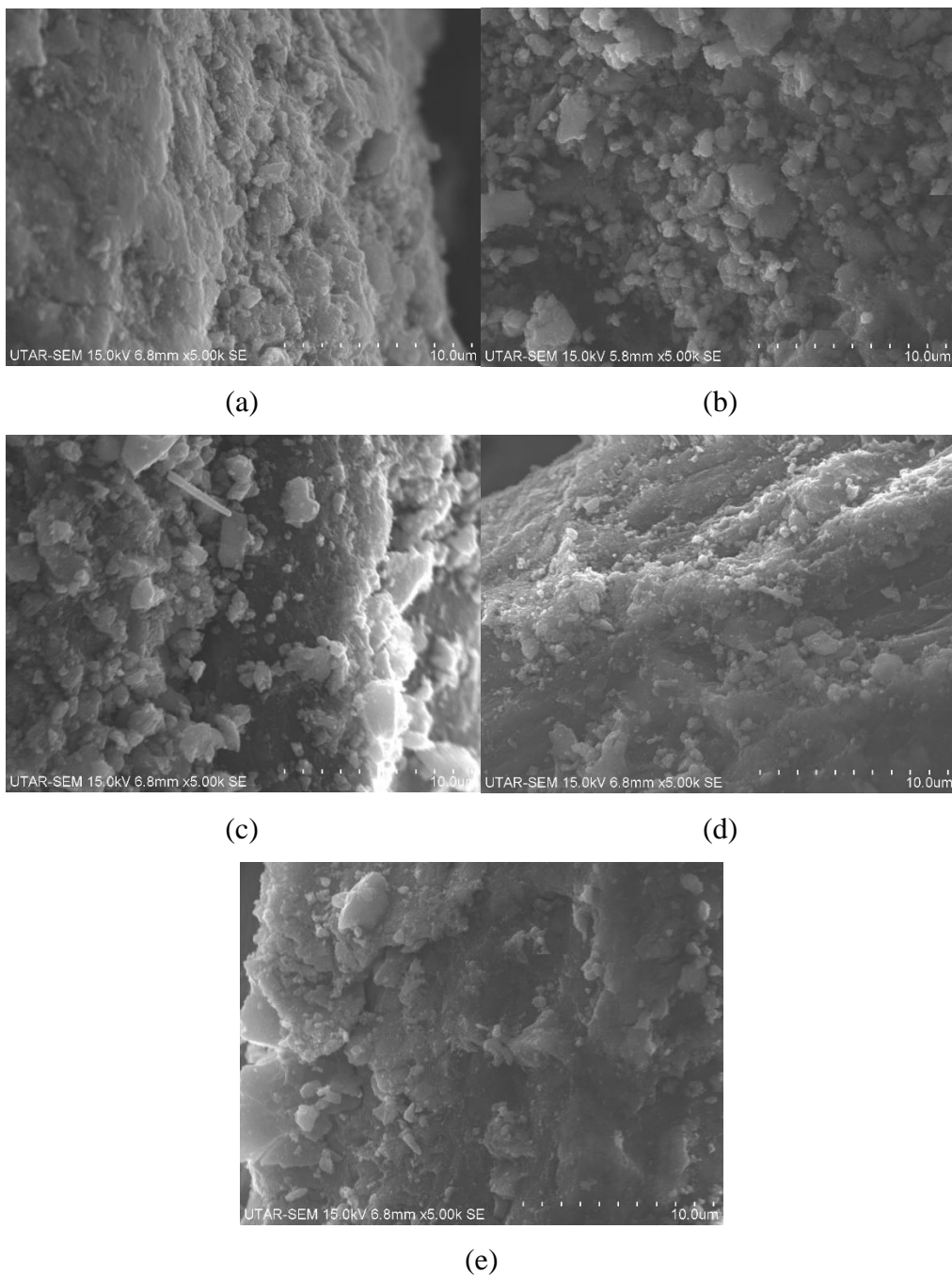


Figure 4.5: SEM Images of N-TiO₂/Cellulose Composites with Cellulose Loading of (a) 1 wt%, (b) 5 wt%, (c) 10 wt%, (d) 20 wt% and (e) 30 wt% at 5000× Magnification.

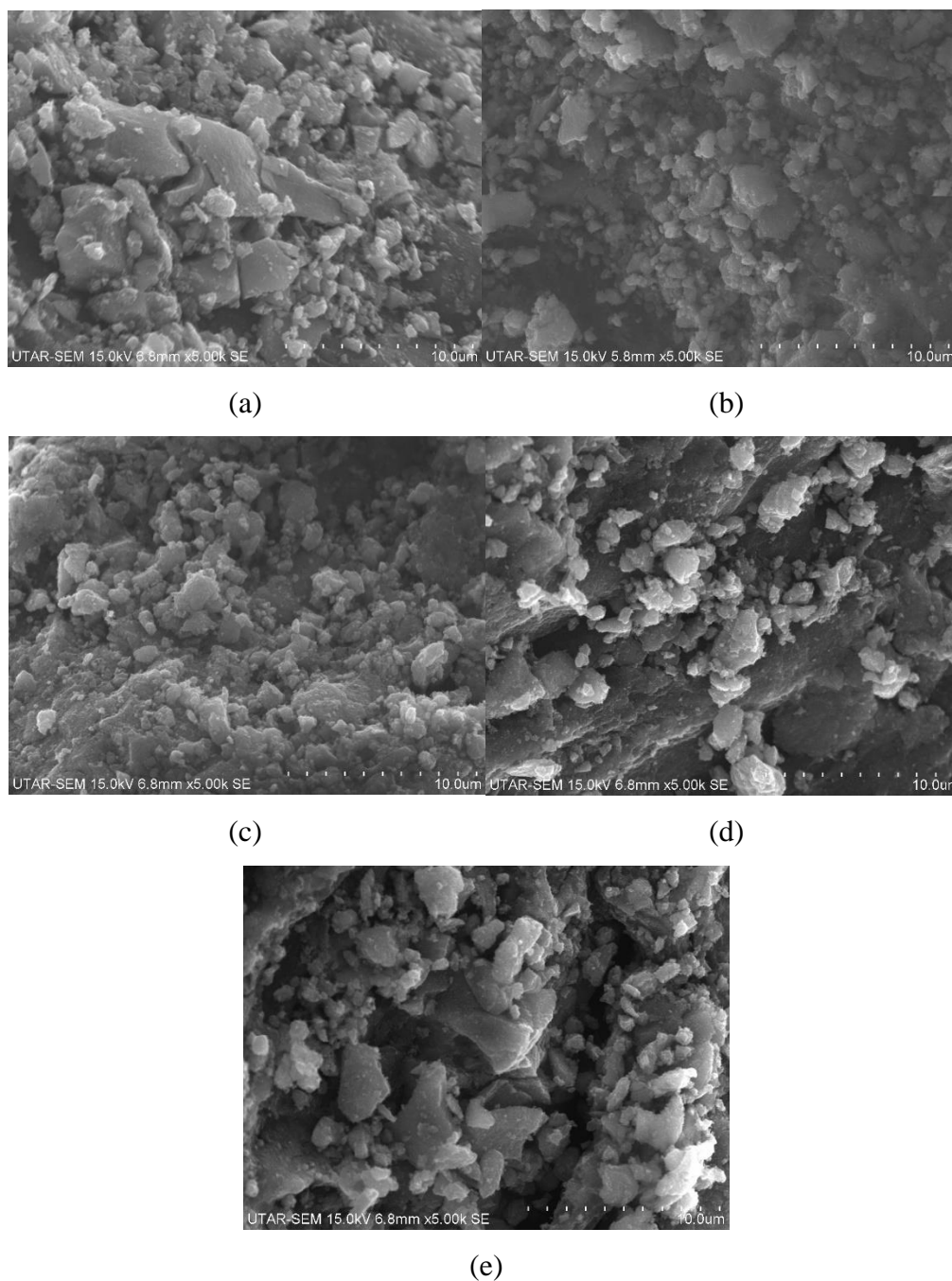


Figure 4.6: SEM Images of N-TiO₂/ 5 wt% Cellulose Composites Synthesized at (a) 100 °C, (b) 120 °C, (c) 140 °C, (d) 160 °C and (e) 180 °C at 5000× Magnification.

Table 4.2 shows the distribution of elements on the synthesised catalysts given by EDX analysis. It can be seen that sodium is present within the cellulose matrix in addition to the expected carbon and oxygen components. The presence of sodium can be traced back to the dissolution of EFB fibres into NaOH during the cellulose extraction process. This is due to a process which is

known as the mercerisation process, in which NaOH or other alkali penetrates into the amorphous cellular matrix thus increasing fibre flexibility, and subsequently enters into the crystalline regions of cellulose forming sodium-cellulose complexes (Budtova and Navard, 2016). Additionally, it could be seen that the increase in cellulose loading led to the increase of carbon and oxygen content within the N-TiO₂/cellulose composite. This indicated that cellulose had indeed properly incorporated into the composite itself. No drastic change in carbon, oxygen nor titanium weight composition was identified regardless of hydrothermal synthesis temperature. However, no nitrogen was found in any samples that were previously doped with triethylamine. Such phenomena was also shown in the EDX analysis of hydrothermally synthesized N-TiO₂ by Pookmanee, et al. (2018). This may be due to the scarce amount of oxygen being substituted by nitrogen within the lattice of TiO₂ itself (Gomes, et al., 2019).

Table 4.2: EDX Results for Various Catalysts.

Sample	C	O	Ti	N	Na
	(wt%)	(wt%)	(wt%)	(wt%)	(wt%)
TiO₂ (120 °C)	-	36.78	63.22	-	-
Cellulose	53.30	43.88	-	-	2.83
N-TiO₂ (120 °C)	-	40.37	59.63	-	-
N-TiO₂/Cellulose	19.99	40.97	39.05	-	-
(Cellulose 1 wt%, 120 °C)					
N-TiO₂/Cellulose	6.34	32.12	61.54	-	-
(Cellulose 5 wt%, 120 °C)					
N-TiO₂/Cellulose	12.93	40.44	46.63	-	-
(Cellulose 10 wt%, 120 °C)					
N-TiO₂/Cellulose	31.98	42.57	25.45	-	-
(Cellulose 20 wt%, 120 °C)					
N-TiO₂/Cellulose	54.19	43.56	2.25	-	-
(Cellulose 30 wt%, 120 °C)					
N-TiO₂/Cellulose	17.22	42.50	40.28	-	-
(Cellulose 5 wt%, 100 °C)					

Table 4.2 (Continued)

N-TiO₂/Cellulose (Cellulose 5 wt%, 140 °C)	19.99	40.97	25.45	-	-
N-TiO₂/Cellulose (Cellulose 5 wt%, 160 °C)	16.92	40.53	42.55	-	-
N-TiO₂/Cellulose (Cellulose 5 wt%, 180 °C)	15.33	41.52	43.15	-	-

4.1.3 FTIR

FTIR was used to study the functional groups that are present on the surfaces of the synthesized catalyst and cellulose. It could be seen that broad stretches were present at around 3400 cm^{-1} and 2906 cm^{-1} in the FTIR spectrum of cellulose which indicated the presence of -OH and C-H groups in cellulose (Nazir, et al., 2013). Additionally, a few minor peaks that corresponded to the bending vibration of -CH_2 , C-H and C-O groups on the cellulose fibre surface were also identified at 1432 cm^{-1} , 1375 cm^{-1} and 1326 cm^{-1} respectively as reported by Nazir, et al. (2013). The absence of peaks at 1735 cm^{-1} and 1248 cm^{-1} indicated that C=O group in hemicellulose and C-O-C present in lignin had been completely removed (Alemdar and Sain, 2008). Other peaks that were found at 1161 cm^{-1} , 1137 cm^{-1} , 1105 cm^{-1} and 895 cm^{-1} were also characteristic to cellulose. The mentioned first three peaks were associated to the C-O-C group of pyranose sugar and C-H rocking vibration, and the fourth peak indicated the presence of β -1,4-glycosidic bond that binds cellulosic units together (Nazir, et al., 2013; Kargarzadeh, et al., 2012).

Figure 4.7 (a) shows the FTIR spectra of TiO_2 . There was a broad peak at around 3400 cm^{-1} , which corresponded to the stretching vibration mode of O-H groups in TiO_2 (Leon, et al., 2017). Additionally, another prominent peak was located at around 1630 cm^{-1} , which could be associated to the O-H group vibration. A miniscule peak was identified at around 3840 cm^{-1} could be corresponded to the $\text{Ti}^{3+}\text{-OH}$ group in TiO_2 (Kumar, Badrinarayanan and Sastry, 2000). Another peak that was characteristic to the Ti-O-Ti group of TiO_2 was also identified at around 420 cm^{-1} (Viana, Soares and Mohallem, 2010). The broad band from 400 cm^{-1} to 900 cm^{-1} shown was also the characteristic of TiO_2 caused by the stretching vibration of Ti-O groups. Unfortunately, no nitrogen

associated peaks nor the shifting of TiO₂ peaks were identified in the FTIR spectrum of N-TiO₂. This might be due to the scarce amount of oxygen being substituted by nitrogen within the lattice of TiO₂ itself (Gomes, et al., 2019).

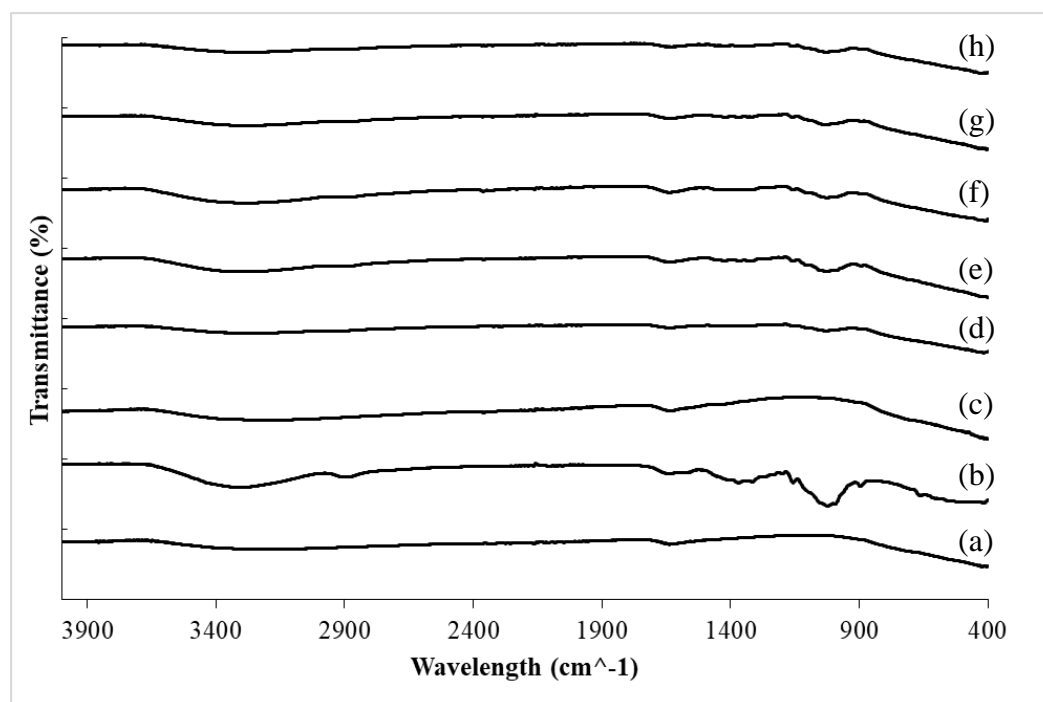


Figure 4.7: FTIR Spectra of (a) TiO₂, (b) Cellulose, (c) N-TiO₂ and N-TiO₂/Cellulose Composite with the Cellulose Portion of (d) 1 wt%, (e) 5 wt%, (f) 10 wt%, (g) 20 wt% and (h) 30 wt%.

For the composite materials, it could be seen that there was a clear incorporation of peaks into the spectrum of N-TiO₂ especially at 1105 cm⁻¹ and 895 cm⁻¹. The former peak was corresponded to the C-O-C group of pyranose sugar and C-H rocking vibration of cellulose, while the latter peak was corresponded to the cellulosic β -1,4-glycosidic bond (Nazir, et al., 2013; Kargarzadeh, et al., 2012). This indicated the successful deposition of N-TiO₂ onto the surface of cellulose fibres. The incorporation of the stated peaks were also being observed at higher hydrothermal temperatures as shown in Figure 4.8. However, the peak intensities exhibited by cellulosic components were found to diminish at increasing hydrothermal temperature. This suggested that the thermal decomposition of cellulose which is possible at high temperatures although such decompositions typically start as 250 °C as reported by Rantuch and Chrebet (2013).

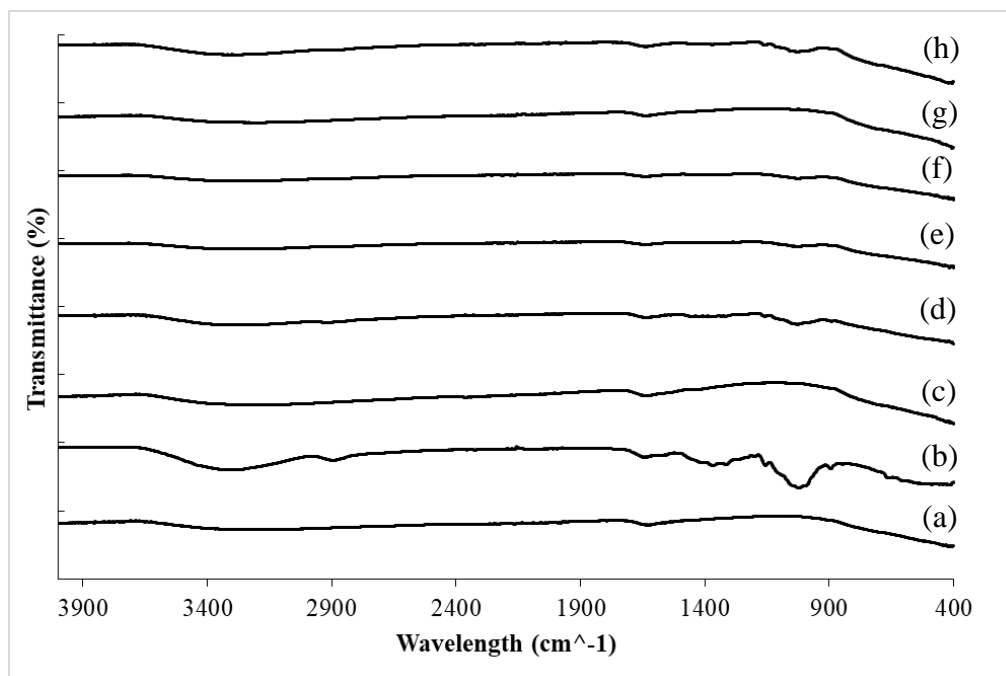


Figure 4.8: FTIR Spectra of (a) TiO₂, (b) Cellulose, (c) N-TiO₂ and N-TiO₂/ 5 wt% Cellulose Composite Synthesized at (d) 100 °C, (e) 120 °C, (f) 140 °C, (g) 160 °C and (h) 180 °C.

4.2 Parameter Studies

4.2.1 Effect of Different Cellulose Loading

Figure 4.9 and 4.10 show the sonocatalytic degradation efficiency of 20 ppm Congo red in the presence of TiO₂, cellulose, N-TiO₂ and N-TiO₂/Cellulose composites with different cellulose loadings. It was obvious that cellulose had the weakest sonocatalytic degradation efficiency, followed by pristine TiO₂, and then N-TiO₂/Cellulose composite with 30 wt% cellulose, N-TiO₂/Cellulose composite with 20 wt% cellulose, N-TiO₂/Cellulose composite with 10 wt% cellulose, N-TiO₂ and N-TiO₂/Cellulose composite with 1 wt% cellulose. The highest sonocatalytic activity was achieved by N-TiO₂/ 5 wt% Cellulose composite. It could be noticed that the drastic increase of cellulose content within the composite deteriorates its sonocatalytic degradation efficiency to an extent in which the composite material became inferior to pristine N-TiO₂. Despite such effects, the addition of around 1 wt% to 5 wt% of cellulose was found to boost the sonocatalytic degradation efficiency of N-TiO₂. Similar to the work conducted by Cong, et al. (2007), the doping of TiO₂ with

triethylamine in accordance to the titanium to nitrogen molar ratio of 2 reported a drastic improvement in terms of the photo catalytic degradation efficiency of the organic pollutants. The stated molar ratio is able to extend the photo-absorption of TiO_2 to the visible light region while decreasing photo-generated electron-hole pair recombination and band gap energy owing to the formation of N-Ti-O and Ti-O-N groups.

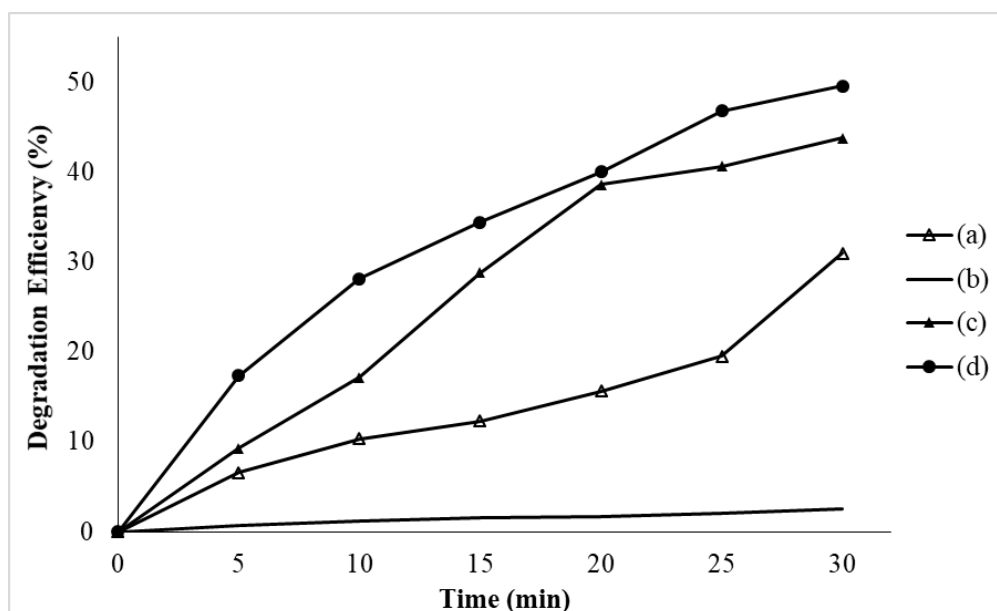


Figure 4.9: Sonocatalytic Degradation of 20 ppm Congo Red with 0.5 g/L of (a) TiO_2 , (b) cellulose, (c) N- TiO_2 , and (d) N- TiO_2 /Cellulose composite with Cellulose Loading of 5 wt%.

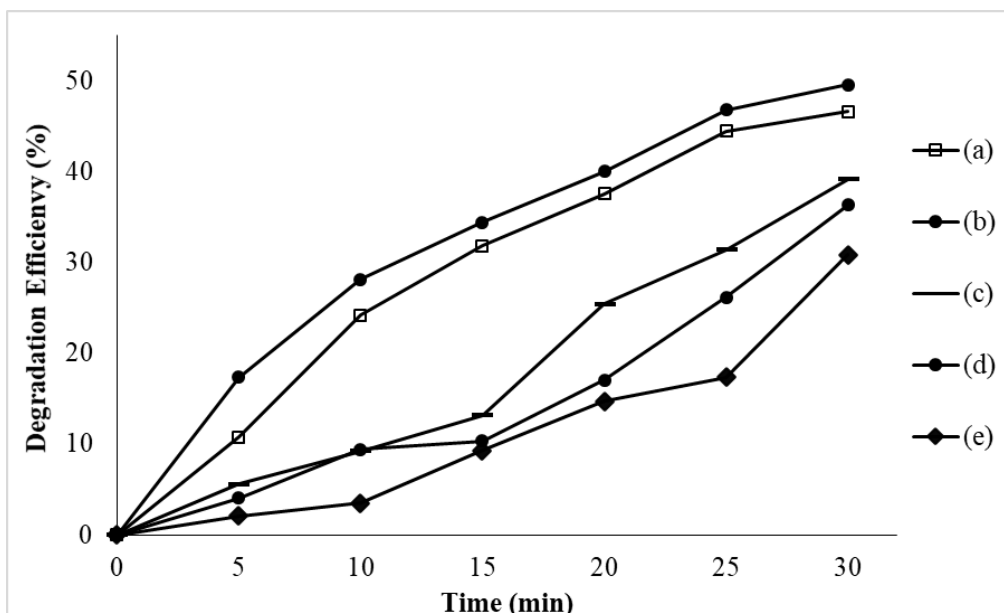


Figure 4.10: Sonocatalytic Degradation of 20 ppm Congo Red with 0.5 g/L of N-TiO₂/Cellulose composite with Cellulose Loading of (a) 1 wt%, (b) 5 wt%, (c) 10 wt%, (d) 20 wt% and (e) 30 wt%.

The addition of vast amounts of cellulose was found to be detrimental to the sonocatalytic degradation efficiency of Congo Red. This was due to the natural surface charge of cellulose itself being negative, hence greatly reducing its ability to adsorb Congo Red which itself is an anionic dye that also exhibits negative charge at its surface (Budd and Herrington, 1989; Mittal, Mittal, Malviya and Gupta, 2009). Additionally, alkaline pre-treatment and extraction processes were employed during the extraction of cellulose from EFB making the fibres itself alkaline by nature. Cellulose however can exhibit great Congo Red adsorption under acidic conditions (Namasivayam, Muniasamy, Rani and Ranganathan, 1996). However, a scarce amount of cellulose loading was beneficial as cellulose chains can react with titanium isopropoxide to narrow band gap energy and improve the development of more active surfaces thus leading to a greater sonocatalytic activity (Hamad, et al., 2018). The optimal amount of cellulose loading was found to be at 5 wt%.

4.2.2 Effect of Different Hydrothermal Synthesis Temperature

N-TiO₂/Cellulose composites with cellulose loading of 5 wt% were synthesized under different hydrothermal temperatures and employed for the sonocatalytic

degradation of 20 ppm Congo Red with catalyst loading of 0.5 g/L. The results are shown in Figure 4.11. It can be observed that the performance of N-TiO₂/Cellulose composite synthesized hydrothermally at 100 °C was rather subpar as compared to other composite materials. The maximum performance was obtained when the composite was synthesized at 120 °C, while further increase of hydrothermal temperature led to the deterioration of sonocatalytic degradation efficiency. However, a recovery of performance was seen when the synthesis temperature employed was 180 °C.

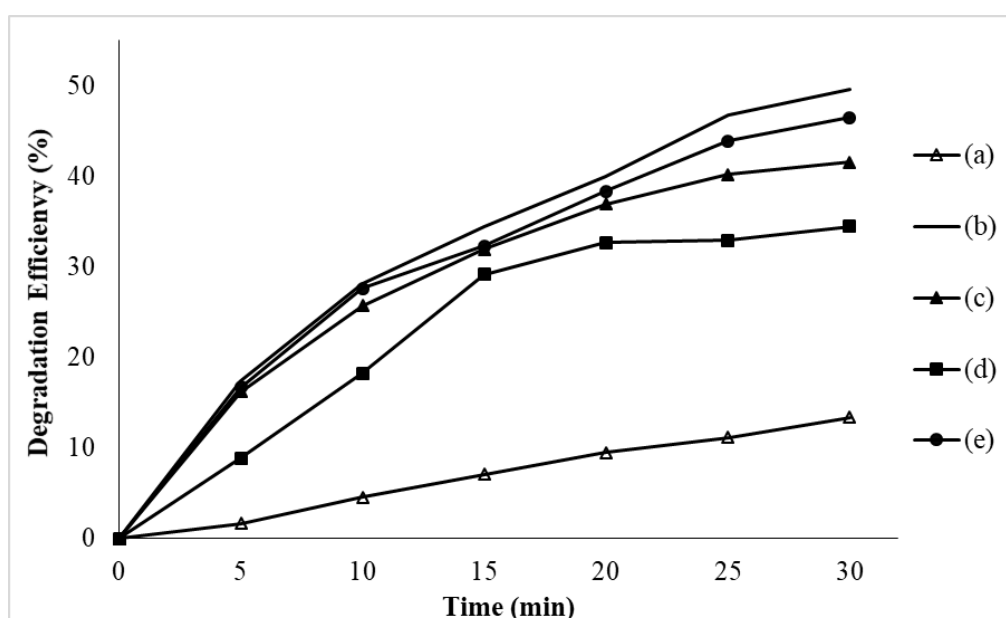


Figure 4.11: Sonocatalytic Degradation of 20 ppm Congo Red with 0.5 g/L of N-TiO₂/ 5 wt% Cellulose Composite Synthesized Hydrothermally at (a) 100 °C, (b) 120 °C, (c) 140 °C, (d) 160 °C and (e) 180 °C.

The inferiority of N-TiO₂/Cellulose composite synthesized hydrothermally at 100 °C as compared to other composites could be attributed to its low crystallinity as shown in its XRD spectrum in Figure 4.2 (d) as sonocatalytic processes were highly dependent crystallinity itself (Nandiyanto, Zaen and Oktiani, 2020). As mentioned previous, the drop in crystallinity was due to the incomplete hydrolysis of titanium isopropoxide which led to the formation of amorphous TiO₂ especially at 100 °C or lower (Yu, et al., 2007). The increase of hydrothermal temperature from 120 °C to 160 °C led to the drop in sonocatalytic degradation efficiency might have been due to the drastic

increase in crystallite size as shown in Table 4.1 which reduced the total active surface area for sonocatalysis to occur. However, a sudden recovery of sonocatalytic performance was seen when the composite material was synthesized at 180 °C. This might be attributed to the formation of more rutile phase TiO₂ as shown by the increase in rutile XRD diffraction peak intensity. The combination of both rutile and anatase TiO₂ was observed to be beneficial due to the transfer of photoelectrons from rutile TiO₂ to anatase TiO₂ which could improve charge separation (Wang, et al., 2016).

4.2.3 Effect of Different Catalyst Loading

Different loadings of N-TiO₂/Cellulose composite loading were used for the sonocatalytic degradation of 20 ppm Congo Red and the results are shown in Figure 4.12. It is axiomatic that increase in catalyst loading will increase the number of active sites available for sonocatalysis to occur. It could be observed from Figure 4.12 that at increasing catalyst loadings, the sonocatalytic degradation efficiency of Congo Red also increased until the optimum loading of 1 g/L. The further increase of catalyst loading was seen to cause a decrease in degradation efficiency as per the case of 1.25 g/L catalyst loading. Such detrimental effects could be explained by the agglomeration of the composite material which led to the sedimentation and decrement in particle size and specific surface area at high catalyst loadings (Mohamed, et al., 2012). Agglomeration of particles at high catalyst loading could consequent in the abrupt drop in catalytic activity as reported by Yunus, et al. (2016). Additionally, Mohamed, et al. (2012) also mentioned that high catalyst loading could also lead to light scattering and the decrease in irradiation pathways within the suspension due to increased turbidity and decreased opacity. The sonoluminescence generated by ultrasonic cavitation might also have been suffering similar scattering effects when the catalyst loading exceeds 1 g/L.

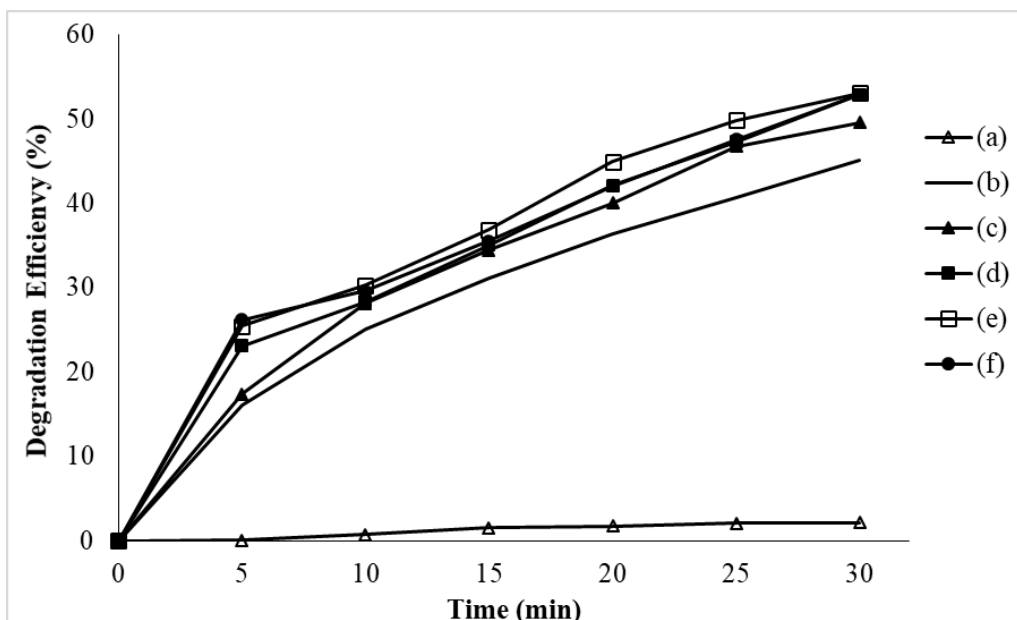


Figure 4.12: Sonocatalytic Degradation of 20 ppm Congo Red with different catalyst loading of (a) 0 g/L, (b) 0.25 g/L, (c) 0.5 g/L, (d) 0.75 g/L, (e) 1 g/L and (f) 1.25 g/L of N-TiO₂/ 5 wt% Cellulose Composite Synthesized Hydrothermally at 120 °C.

4.2.4 Effect of Different Oxidant

In this study, various types of oxidant with the concentration of 1 mM were added along with the N-TiO₂/Cellulose composite to degrade 20 ppm Congo Red. Figure 4.13 shows that the addition of potassium peroxydisulfate yielded the highest sonocatalytic degradation efficiency at around 90 % after 30 minutes degradation. The usage of 1 mM potassium persulfate only yielded around 64 % degradation efficiency, which was drastically lower as compared to potassium peroxydisulfate. Despite improvements on degradation efficiency were present during the usage of all oxidants, the utilization of H₂O₂ was found to only give marginal enhancement and was subpar as compared to the other two oxidants.

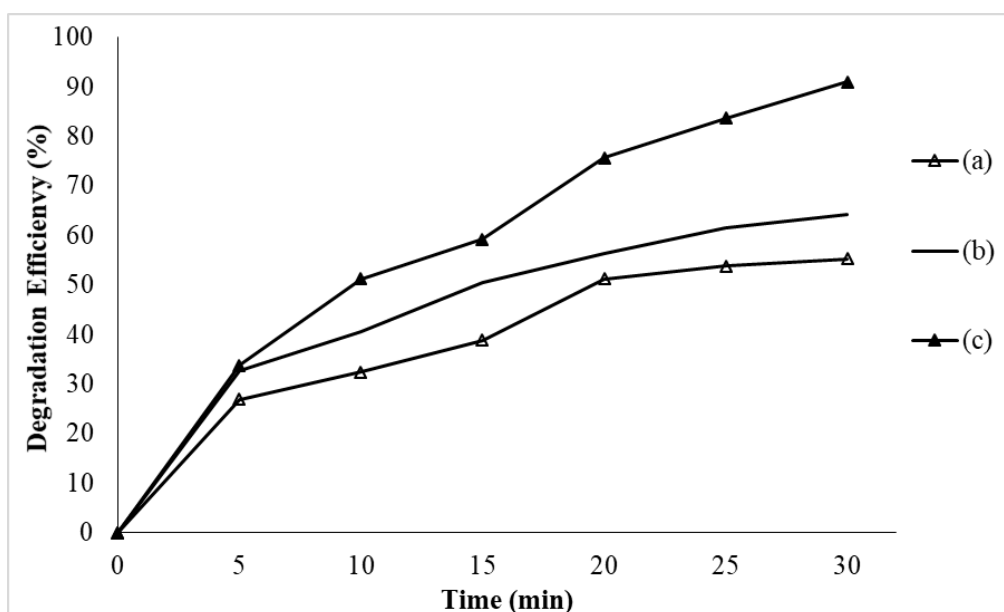


Figure 4.13: Sonocatalytic Degradation of 20 ppm Congo Red with N-TiO₂/ 5 wt % Cellulose Composite Synthesized Hydrothermally at 120 °C with the Addition of 1 mM (a) H₂O₂, (b) Potassium Persulfate and (c) Potassium Peroxymonosulfate.

The subpar performance of H₂O₂ could be attributed to the type of radicals generated upon its excitation. Litter (2005) reported that the breaking of O-O bonds in H₂O₂ could lead to the formation of hydroxyl radicals. However, hydroxyl radicals are often times ineffective against recalcitrant and refractory compounds like highly chlorinated organics and inorganics. The activation of H₂O₂ is also largely dependent on the wavelength of the absorbed photon which could be troublesome for case of sonoluminescence. Litter (2005) also mentioned that an awful radical recombination rates for H₂O₂ were identified which reduces the number of radicals available for the mineralization of organic compounds. However, H₂O₂ did offer some benefit to the alteration of surface functional groups on TiO₂ surfaces such as replacing -OH groups with -OOH groups, which extends the absorption region of the catalyst to the visible light region (Kang, et al., 2017).

Comparatively, the production of sulphate radicals resulted from the activation of both peroxyxymonosulfate and persulfate were reported to be much more effective in degrading recalcitrant compounds due to their relatively higher redox potential (Jo, et al., 2018). The production of sulfate radicals upon

peroxymonosulfate activation was relatively higher as compared to persulfate activation (Shi, 2015). Ahmadi, Ghanbari and Moradi (2015) also reported that the usage of peroxymonosulfate was relatively better as compared to persulfate in terms of photocatalytic degradation. Additionally, the usage of peroxymonosulfate could form a complex ligand on the surface of TiO_2 to which extends the activation absorption range of both peroxymonosulfate and TiO_2 to the visible range as reported by Jo, et al. (2018). Such phenomena was due to the excitation of peroxymonosulfate by visible light photon, causing the subsequent electron injection by the excited peroxymonosulfate into the conduction band of TiO_2 which further activates the peroxymonosulfate to form sulfate radicals.

4.2.5 Effect of Different Oxidant Dosage

Different concentrations of potassium peroxymonosulfate were employed with N- TiO_2 /Cellulose composite in degrading 20 ppm Congo Red to determine the optimum oxidant dosage. Figure 4.14 shows that the increase in oxidant dosing causes the sonocatalytic degradation efficiency to increase. However, the increments were seen to be less impactful as the oxidant dosage exceeded 1.0 mM. Jo, et al. (2018) reported that the diminishing of degradation efficiency enhancement when the concentration of peroxymonosulfate exceeds 1.0 mM was due to the competition between the organic pollutants and peroxymonosulfate itself in reacting with the produce sulfate radicals. It might be possible that at 1.0 mM peroxymonosulfate, the surface of the composite materials might have been fully saturated and complexed with all available peroxymonosulfate, hence producing the highest amount of sulfate radicals while reducing the competition for it (Jo, et al., 2018).

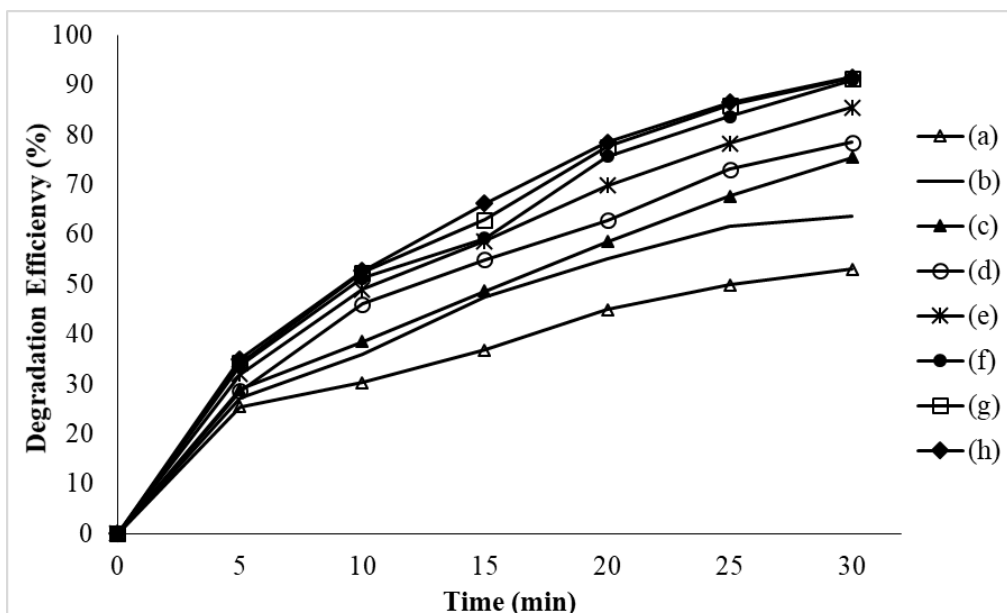


Figure 4.14: Sonocatalytic Degradation of 20 ppm Congo Red with N-TiO₂/ 5 wt% Cellulose Composite Synthesized Hydrothermally at 120 °C with the addition of (a) 0 mM, (b) 0.2 mM, (c) 0.4 mM, (d) 0.6 mM, (e) 0.8 mM, (f) 1.0 mM, (g) 1.2 mM and (h) 1.4 mM Potassium Peroxymonosulfate.

4.2.6 Effect of Different Solution pH

The effect of solution pH towards the sonocatalytic degradation efficiency was explored in this section. It can be seen from Figure 4.15 that N-TiO₂/Cellulose composite had better degradation efficiency at acidic conditions. Overall, N-TiO₂/Cellulose composite behaves terribly at alkaline conditions. This was resulted by the negatively charged surface of the composite materials at alkaline conditions, which decreased the rate of adsorption of Congo Red (Erdemoglu, et al., 2008). Additionally, Erdemoglu, et al. (2008) reported that the sulfonic groups from Congo Red only ionizes effectively at acidic to neutral conditions to yield a soluble anionic Congo Red anion that could be easily adsorbed onto the particle surface. There was a possibility of oxidation of soluble anionic Congo Red anion directly by oxygen if the anions were produced in the first place which was less possible under alkaline conditions.

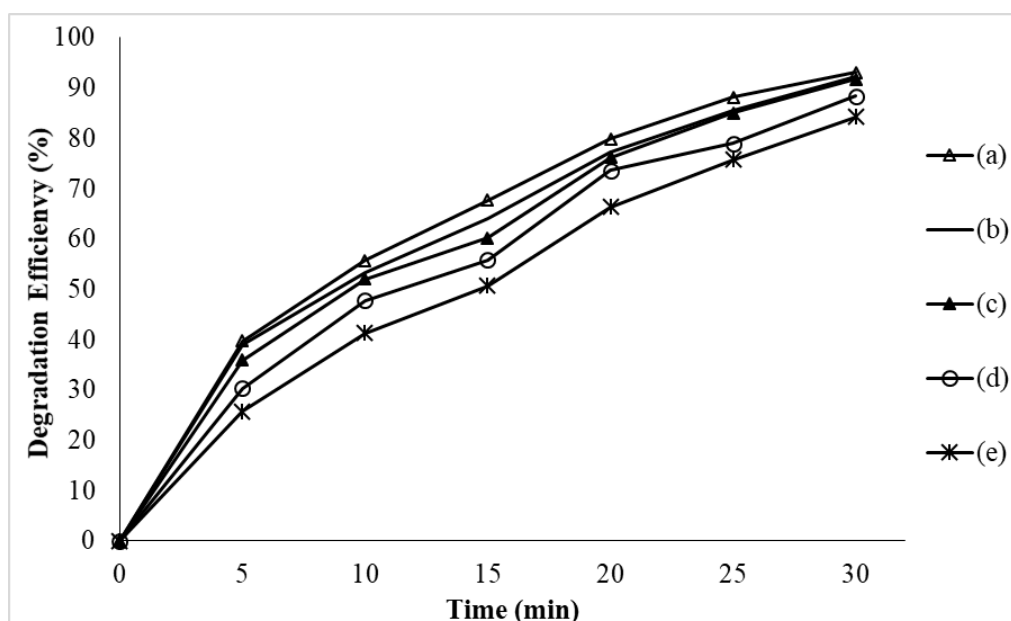


Figure 4.15: Sonocatalytic Degradation of 20 ppm Congo Red with N-TiO₂/ 5 wt% Cellulose Composite Synthesized Hydrothermally at 120 °C with 1.0 mM Potassium Peroxymonosulfate at Solution pH of (a) 2, (b) 4, (c) 6, (d) 8 and (e) 10.

4.3 COD Test Results

COD tests were conducted on the sonolysis and sonocatalytic degradation of 20 ppm Congo Red. The prescribed optimal conditions were obtained from the previous parameter study, such as cellulose loading = 5 wt%, hydrothermal synthesis temperature = 120 °C, catalyst loading = 1 g/L, oxidant type = potassium peroxydisulfate, oxidant dosage = 1.0 mM and solution pH = pH 6.

The COD test results showed that the addition of 5 wt% cellulose to N-TiO₂ could boost the degradation rate of Congo Red. These results were consistent with the parameter study on cellulose loading in section 4.2.1. There was a lack of COD test reference data in literature in the case of N-TiO₂/Cellulose composite usage. However, roughly similar works were performed by Kanakaraju and Wong (2008) in which they reported a COD removal efficiency of 64.92 % when using TiO₂/modified sago bark cellulose in the degradation of organic waste in wastewater after 120 min. In our case, 73.7 % of COD removal was obtained by using N-TiO₂/Cellulose composite thus proving the benefits of nitrogen doping via triethylamine.

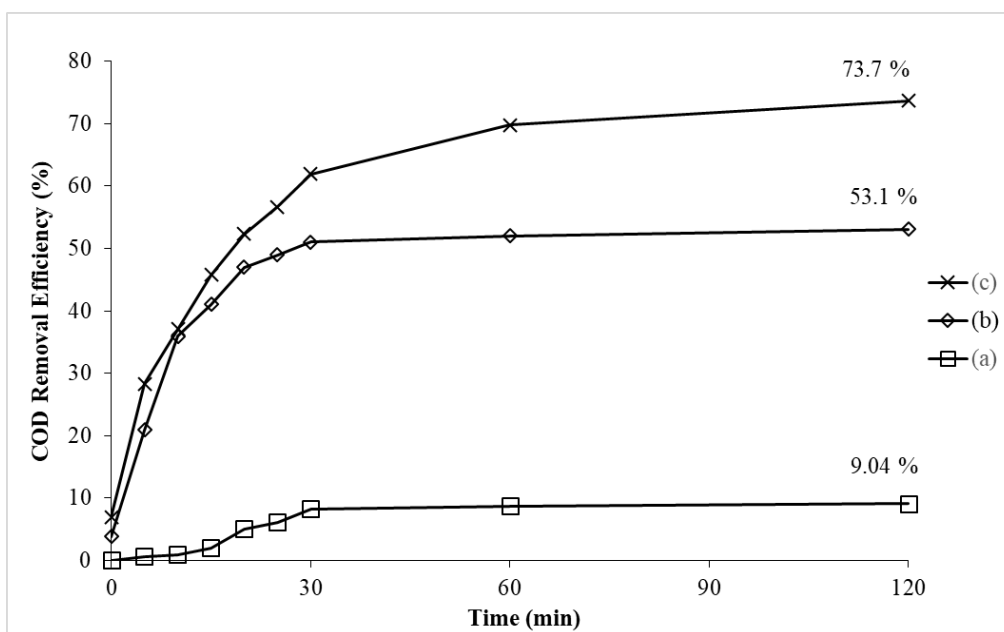


Figure 4.16: COD Results for (a) Sonolysis, Sonocatalytic Degradation of Congo Red in the Presence of (b) N-TiO₂ and (c) N-TiO₂/ 5 wt% Cellulose Composite under Optimum Conditions.

CHAPTER 5

CONCLUSIONS AND RECOMMENDATIONS

5.1 Conclusions

In this work, the synthesis of N-TiO₂/Cellulose was conducted via the hydrothermal synthesis route for sonocatalytic degradation of 20 ppm of Congo Red. The synthesized composite was also characterized using XRD, SEM-EDX and FTIR analyses. The XRD spectra of N-TiO₂/Cellulose identified the presence of anatase N-TiO₂ on the surface of the extracted EFB cellulose. Rutile N-TiO₂ was found to be extremely scarce especially at low hydrothermal synthesis temperature. The change in cellulose loading did not have any solid impact on the crystallographic properties of N-TiO₂. However, the increase in hydrothermal temperature was found to increase composite crystallinity. As per the SEM results, it was observed that an uneven layer of N-TiO₂ had partially covered the cellulose fibres with occasional cracks. Additionally, a large amounts of N-TiO₂ aggregates and agglomerates were present on the N-TiO₂ covered cellulose fibre surface. The EDX results also confirmed the successful deposition of N-TiO₂ onto the surface of cellulose fibres. However, nitrogen was not detected via EDX due to the scare amount of nitrogen within the TiO₂ lattice. FTIR results further showed the presence of O-H, Ti-O-Ti, Ti-O and Ti³⁺-OH groups on the cellulose fibres which again, proved the successful impregnation of TiO₂ onto cellulose fibre surface. Additionally, the presence of cellulose within the composite material was confirmed by the presence of C-O-C group of pyranose sugar, C-H rocking vibration and β-1,4-glycosidic bond.

Operating parameter studies for sonocatalytic degradation of 20 ppm Congo Red in the presence of N-TiO₂/Cellulose composite were also conducted. It was observed that only a scarce amount of cellulose loading (5 wt%) was beneficial to the sonocatalytic degradation of Congo Red due to the inferiority of Congo Red adsorption onto cellulose surface. Additionally, the optimal temperature for the hydrothermal synthesis of the composite was found to be 120 °C. Any temperature lower would cause the abrupt loss in catalytic activity due to the incomplete hydrolysis of titanium isopropoxide and the formation of amorphous TiO₂. The increment of hydrothermal synthesis temperature above

the optimal would lead to the drastic increase of crystallite sizes and particle sizes, which greatly reduced the specific surface area for sonocatalysis. Catalyst dosage of 1.0 g/L was found to be the best catalyst loading due to the availability of more active sites for the dye degradation to occur. However, further increase of catalyst loading would increase sonoluminescence scattering and particle agglomeration which in turn consequent in the drop in sonocatalytic activity. The usage of 1.0 mM of potassium peroxymonosulfate was found to be the optimal oxidant type and loading due to formation of large amounts of sulfate radicals for the degradation of Congo Red. The further increase of potassium peroxymonosulfate would cause the competition between peroxymonosulfate itself with Congo Red in reacting with the sulfate radicals hence decreasing degradation efficiency. N-TiO₂/Cellulose composite was found to work best at acidic conditions. Conclusively, 1.0 g/L of N-TiO₂/Cellulose with cellulose loading of 5 wt% synthesized hydrothermally at 120 °C along with the addition of 1.0 mM of potassium peroxymonosulfate under acidic conditions could achieve 91.74 % of 20 ppm Congo Red sonocatalytic degradation in 30 min and a COD removal of 73.7 %.

5.2 Recommendations for Future Work

Higher hydrothermal synthesis temperature should be used for the synthesis of N-TiO₂/Cellulose to induce the formation of more rutile phase N-TiO₂ and improve the crystallinity of the composite itself. The combination of anatase and rutile phase was stated to be much more beneficial for sonocatalytic degradation efficiency as compared to pure anatase phase. Additionally, instead of a one-pot hydrothermal synthesis of the composite, N-TiO₂ can be synthesized at much higher temperatures above that of the cellulose thermal degradation temperature, followed by the cold impregnation of the synthesized N-TiO₂ onto cellulose surface in order to better control the morphology of N-TiO₂ while ensuring the molecular integrity of cellulose.

REFERENCES

- Abdullah, N. and Sulaiman, F., 2013. The oil palm wastes in malaysia. In: M.D. Matovic, ed. *Biomass now: sustainable growth and use*. United Kingdom: InTechOpen. pp. 75-93.
- Adityosulindro, S., Barthe, L., Gonzalez-Labrada, K, Haza, U. J. J., Delmas, H. and Julcour, C., 2017. Sonolysis and sono-fenton oxidation for removal of ibuprofen in (waste)water. *Ultrasonics Sonochemistry*, 39(2017), pp. 889-896.
- Ahlstrom, L., Eskilsson, C. S. and Biorklund, E., 2005. Determination of banned azo dyes in consumer goods. *Trends in Analytical Chemistry*, 24(1), pp. 49-56.
- Ahmadi, M., Ghanbari, F. and Moradi, M., 2015. Photocatalysis assisted by peroxymonosulfate and persulfate for benzotriazole degradation: effect of pH on sulfate and hydroxyl radicals. *Water Science & Technology*, 72(11), pp. 2095-2102.
- Alemdar, A. and Sain, M., 2008. Isolation and characterization of nanofibers from agricultural residues – wheat straw and soy hulls. *Bioresource Technology*, 99(2008), pp. 1664-1671.
- Ambrogi, V., Carfagna, C. Cerruti, P. and Marturano, V., 2017. Additives in polymer. In: C. F. Jasso-Gastinel and J. M. Kenny, eds. *Modification of polymer properties*. Oxford, United Kingdom: Elsevier. pp. 87-108.
- Angelis, F. D., Valentin, C. D., Fantacci, S., Vittadini, A. and Selloni, A., 2014. Theoretical studies on anatase and less common TiO₂ phases: bulk, surfaces, and nanomaterials. *Chemical Reviews*, 114(2014), 9708-9753.
- Asl, S. D., Saed, A. E. and Sadrnezhad, S. K., 2019. Hierarchical rutile/anatase TiO₂ nanorod/nanoflower thin film: synthesis and characterizations. *Materials Science in Semiconductor Processing*, 93(2019), 252-259.
- Ata, R., Sacco, O., Vaiano, V., Rizzo, L., Tore, G. Y. and Sannino, D., 2017. Visible light active N-doped TiO₂ immobilized on polystyrene as efficient system for wastewater treatment. *Journal of Photochemistry and Photobiology A: Chemistry*, 348(2017), pp. 255-262.
- Awalludin, M. F., Sulaiman, O., Hashim, R. and Aidawati, W. N., 2015. An overview of the palm industry in Malaysia and its waste utilization through thermochemical conversion, specifically via liquefaction. *Renewable and Sustainable Energy Reviews*, 50(2015), pp. 1469-1484.
- Bao, Y., Kang, Q. L. and Ma, J. Z., 2018. Structural regulation of hollow spherical TiO₂ by varying titanium source amount and their thermal insulation property. *Colloids and Surfaces A*, 537(2018), pp. 69-75.

Barkul, R. P., Koli, V. B., Shewale, V. B., Patil, M. K. and Delekar, S. D., 2016. Visible active nanocrystalline N-doped anatase TiO₂ particles for photocatalytic mineralization studies. *Materials Chemistry and Physics*, 173(2016), pp. 42-51.

Bethi, B., Sonawane, S. H., Bhanvasem, B. A. and Gumfekar, S. P., 2016. Nanomaterials-based advance oxidation processes for wastewater treatment: A review. *Chemical Engineering and Processing*, 109(2016), pp. 178-189.

Bingham, S. and Daoud, W. A., 2010. Recent advances in making nano-sized TiO₂ visible-light active through rare-earth metal doping. *Journal of Materials Chemistry*, 21(2011), pp. 2041-2050.

Bora, L. V. and Mewada, R. K., 2017. Visible/solar light activated photocatalyst for organic effluent treatment: fundamentals, mechanisms and parametric review. *Renewable and Sustainable Energy Reviews*, 76(2017), pp. 1393-1421.

Brenner, M. P., Hilgenfeldt, S. and Lohse, D., 2002. Single-bubble sonoluminescence. *Reviews of Modern Physics*, 74(2), pp. 425-484.

Brown, R. M., 2003. Cellulose structure and biosynthesis: what is in store for the 21st Century? *Journal of Polymer Science*, 42(3), pp. 487-495.

Budd, J. and Herrington, T. M., 1989. Surface charge and surface area of cellulose fibres. *Colloids and Surfaces*, 36(1989), pp. 273-288.

Budtova, T. and Navard, P., 2016. Cellulose in NaOH-water based solvents: a review. *Cellulose*, 23(1), pp. 5-55.

Burnside, S. D., Shklover, V., Barbe, C., Comte, P., Arendse, F., Brooks, K. and Gratzel, M., 1998. Self-organization of TiO₂ nanoparticles in thin films. *Chemistry of Materials*, 10(1998), pp. 2419-2425.

Butun, S., Demirci, S., Yasar, A.O., Sagbas, S., Aktas, N. and Sahiner, N., 2017. 0D, 1D, 2D, and 3D soft and hard templates for catalysis. *Studies in Surface Science and Catalysis*, 177(2017), pp. 317-357.

Cao, L., Liang, T., Zhang, X., Liu, W., Li, J., Zhan, X. and Wang, L., 2018. In-situ pH-sensitive fibers via the anchoring of bromothymol blue on cellulose grafted with hydroxypropyltriethylamine groups via adsorption. *Polymers*, 10(7), pp. 709-722.

Cesaro, A. and Belgiono, V., 2013. Sonolysis and ozonation as pretreatment for anaerobic digestion of solid organic waste. *Ultrasonics Sonochemistry*, 20(3), pp. 931-936.

Chauhan, I. and Mohanty, P., 2014. Immobilization of titania nanoparticles on the surface of cellulose fibres by a facile single step hydrothermal method and study of their photocatalytic and antibacterial activities. *RSC Advances*, 4(2014), pp. 57885-57890.

Chio, C., Sain, M. and Qin, W., 2019. Lignin utilization: a review of lignin depolymerisation from various aspects. *Renewable and Sustainable Energy Reviews*, 107(2019), pp. 232-249.

Choo, Y. M., 2012. *Malaysia: economic transformation advances oil palm industry*. Retrieved from <https://www.aocs.org/stay-informed/inform-magazine/featured-articles/malaysia-economic-transformation-advances-oil-palm-industry-september-2012>

Ciolacu, D., Ciolacu, F. and Popa, V., 2010. Amorphous cellulose – structure and characterization. *Cellulose Chemistry and Technology*, 45(1), pp. 13-21.

Conesa, J. C., 2010. The relevance of dispersion interactions for the stability of oxide phases. *The Journal of Physical Chemistry C*, 114(2010), pp. 22718-22726.

Cong, Y., Zhang, J., Chen, F. and Anpo, M., 2007. Synthesis and characterization of nitrogen-doped TiO₂ nanophotocatalyst with high visible light activity. *Journal of Physical Chemistry C*, 111(2007), pp. 6976-6982.

Daghrir, R., Drogui, P. and Robert, D., 2013. Modified TiO₂ for environmental photocatalytic applications: a review. *Industrial & Engineering Chemistry Research*, 52(2013), pp. 3581-3599.

Deboni, T. L., Simioni, F. J., Brand, M. A. and Lopes, G. P., 2018. Evolution of the quality of forest biomass for energy generation in a cogeneration plant. *Renewable Energy*, 135(2019), pp. 1291-1302.

Diebold, U., 2002. The surface science of titanium dioxide. *Surface Science Reports*, 48(2003), pp. 53-229.

Djurisic, A. B., Leung, Y. H. and Ng, A. M. C., 2014. Strategies for improving the efficiency of semiconductor metal oxide photocatalyst. *Material Horizons*, 1(2014), pp. 400-410.

Dong, P., Cheng, X., Huang, Z., Chen, Y., Zhang, Y., Nie, X. and Zhang, X., 2018. In-situ and phase controllable synthesis of nanocrystalline TiO₂ on flexible cellulose fabrics via a simple hydrothermal method. *Materials Research Bulletin*, 97(2018), pp. 89-95.

Elgh, B., Yuan, N., Cho, H. S., Mageri, D., Philipp, M., Roth, S. V., Yoon, K. B., Muller-Buschbaum, P., Terasaki, O. and Palmqvist, A. E. C., 2014. Controlling morphology, mesoporosity, crystallinity, and photocatalytic activity of ordered mesoporous TiO₂ films prepared at low temperature. *APL Materials* 2, 113313(2014), pp. 1-13.

Erdemoglu, S., Aksu, S. K., Sayilkan, F., Izgi, B., Asilturk, M., Sayilkan, H., Frimmel, F. and Gucer, S., 2008. Photocatalytic degradation of Congo Red by hydrothermally synthesized nanocrystalline TiO₂ and identification of

degradation products by LC-MS. *Journal of Hazardous Materials*, 155(3), pp. 469-476.

Eren, Z. and Ince, N. H., 2010. Sonolytic and sonocatalytic degradation of azo dyes by low and high frequency ultrasound. *Journal of Hazardous Materials*, 177(2010), pp. 1019-1024.

Farhat, W., Venditti, R., Quick, A., Taha, M., Mignard, N., Becquart, F. and Ayoub, A., 2017. Hemicellulose extraction and characterization for applications in paper coatings and adhesives. *Industrial Crops & Products*, 107(2017), pp. 370-377.

Feng, S. H. and Li, G. H., 2017. Hydrothermal and solvothermal syntheses. In: R. Xu and Y. Xu, eds. *Modern inorganic synthetic chemistry*. Oxford, United Kingdom: Elsevier. pp. 73-104.

Flint, E. B. and Suslick, K. S., 1991. The temperature of cavitation. *Science*, 253(5026), pp. 1397-1399.

Food and Agriculture Organization of the United Nations, n.d. *AQUASTAT*. Retrieved from <http://www.fao.org/nr/water/aquastat/data/query/index.html?lang=en>

Forgacs, E., Cserhati, T. and Oros, G., 2004. Removal of synthetic dyes from wastewaters: a review. *Environmental International*, 30(2004), pp. 953-971.

Fujishima, A. and Honda, K., 1972. Electrochemical photolysis of water at a semiconductor electrode. *Nature*, 238(1972), pp. 37-38.

Fujishima, A., Rao, T. N. and Tryk, D. A., 2000. Titanium dioxide photocatalyst. *Journal of Photochemistry and Photobiology*, 1(2000), pp. 1-21.

Fujishima, A., Zhang, X. and Tryk, D. A., 2008. TiO₂ photocatalysis and related surface phenomena. *Surface Science Reports*, 63(2008), pp. 515-582.

Gaitan, D. F., Crum, L. A., Church, C. C. and Roy, R. A., 1992. Sonoluminescence and bubble dynamics for a single, stable cavitation bubble. *The Journal of the Acoustical Society of America*, 91(6), pp. 3166-3183.

Geng, H., 2018. *Semiconductor manufacturing handbook*. 2nd ed. New York: McGraw-Hill Education.

Ghauch, A., 2017. Editorial: The importance of advance oxidation processes in degrading persistent pollutants. *Journal of Advance Oxidation Technologies*, 20(1), pp. -.

Goldstein, S., Meyerstein, D. and Czapski, G., 1993. The fenton reagents. *Free Radical Biology & Medicine*, 15(1993), pp. 435-445.

- Gong, L., Zhang, L., Wang, N., Li, J., Ji, S., Guo, H., Zhang, G. and Zhang, Z., 2013. In situ ultraviolet-light-induced TiO₂ nanohybrid superhydrophilic membrane for pervaporation dehydration. *Separation and Purification Technology*, 122(2014), pp. 32-40.
- Gomes, J., Lincho, J., Domingues, E., Quinta-Ferreira, R. M. and Martins, R. C., 2019. N-TiO₂ photocatalysis: a review of their characteristics and capacity for emerging contaminants removal. *Water*, 11(2), pp. 373-408.
- Guo, W., Liu, X., Hua, P., Gao, X., Wu, D., Lu, Z. and Yan, Y., 2012. Hydrothermal synthesis spherical TiO₂ and its photo-degradation property on salicylic acid. *Applied Surface Science*, 258(2012), pp. 6891-6896.
- Gupta, S.M. and Tripathi, M., 2011. A review of TiO₂ nanoparticles. *Chinese Science Bulletin*, 56(2011), pp. 1639-1657.
- Hamad, H., Bailon-Garcia, E., Morales-Torres, S., Carrasco-Marin, F., Perez-Cadenas, A. F. and Maldonado-Hodar, F. J., 2018. Physiochemical properties of new cellulose-TiO₂ composites for the removal of water pollutants: developing specific interactions and performances by cellulose functionalization. *Journal of Environmental Chemical Engineering*, 6(4), pp. 5032-5041.
- Han, X., Kuang, Q., Jin, M., Xie, Z. and Zheng, L., 2009. Synthesis of titania nanosheets with a high percentage of exposed (001) facets and related photocatalytic properties. *Journal of the American Chemical Society*, 131(2019), pp. 3152-3153.
- Hanaor, D. A. H. and Sorrell, C. C., 2011. Review of the anatase to rutile phase transformation. *Journal of Material Science*, 46(2011), pp. 855-874.
- He, L., Liu, Q., Zhang, S., Zhang, X., Gong, C., Shu, H., Wang, G., Liu, H., Wen, S. and Zhang, B., 2018. High sensitivity of TiO₂ nanorod array electrode for photoelectrochemical glucose sensor and its photo fuel cell application. *Electrochemistry Communications*, 94(2018), pp. 18-22.
- Hilal, H. S., Majjad, L. Z., Zaatar, N. and El-Hamouz, A., 2007. Dye-effect in TiO₂ catalyzed contaminant photo-degradation: sensitization vs. charge-transfer formalism. *Solid State Sciences*, 9(2007), pp. 9-15.
- Hu, Y., Liu, H., Rao, Q., Kong, X., Sun, W. and Guo, X., 2011. Effects of N precursor on the agglomeration and visible light photocatalytic activity of N-doped TiO₂ nanocrystalline powder. *Journal of Nanoscience and Nanotechnology*, 11(2011), pp. 3434-3444.
- International Agency for Research on Cancer, 2010. *IARC monographs on the evaluation of carcinogenic risks to humans*. Lyon, France: World Health Organization International Agency for Research on Cancer.

International Water Association, 2018. *Wastewater report 2018*. United Kingdom: International Water Association.

Jia, Y., Zhang, B., Chang, H., Yu, F. and Zhao, Z., 2019. TiO₂/SnO_x-Au nanocomposite catalysed photochromic reaction for colorimetric immunoassay of tumour marker. *Journal of Pharmaceutical and Biomedical Analysis*, 169(2019), pp. 75-81.

Jiang, B., Chen, Z., Dou, H., Sun, Y., Zhang, H., Gong, Z.Q. and Zhang, L., 2018. Superhydrophilic and underwater superoleophobic Ti foam with fluorinated hierarchical flower-like TiO₂ nanostructure for effective oil-in-water emulsion separation. *Applied Surface Science*, 456(2018), pp. 114-123.

Jo, Y., Kim, C., Moon, G., Lee, J., An, T. and Choi, W., 2018. Activation of peroxymonosulfate on visible light irradiated TiO₂ via a charge transfer complex path. *Chemical Engineering Journal*, 346(2018), pp. 249-257.

Jiang, J., Yu, S., Yao, W., Ge, H. and Zhang, G., 2005. Morphogenesis and crystallization of Bi₂S₃ nanostructures by an ionic liquid-assisted templating route: synthesis, formation mechanism, and properties. *Chemistry of Materials*, 17(2005), pp. 6094-6100.

Jiang, X., Tian, X., Huang, D. and Yang, Y., 2011. Cotton fabric coated with nano TiO₂-acrylate copolymer for photocatalytic self-cleaning by in-situ suspension polymerization. *Applied Surface Science*, 257(2011), pp. 8451-8456.

Kakuma, Y., Nosaka, A. Y. and Nosaka, Y., 2015. Difference in TiO₂ photocatalytic mechanism between rutile and anatase studied by detections of active oxygen and surface species in water. *Physical Chemistry Chemical Physics*, 17(2015), pp. 1-8.

Kalaivani, T. and Anilkumar, P., 2017. Role of temperature on the phase modification of TiO₂ nanoparticles synthesized by the precipitation method. *Silicon*, 10(4), pp. 9652-9658.

Kang, S., Zhang, L., Liu, C., Huang, L., Shi, H. and Cui, L., 2017. Hydrogen peroxide activated commercial P25 TiO₂ as efficient visible-light-driven photocatalyst on dye degradation. *International Journal of Electrochemical Science*, 12(2017), pp. 5284-5293.

Kargarzadeh, H., Ahmand, I., Abdullah, I., Dufresne, A., Zainudin, S. Y. and Sheltami, R. M., 2012. Effects of hydrolysis conditions on the morphology, crystallinity, and thermal stability of cellulose nanocrystals extracted from kenaf bast fibers. *Cellulose*, 19(2012), pp. 855-866.

Kavan, L., Gratzel, M., Gilbert, S. E., Klemenz, C. and Scheel, H. J., 1996. Electrochemical and photoelectrochemical investigation of single-crystal anatase. *Journal of the American Chemical Society*, 118(1996), pp. 6716-6723.

Keerthana, B. G. T., Solaiyammal, T., Muniyappan, S. and Murugakoothan, P., 2018. Hydrothermal synthesis and characterization of TiO₂ nanostructures prepared using different solvents. *Materials Letters*, 220(2018), pp. 20-23.

Kim, T. H., Jeong, S., Lim, H., Cho, H., Lee, C. and Choa, Y., 2018. Bulk-direct synthesis of TiO₂ nanoparticles by plasma-assisted electrolysis with enhanced photocatalytic performance. *Journal of the Electrochemical Society*, 165(2), pp. E64-E69.

Kohno, N., Mokudai, T., Ozawa, T. and Niwano, Y., 2010. Free radical formation from sonolysis of water in the presence of different gases. *Journal of Clinical Biochemistry and Nutrition*, 49(2), pp. 96-101.

Kolpak, F. J. and Blackwell, J., 1975. Determination of the structure of cellulose II. *Macromolecules*, 9(2), pp. 273-278.

Konstantinou, I. K. and Albanis, T. A., 2004. TiO₂-assisted photocatalytic degradation of azo dyes in aqueous solution: kinetic and mechanistic investigations: a review. *Applied Catalysis B: Environmental*, 49(2004), pp. 1-14.

Kumar, P. M., Badrinarayanan, S. and Sastry, M., 2000. Nanocrystalline TiO₂ studied by optical, FTIR and X-ray photoelectron spectroscopy: correlation to presence of surface states. *Thin Solid Films*, 358(2000), pp. 123-130.

Kuna, E., Behling, R., Valange, S., Chatel, G. and Colmenares, J.C., 2017. Sonocatalysis: a potential sustainable pathway for the valorization of lignocellulosic biomass and derivatives. *Topics in Current Chemistry*, 375(2), pp. 41-61.

Lai, Z., Peng, F., Wang, H., Yu, H., Zhang, S. and Zhao, H., 2013. A new insight in regulating high energy facets of rutile TiO₂. *Journal of Materials Chemistry A*, 1(2013), pp. 4182-4185.

Leon, A., Reuquen, P., Garin, C., Segura, R., Vargas, P., Zapta, P. and Orihuela, P. A., 2017. FTIR and Raman characterization of TiO₂ nanoparticles coated with polyethylene glycol as carrier for 2-methoxyestradiol. *Applied Sciences*, 7(1), pp. 49-58.

Lin, X., Rong, F., Ji, X. and Fu, D., 2010. Carbon-doped mesoporous TiO₂ film and its photocatalytic activity. *Microporous and Mesoporous Materials*, 142(2011), pp. 276-281.

Ling, A.H., 2019. *Global palm oil trade – prospects and outlook*. Malaysia: Malaysian Palm Oil Board.

Litter, M. I., 2005. Introduction to photochemical advanced oxidation processes for water treatment. *The Handbook of Environmental Chemistry*, 2(2005), pp. 325-366.

Liu, S., Li, X., Zhu, X., Zhao, T., Liu, J. and Zhu, A., 2013. Gliding arc plasma synthesis of crystalline TiO₂ nanopowders with high photocatalytic activity. *Plasma Chemistry and Plasma Processing*, 33(2013), pp. 827-839.

Luttrell, T., Halpegamage, S., Taom J., Kramer, A., Sutter, E. and Batzill, M., 2014. Why is anatase a better photocatalyst than rutile? – Model studies on epitaxial TiO₂ films. *Scientific Reports* 4, 4043(2014), pp. 1-8.

Ma, F. and Hanna, M., 1999. Biodiesel production: a review. *Bioresource Technology*, 70(1999), pp. 1-15.

Mahshid, S., Askari, M. and Ghamsari, M. S., 2007. Synthesis of TiO₂ nanoparticles by hydrolysis and peptization of titanium isopropoxide solution. *Journal of Materials Processing Technology*, 189(2007), pp. 269-300.

Malaysian Palm Oil Board, 2019. *Production of crude palm oil for the month of June 2019*. Retrieved from <http://bepi.mpob.gov.my/index.php/en/statistics/production/368-production-2019/906-production-of-crude-oil-palm-2019.html>

Mateo-Sagasta, J., Raschid-Sally, L. and Thebo, A., 2015. *Global wastewater and sludge production, treatment and use*. Dordrecht: Springer.

Miao, J., Zhang, R. and Zhang, L., 2018. Photocatalytic degradations of three dyes with different chemical structures using ball-milled TiO₂. *Materials Research Bulletin*, 97(2018), pp. 100-114.

Mikkonen, K. S., Kirjoranta, S., Xu, C., Hemming, J., Pranovich, A., Bhattarai, M., Peltonen, L., Kilpelainen, P., Maina, N., Tenkanen, M., Lehtonen, M. and Willfor, S., 2019. Environmentally-compatible alkyd paints stabilized by wood hemicelluloses. *Industrial Crops & Products*, 133(2019), pp. 212-220.

Mittal, A., Mittal, J., Malviya, A. and Gupta, V. K., 2009. Adsorptive removal of hazardous anionic dye “Congo Red” from wastewater using waste materials and recovery by desorption. *Journal of Colloid and Interface Science*, 340(2009), pp. 16-26.

Mohamed, M. A., Salleh, W. N. W., Jaafar, J., Ismail, A. F., Mutalid, M. A., Sani, N. A. A., Asri, S. E. A. M. and Ong, C. S., 2015. Physiochemical characteristic of regenerated cellulose/M-doped TiO₂ nanocomposite membrane fabricated from recycled newspaper with photocatalytic activity under UV and visible light irradiation. *Chemical Engineering Journal*, 284(2016), pp. 202-215.

Mohamed, M. A., Mutalib, M. A., Hir, Z. A., Zain, M. F. M., Mohamad, A. B., Minggu, L. J., Awang, N. A. and Salleh, W. N. W., 2017. An overview on cellulose-based material in tailoring bio-hybrid nanostructured photocatalysts for water treatment and renewable energy applications. *International Journal of Biological Macromolecules*, 103(2017), pp. 1232-1256.

Mohamed, R. M., Mkhaliid, I. A., Baeissa, E. S. and Al-Rayyani, M. A., 2012. Photocatalytic degradation of methylene blue by Fe/ZnO/SiO₂ nanoparticles under visible light. *Journal of Nanotechnology*, 2012(-), pp. 1-5.

Mostafa, M., 2015. Waste water treatment in textile Industries – the concept and current removal technologies. *Journal of Biodiversity and Environmental Sciences*, 7(1), pp. 2222-3045.

Nag, A., 2008. *Biofuels refining and performance*. New York: McGraw-Hill Education.

Najafi-Ashtiani, H., 2018. Performance evaluation of free-silicon organic-inorganic hybrid (SiO₂-TiO₂-PVP) thin films as a gate dielectric. *Applied Surface Science*, 455(2018), pp. 373-378.

Nakata, K. and Fujishima, A., 2012. TiO₂ photocatalysis: design and applications. *Journal of Photochemistry and Photobiology C: Photochemistry Reviews*, 13(2012), pp. 169-189.

Nambiappan, B., Ismail, A., Hashim, N., Ismail, I., Shahari, D. N., Idris, N. A. N., Omar, N., Salleh, K. M., Hassan, N. A. M. and Kushairi, A., 2018. Malaysia: 100 years of resilient palm oil economic performance. *Journal of Oil Palm Research*, 30(1), pp. 13-25.

Nambiappan, B., Ismail, A., Hashim, N., Ismail, I., Shahari, D.N., Idris, N. A. N., Omar, N., Salleh, K. M., Hassan, N. A. M. and Kushairi, A., 2018. Malaysia: 100 Years of Resilient Palm Oil Economic Performance. *Journal of Oil Palm Research*, 30(1), pp. 13-25.

Nandiyanto, A. B. D., Zaen, R. and Oktiani, R., 2020. Correlation between crystallite size and photocatalytic performance of micrometer-sized monoclinic WO₃ particles. *Arabian Journal of Chemistry*, 13(2020), pp. 1283-1296.

Nazir, M. S., Wahjoedi, B. A., Yussof, A. W. and Abdullah, M. A., 2013. Eco-friendly extraction and characterization of cellulose from oil palm empty fruit bunches. *BioResources*, 8(2), 2161-2172.

Nolan, N. T., Synnott, D. W., Seery, M. K., Hinder, S. J., Wassenhoven, A. V. and Pillai, S. C., 2012. Effect of N-doping on the photocatalytic activity of sol-gel TiO₂. *Journal of Hazardous Materials*, 211-212(2012), pp. 88-94.

Nunez, J. A. P., Salapare III, H. S., Villamayor, M. M. S., Siringan, M. A. T. and Ramos, H. J., 2017. Antibacterial efficiency of magnetron sputtered TiO₂ on poly(methylmethacrylate). *Surfaces and Interfaces*, 8(2017), pp. 28-35.

O'Hare, D., 2001. Hydrothermal synthesis. In: K. H. J. Buschow, R. W. Cahn, M. C. Flemings, B. Ilshner, E. J. Kramer, S. Mahajan and P. Veyssiere, eds. *Encyclopaedia of materials: science and technology*. Oxford, United Kingdom: Elsevier. pp. 3989-3992.

O'Sullivan A., 1996. Cellulose: the structure slowly unravels. *Cellulose*, 4(1997), 173-207.

Odlare, M., 2014. Introductory chapter for water resources. In: Elias, S. A., ed. *Reference module in earth systems and environmental sciences*. Oxford, United Kingdom: Elsevier. pp. 1-2.

Ogi, H., Hirao, M. and Shimoyama, M., 2002. Activation of TiO₂ photocatalyst by single-bubble sonoluminescence for water treatment. *Ultrasonics*, 40(2002), pp. 649-650.

Okitsu, K., Iwasaki, K., Yobiko, Y., Bandow, H., Nishimura, R. and Maeda, Y., 2005. Sonochemical degradation of azo dyes in aqueous solution: a new heterogeneous kinetics model taking into account the local concentration of OH radicals and azo dyes. *Ultrasonics Sonochemistry*, 12(2005), pp. 255-262.

Okiyama, A., Motoki, M. and Yamanaka, S. 1993. Bacterial cellulose IV. Application to processed foods. *Food Hydrocolloids*, 6(6), pp. 503-511.

Oliveira, A. C. D. M., Santos, M. S. D., Brandao, L. M. S., Resende, I. T. D., Leo, I. M., Morillo, E. S., Yerga, R. M. N., Fierro, J. L. G., Egues, S. M. D. S. and Figueiredo, R. T., 2017. The effect of cellulose loading on the photoactivity of cellulose-TiO₂ hybrids for hydrogen production under simulated sunlight. *International Journal of Hydrogen Energy*, -(2017), pp. 1-8.

Paola, A. D., Bellardita, M. and Palmisano, L., 2013. Brookite, the least known TiO₂ photocatalyst. *Catalyst*, 3(2013), pp. 36-73.

Paraschiv, D., Tudor, C. and Petrariu, R., 2015. The textile industry and sustainable development: a holt-winters forecasting investigation for the eastern European area. *Sustainability*, 7(2), pp. 1280-1291.

Park, S., Baek, S., Kim, D. and Lee, S., 2018. Oxygen-vacancy-modified brookite TiO₂ nanorods as visible-light-responsive photocatalyst. *Materials Letters*, 232(2018), pp. 146-149.

Peng, Q., Dong, Y. and Li, Y., 2003. ZnSe semiconductor hollow microspheres. *Angewandte Chemie International Edition*, 42(2003), pp. 3027-3030.

Perera, S. D., Marianom R. G., Vu, K., Nour, N., Sietz, O., Chabal, Y. and Balkus, K. J. J., 2012. Hydrothermal synthesis of graphene-TiO₂ nanotube composites with enhanced photocatalytic activity. *ACS Catalysis*, 2(2012), pp. 949-956.

Poletto, M., Junior, H. L. O. and Zattera, A. J., 2014. Native cellulose: structure, characterization and thermal properties. *Materials*, 7(2014), pp. 6105-6119.

Ponomarev, A. V., 2017. Radiolysis of lignin prospective mechanism of high-temperature decomposition. *Radiation Physics and Chemistry*, 141(2017), pp. 160-167.

Pookmanee, P., Promwanna, K., Narong, K., Ananpattarachai, J., Junin, C., Ananpattarachai, J. and Phanichphant, S., 2018. Titanium dioxide doped with nitrogen nanopowder prepared by hydrothermal method. *Solid State Phenomena*, 283(-), pp. 167-172.

Prakash, J., Sun, S., Swart, H. C. and Gupta, R. K., 2018. Noble metals-TiO₂ nanocomposites: from fundamental mechanisms to photocatalysis, surface enhanced Raman Scattering and antibacterial applications. *Applied Materials Today*, 11(2018), pp. 82-135.

Qiu, P., Park, B., Choi, J., Thokchom, B., Pandit, A. B. and Khim, J., 2018. A review on heterogeneous sonocatalyst for treatment of organic pollutants in aqueous phase based on catalytic mechanism. *Ultrasonics Sonochemistry*, 45(2018), pp. 29-49.

Ram, M. K., Andresscue, S. and Ding, H., 2011. *Nanotechnology for environmental decontamination*. New York: McGraw-Hill Education.

Rantuch, P. and Chrebet, T., 2013. Thermal decomposition of cellulose insulation. *Cellulose Chemistry and Technology*, 48(5-6), pp. 461-467.

Rijsberman, F. R. and Cosgrove, W. J., 2000. *World water vision: making water everybody's business*. United Kingdom: Earthscan Publications Ltd.

Robinson, T., McMullan, G., Marchant, R. and Nigam, P., 2004. Remediation of dyes in textile effluent: a critical review on current treatment technologies with a proposed alternative. *Bioresource Technology*, 77(2001), pp. 247-255.

Rodriguez, M. M., Peng, X., Liu, L., Li, Y. and Andino, J. M., 2012. A density functional theory and experimental study of CO₂ interaction with brookite TiO₂. *The Journal of Physical Chemistry C*, 116(2012), pp. 19755-19764.

Rosa, J. M., Tombourgi, E. B., Santana, J. C. C., Araujo, M. D. C., Ming, W.C. and Trindade, N., 2014. Development of colours with sustainability: a comparative study between dyeing of cotton with reactive and vat dyestuffs. *Textile Research Journal*, 84(10), pp. 1009-1017.

Ryu, H. W., Lee, H. W., Jae, J. and Park, Y. K., 2019. Catalytic pyrolysis of lignin for the production of aromatic hydrocarbons: effect of magnesium oxide catalyst. *Energy*, 179(2019), pp. 669-675.

Scheller, H. V. and Ulvskov, P., 2010. Hemicelluloses. *Annual Review of Plant Biology*, 61(2010), pp. 263-289.

Shahzad, M. W., Ng, K. C., Thu, K., Saha, B. B. and Chun, W. G., 2014. Multi effect desalination and adsorption desalination (MEDAD): a hybrid desalination method. *Applied Thermal Engineering*, 72(2014), pp. 289-297.

Sharfudeen, B. F. J. M., Latheef, A. F. A. and Ambrose, R. V., 2017. Synthesis and characterization of TiO₂ nanoparticles and investigation of antimicrobial

activities against human pathogens. *Journal of Pharmaceutical Sciences and Research*, 9(9), pp. 1604-1608.

Sharma, K. R., 2010. *Nanostructuring operations in nanoscale science and engineering*. New York: McGraw-Hill Companies, Inc.

Shi, G., 2015. *Oxidation of 2,4-D using iron activated persulfate and peroxymonosulfate*. Bachelor. Iowa State University.

Shi, W., Song, S. and Zhang, H., 2013. Hydrothermal synthetic strategies of inorganic semiconducting nanostructures. *Chemical Society Reviews*, 42(2013), pp. 5714-5743.

Shriram, B. and Kanmanim, S., 2014. *Ozonation of textile dyeing wastewater – a review*. Chennai: Anna University.

Shrotri, A., Kobayashi, H. and Fukuoka, A. 2017. Catalytic conversion of structural carbohydrates and lignin to chemicals. *Advances in Catalysis*, 60(2017), pp. 59-123.

Si, Y., Zhang, A., Liu, C., Pei, N. and Yu, H., 2019. Photo-assisted electrochemical detection of bisphenol A in water samples by renewable {001}-exposed TiO₂ single crystals. *Water Research*, 157(2019), pp. 30-39.

Silva, C. G. D. and Faria, J. L., 2003. Photochemical and photocatalytic degradation of an azo dye in aqueous solution by UV irradiation. *Journal of Photochemistry and Photobiology A: Chemistry*, 155(2003), pp. 133-143.

Singh, J., Khan, S. A., Kotnala, R. K. and Mohapatra, S., 2017. Nanostructured TiO₂ thin films prepared by RF magnetron sputtering for photocatalytic applications. *Applied Surface Science*, 422(2017), pp. 953-961.

Singh, J., Sahu, K., Satpati, B. and Mohapatra, S., 2018. Facile synthesis, structural, optical and photocatalytic properties of anatase/ rutile mixed phase TiO₂ ball-like sub-micron structure. *Optik – International Journal for Light and Electron Optics*, 188(2019), pp. 270-276.

Smugat-Kogut, M., Piskier, T., Walendzik, B. and Szymanowska-Powalowska, D., 2019. Assessment of wasteland derived biomass for bioethanol production. *Electronic Journal of Biotechnology*, 41(2019), pp. 1-8.

Sotomayor, F. J., Cychosz, K. A. and Thommes, M., 2018. Characterization of micro/mesoporous materials by physisorption: concepts and case studies. *Accounts of Materials & Surface Research*, 3(2), pp. 34-50.

Speight, J. G., 2008. *Synthetic fuels handbook: properties, process, and performance*. New York: The McGraw-Hill Companies, Inc.

- Sui, Y., Wu, L., Zhong, S. and Liu, Q., 2019. Carbon quantum dots/TiO₂ nanosheets with dominant (001) facets for enhanced photocatalytic hydrogen evolution. *Applied Surface Science*, 480(2019), pp. 810-816.
- Suwannaruang, T., Rivera, K. K. P., Neramittagapong, A. and Wantala, K., 2015. Effects of hydrothermal temperature and time on uncalcined TiO₂ synthesis for reactive red 120 photocatalytic degradation. *Surface & Coatings Technology*, 271(2015), pp. 192-200.
- Titirici, M., Antonietti, M. and Thomas, A., 2006. A generalized synthesis of metal oxide hollow spheres using a hydrothermal approach. *Chemistry of Materials*, 18(2006), pp. 3808-3812.
- Torres-Palma R. A. and Serna-Galvis, E. A., 2018. Sonolysis. In: S. C. Ameta and R. Ameta, eds. *Advance oxidation processes for waste water treatment*. Massachusetts, United States: Academic Press. pp. 177-213.
- Trop, P., Anicic, B. and Goricanec, D., 2014. Production of methanol from a mixture of terrified biomass and coal. *Energy*, 77(2014), pp. 125-132.
- Tuckute, S., Varnagiris, S., Urbonavicius, M., Lelis, M. and Sakalauskaite, S., 2019. Tailoring of TiO₂ film crystal texture for higher photocatalysis efficiency. *Applied Surface Science*, 489(2019), pp. 576-583.
- Uddin, M. J., Cesano, F., Bonino, F., Bordiga, S., Spoto, G., Scarano, D. and Zecchina, A., 2007. Photoactive TiO₂ films on cellulose fibres: synthesis and characterization. *Journal of Photochemistry and Photobiology A: Chemistry*, 189(2007), pp. 286-294.
- Vaiano, F., Mari, F. and Busardo, F. P., 2014. Enhancing the sensitivity of the LC-MS/MS detection of propofol in urine and blood by azo-coupling derivatization. *Analytical and Bioanalytical Chemistry*, 406(15), pp. 3579-3587.
- Vanek, F. M., Albright, L. D and Angenent, L. T., 2012. *Energy systems engineering: evaluation and implementation*. 2nd ed. New York: McGraw-Hill.
- Viana, M. M., Soares, V. F. and Mohallem, N. D. S., 2010. Synthesis and characterization of TiO₂ nanoparticles. *Ceramics International*, 36(2010), pp. 2047-2053.
- Vinu, R. and Madras, G., 2008. Kinetics of sonophotocatalytic degradation of anionic dyes with nano-TiO₂. *Environmental Science & Technology*, 43(2009), pp. 473-479.
- Wang, F., Ge, W., Shen, T., Ye, B., Fu, Z. and Lu, Y., 2017. The effect of bulk/surface defects ratio change on the photocatalysis of TiO₂ nanosheet film. *Applied Surface Science*, 410(2017), pp. 513-518.

Wang, W., Chen, J., Gao, M., Huang, Y., Zhang, X. and Yu, H., 2016. Photocatalytic degradation of atrazine by boron-doped TiO₂ with a tunable rutile/anatase Ratio. *Applied Catalysis B: Environmental*, 195(2016), pp. 69-76.

Waring, D. R., 1984. Heterocyclic dyes and pigments. *Comprehensive Heterocyclic Chemistry*, 1(1984), pp. 317-346.

Xu, X., Li, H., Wang, W. and Gu, J., 2004. Degradation of dyes in aqueous solutions by the fenton process. *Chemosphere*, 57(2004), pp. 595-600.

Yang, H. G. and Zeng, H. C., 2004. Preparation of hollow anatase TiO₂ nanospheres via Ostwald ripening. *The Journal of Physical Chemistry B*, 108(2004), pp. 3492-3495.

Yang, H. G., Sun, C. H., Qiao, S. Z., Zou, J., Liu, G., Smith, S. C., Cheng, H. M. and Lu, G. Q., 2008. Anatase TiO₂ single crystals with a large percentage of reactive facets. *Nature*, 453(2008), pp. 638-641.

Yaseen, D. A. and Schulz, M., 2019. Textile dye wastewater characteristics and constituents of synthetic effluents: a critical review. *International Journal of Environmental Science and Technology*, 16(2019), pp. 1193-1226.

Yasui, K., Tuziuti, T., Sivakumar, M. and Iida, Y., 2004. Sonoluminescence. *Applied Spectroscopy Reviews*, 39(3), pp. 399-436.

Yousefi, A. R., Savadkoohi, B., Zahedi, Y., Hatami, M. and Ako, K., 2019. Fabrication and characterization of hybrid sodium montmorillonite/TiO₂ reinforced cross-linked wheat starch-based nanocomposites. *International Journal on Biological Macromolecules*, 131(2019), pp. 253-263.

Yu, J., Wang, G., Cheng, B. and Zhou, M., 2007. Effects of hydrothermal temperature and time on the photocatalytic activity and microstructures of bimodal mesoporous TiO₂ powders. *Applied Catalysis B: Environmental*, 69(2007), pp. 171-180.

Yue, Y. 2011. *A comparative study of cellulose I and II and fibres and nanocrystals*. Master. Louisiana State University.

Yunus, N. N., Hamzah, F., So'aib, M. S. and Krishnan, J., 2016. Effect of catalyst loading on photocatalytic degradation of phenol using N, S co-doped TiO₂. *Materials Science and Engineering*, 206(2017), pp. 1-6.

Zaleska, A., 2008. Doped-TiO₂: a review. *Recent Patents on Engineering*, 2(2008), pp. 157-164.

Zhang, W., Gu, J., Zhao, J., Ma, H., Wu, C., Zhang, C., Xie, Y., Yang, F. and Zheng, X., 2019. A hydrogenated black TiO₂ coating with excellent effects for photothermal therapy of bone tumour and bone regeneration. *Materials Science & Engineering C*, 102(2019), pp. 458-470.

Zhou, X., Yu, S., Zhang, J., Lv, Z., Liu, E. and Zhao, Y., 2019. Colourful nanostructured TiO₂ film with superhydrophobic-superhydrophilic switchable wettability and anti-fouling property. *Journal of Alloys and Compounds*, 798(2019), pp. 257-266.

Zhou, X., Zhang, D., Zhu, Y., Shen, Y., Guo, X., Ding, W. and Chen, Y., 2006. Mechanistic Investigations of PEG-directed assembly of one-dimensional ZnO nanostructures. *Journal of Physical Chemistry B*, 110(2006), pp. 25734-25739.

Ziarani, G. M., Moradi, R. and Lashgari, N., 2018. *Metal-free Synthetic organic dyes*. Oxford, United Kingdom: Elsevier.

Zoccal, J. V. M., Arouca, F. D. O. and Goncalves, J. A. S., 2010. Synthesis and characterization of TiO₂ nanoparticles by the method Pechini. *Materials Science Forum*, 660(2010), pp. 385-390.